

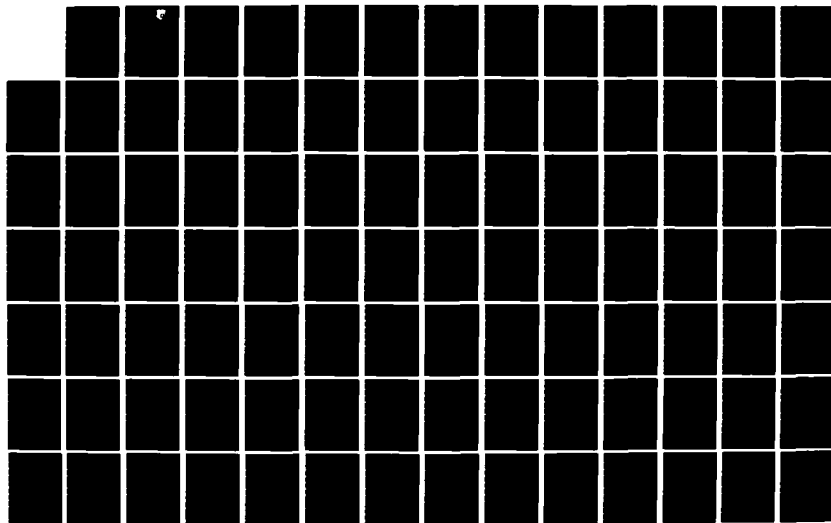
AD-A133 587

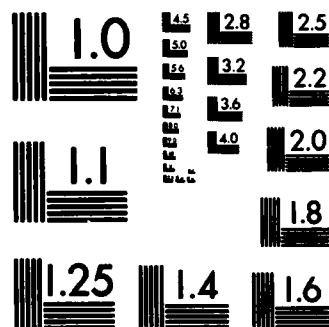
THE CALCULATED PERFORMANCE OF SOME RADAR AND  
TRANSMISSOMETER SYSTEMS IN R. (U) OHIO STATE UNIV  
COLUMBUS ELECTROSCIENCE LAB E L UTT ET AL. DEC 82  
ESL-713671-2-VOL-1 AFWAL-TR-82-1147-VOL-1 F/G 17/9

1/2

UNCLASSIFIED

NL



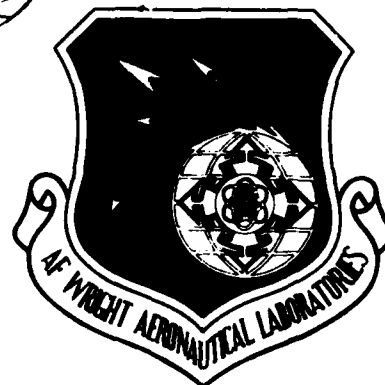


MICROCOPY RESOLUTION TEST CHART  
NATIONAL BUREAU OF STANDARDS-1963-A

AD 133587 AD - A133587

12

AFWAL-TR-82-1147  
Volume I



THE CALCULATED PERFORMANCE OF SOME RADAR AND  
TRANSMISSOMETER SYSTEMS IN RAIN AND FOG AT  
35, 94, 140, AND 240 GHz

E.L. Utt  
C.A. Levis

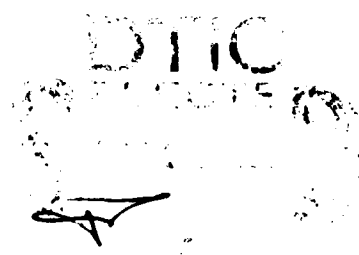
The Ohio State University ElectroScience Laboratory  
Department of Electrical Engineering  
Columbus, Ohio 43212

December 1982

Final Report for Period 1 April 1981 to 31 July 1982

Approved for public release; distribution unlimited.

Avionics Laboratory  
AF Wright Aeronautical Laboratories  
Air Force Systems Command  
Wright-Patterson Air Force Base, Ohio 45433

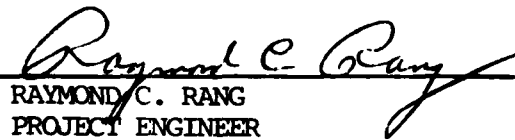


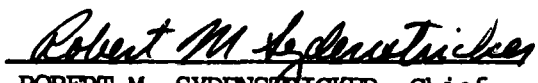
83 10 20 045

## NOTICE

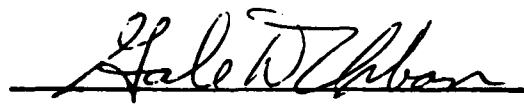
When Government drawings, specifications, or other data are used for any purpose other than in connection with a definitely related Government procurement operation, the United States Government thereby incurs no responsibility nor any obligation whatsoever; and the fact that the government may have formulated, furnished, or in any way supplied the said drawings, specifications, or other data, is not to be regarded by implication or otherwise as in any manner licensing the holder or any other person or corporation, or conveying any rights or permission to manufacture, use, or sell any patented invention that may in any way be related thereto.

This technical report has been reviewed and is approved for publication.

  
RAYMOND C. RANG  
PROJECT ENGINEER  
Mission Avionics Division

  
ROBERT M. SYDENSTRICKER, Chief  
Automatic Target Classification Group  
Mission Avionics Division  
Avionics Laboratory

FOR THE COMMANDER:

  
GALE D. URBAN, Chief  
Electro-Optics Branch  
Mission Avionics Division  
Avionics Laboratory

"If your address has changed, if you wish to be removed from our mailing list, or if the addressee is no longer employed by your organization please notify AFWAL/AARI, W-P AFB, OH 45433 to help maintain a current mailing list".

Copies of this report should not be returned unless return is required by security considerations, contractual obligations, or notice on a specific document.

REPORT DOCUMENTATION PAGE		READ INSTRUCTIONS BEFORE COMPLETING FORM
1. REPORT NUMBER AFWAL-TR-82-1147 Volume I	2. GOVT ACCESSION NO. AD-A133587	3. RECIPIENT'S CATALOG NUMBER
4. TITLE (and Subtitle) THE CALCULATED PERFORMANCE OF SOME RADAR AND TRANSMISSOMETER SYSTEMS IN RAIN AND FOG AT 35, 94, 140, AND 240 GHz		5. TYPE OF REPORT & PERIOD COVERED Final Report 1 April 1981 - 31 July 1982
7. AUTHOR(s) E.L. Utt and C.A. Levis		6. PERFORMING ORG. REPORT NUMBER ✓ ESL 713671-2-Volume I
9. PERFORMING ORGANIZATION NAME AND ADDRESS The Ohio State University ElectroScience Lab. The Department of Electrical Engineering Columbus, Ohio 43212		8. CONTRACT OR GRANT NUMBER(s) F33615-81-C-1437
11. CONTROLLING OFFICE NAME AND ADDRESS Avionics Laboratory (AFWAL/AARI) AF Wright Aeronautical Laboratories, AFSC Wright-Patterson Air Force Base, Ohio 45433		10. PROGRAM ELEMENT, PROJECT, TASK AREA & WORK UNIT NUMBERS
14. MONITORING AGENCY NAME & ADDRESS (if different from Controlling Office)		12. REPORT DATE December 1982
		13. NUMBER OF PAGES 129
		15. SECURITY CLASS. (of this report) Unclassified
		15a. DECLASSIFICATION/DOWNGRADING SCHEDULE
16. DISTRIBUTION STATEMENT (of this Report) Approved for public release; distribution unlimited.		
17. DISTRIBUTION STATEMENT (of the abstract entered in Block 20, if different from Report)		
18. SUPPLEMENTARY NOTES AFWAL-TR-82-1147, Volume II contains computer software; therefore distribution is limited in accordance with AFR 300-6 (DoD Dir. 4160.19 dtd 5 Apr 73). Non-DoD requests for Volume II must include the statement of terms and conditions contained in Atch. 21 to AFR 300-6. See Foreword.		
19. KEY WORDS (Continue on reverse side if necessary and identify by block number)		
millimeter wave	rain	transmission
near millimeter	fog	radar
attenuation	precipitation	extinction
propagation	transmissometer	
20. ABSTRACT (Continue on reverse side if necessary and identify by block number) → The effects of rain and fog are examined for three transmissometer and threeradar systems: double-ended (direct path) with square-wave modulation and square-law detector, single-ended (folded path) with square-wave modulation and square-law detection, single-ended CW with quadrature receiver, single-ended pulsed with post-detection pulse integration, single-ended pulsed with quadrature receiver, and single-ended with linear FM pulse compression. Computer algorithms were developed to find the probability of detection as a function of range for the radar systems, and the signal-to-noise ratio as a		

function of range for the transmissometer systems. These algorithms are used recursively to determine the range at which specified performance is attained as a function of rain rate or fog liquid water content. Calculated results are presented for exponential drop-size distributions; provision has been made for the extension to other distributions.

Volume I contains the theory and results; computer code listings and directions for use of the codes are given in Volume II.

## FOREWORD

This study constitutes a thesis submitted by Mr. Utt in partial fulfillment of the requirements for the degree Master of Science in Electrical Engineering under the guidance of Professor Levis.

The helpful criticism of graduate student colleagues at the ElectroScience Laboratory is gratefully acknowledged, as is the thesis of O.M. Buyukdura, which laid the foundation for this study.

This work was sponsored under Contract F33615-81-C-1437 by the Avionics Laboratory, Air Force Wright Aeronautical Laboratory, Air Force Systems Command, United States Air Force, Wright-Patterson Air Force Base, Ohio 45433.

Authorized non-DoD DTIC users may order Volume II by sending a DTIC Form 55, "Request for Limited Document," directly to DTIC. Also send a signed copy of Atch. 21 (contained in AFR 300-6) to AFWAL/AARI concurrently.



Accession For

NTIS GRA&I ☒

DTIC TAB ☐

Unannounced ☐

Justification

By

DTIC TAB ☐

Unannounced ☐

Justification

By

A

# TABLE OF CONTENTS

## Volume I

	Page
FOREWORD . . . . .	iii
LIST OF FIGURES. . . . .	vii
LIST OF TABLES . . . . .	xii
I INTRODUCTION . . . . .	1
II DERIVATION OF SIGNAL-TO-NOISE EXPRESSIONS . . . . .	5
A. Derivation of Pre-detection Signal-to-Noise Ratio Expressions	5
B. Derivation of Processed Signal-to-Noise Ratio Expressions	8
1. One-way Transmission and Square-Law Detection	8
2. Two-way Transmission and Square-Law Detection	11
3. CW Signal Transmission and Quadrature Receiver	11
4. Pulsed Source with Incoherent Pulse Integration	18
5. Pulsed Source with a Quadrature Receiver	20
6. Pulsed Source with Pulse Compression	23
C. Summary	28
III DERIVATION OF PROBABILITY OF DETECTION . . . . .	29
A. Description of Noise in the Radar System	29
B. Derivation of the Probability of Detection	31
C. Derivation of the Probability of False Alarm	38
IV ATTENUATION DUE TO RAIN AND FOG. . . . .	44
A. Dropsizes Distribution for Rain	45
B. Dropsizes Distribution for Fog	45
V RESULTS AND DISCUSSION . . . . .	49
A. Graphical Results and Discussion	54
1. One-way Transmission and Square-Law Detection	54
2. Two-way Transmission and Square-Law Detection	61
3. CW Signal Transmission and Quadrature Receiver	70
4. Pulsed Source with Incoherent Pulse Integration	78
5. Pulsed Source with a Quadrature Receiver	86
6. Pulsed Source with Pulse Compression	94
B. Effects of Rain Attenuation	103



	Page
C. Effects of Fog Attenuation	111
D. Conclusions	113
REFERENCES . . . . .	115
APPENDIX A - MODEL FOR COMPLEX INDEX OF REFRACTION. . . . .	117
APPENDIX B - PULSE COMPRESSION RADAR. . . . .	124

## Volume II

	Page
APPENDIX C - COMPUTER PROGRAM LISTING . . . . .	130
LINKING PROCEDURE FOR COMPUTER PROGRAMS . . . . .	220

# LIST OF FIGURES

Figure		Page
1	Specific attenuation in clear air versus frequency.	2
2	Receiver system with square-law detector.	9
3	Quadrature Receiver.	12
4	(a.) Correlation detector and (b.) Matched filter.	13
5	(a.) Integration improvement factor, (b.) Integration loss versus number of pulses integrated.	21
6	Typical Intrapulse Linear Frequency Pulse Compression Radar.	25
7	Idealized Pulse Compression Characteristics.	26
8	Wide-pulse and Compressed Pulse Waveforms.	27
9	Probability of Detection and Probability of False Alarm in terms of density function plot $p(r)$ .	34
10	Typical plot of Probability of Detection versus Signal-to-noise Ratio for a specified Probability of False Alarm.	40
11	Typical plot of Probability of Detection versus Range for a specified Probability of False Alarm.	41
12	Signal-to-noise ratio versus Range for the double-ended system with square-law detection. $\alpha = 0$ dB/km.	56
13	Signal-to-noise ratio versus Range for the double-ended system with square-law detection. $\alpha = 5$ dB/km.	57
14	Signal-to-noise ratio versus Range for the double-ended system with square-law detection. $\alpha = 10$ dB/km.	58
15	Signal-to-noise ratio versus Range for the double-ended system with square-law detection. $\alpha = 20$ dB/km.	59
16	Range versus Specific Attenuation for the double-ended system with square-law detection. $E/N = 10$ dB.	60
17	Signal-to-noise ratio versus Range for the single-ended system with square-wave modulation and square-law detection. $\alpha = 0$ dB/km, $\sigma = 125$ m <sup>2</sup> .	63

Figure		Page
18	Signal-to-noise ratio versus Range for the single-ended system with square-wave modulation and square-law detection. $\alpha = 5$ dB/km, $\sigma = 125$ m <sup>2</sup> .	64
19	Signal-to-noise ratio versus Range for the single-ended system with square-wave modulation and square-law detection. $\alpha = 10$ dB/km, $\sigma = 125$ m <sup>2</sup> .	65
20	Signal-to-noise ratio versus Range for the single-ended system with square-wave modulation and square-law detection. $\alpha = 20$ dB/km, $\sigma = 125$ m <sup>2</sup> .	66
21	Probability of Detection versus Post-detection Signal-to-noise ratio for single-ended system with square-wave modulation and square-law detection.	67
22	Probability of Detection versus Range for single-ended system with square-wave modulation and square-law detection. $f = 94$ GHz, $\alpha = 20$ dB/km, $\sigma = 125$ m <sup>2</sup> .	68
23	Range versus Specific Attenuation for the single-ended system with square-wave modulation and square-law detection. $P_d = 0.995$ , $P_{fa} = 10^{-6}$ (Computed processed E/N = 15.83 dB.)	69
24	Signal-to-noise ratio versus Range for the single-ended CW system with quadrature receiver. $\alpha = 0$ dB/km, $\sigma = 125$ m <sup>2</sup> .	71
25	Signal-to-noise ratio versus Range for the single-ended CW system with quadrature receiver. $\alpha = 5$ dB/km, $\sigma = 125$ m <sup>2</sup> .	72
26	Signal-to-noise ratio versus Range for the single-ended CW system with quadrature receiver. $\alpha = 10$ dB/km, $\sigma = 125$ m <sup>2</sup> .	73
27	Signal-to-noise ratio versus Range for the single-ended CW system with quadrature receiver. $\alpha = 20$ dB/km, $\sigma = 125$ m <sup>2</sup> .	74
28	Probability of Detection versus Post-detection Signal-to-noise ratio for a single-ended CW system with quadrature receiver.	75
29	Probability of Detection versus Range for the single-ended CW system with quadrature receiver. $f = 94$ GHz, $\alpha = 20$ dB/km, $\sigma = 125$ m <sup>2</sup> .	76

Figure		Page
30	Range versus Specific Attenuation for the single-ended CW system with quadrature receiver. $P_d = 0.995$ , $P_{fa} = 10^{-6}$ , (Computed processed $E/N = 17.79$ dB.)	77
31	Signal-to-noise ratio versus Range for the single-ended pulsed source range gated radar employing post-detection integration, $n=10000$ , $\alpha = 0$ dB/km, and $\sigma = 125$ m <sup>2</sup> .	79
32	Signal-to-noise ratio versus Range for the single-ended pulsed source range gated radar employing post-detection integration. $n=10000$ , $\alpha = 5$ dB/km, and $\sigma = 125$ m <sup>2</sup> .	80
33	Signal-to-noise ratio versus Range for the single-ended pulsed source range gated radar employing post-detection integration. $n=10000$ , $\alpha = 10$ dB/km, and $\sigma = 125$ m <sup>2</sup> .	81
34	Signal-to-noise ratio versus Range for the single-ended pulsed source range gated radar employing post-detection integration. $n=10000$ , $\alpha = 20$ dB/km, and $\sigma = 125$ m <sup>2</sup> .	82
35	Probability of Detection versus Post-detection Signal-to-noise ratio for the single-ended pulsed range gated radar.	83
36	Probability of Detection versus Range for the single-ended pulsed source range gated radar. $f = 94$ GHz, $\alpha = 20$ dB/km, and $\sigma = 125$ m <sup>2</sup> .	84
37	Range versus Specific Attenuation for the single-ended pulsed source range gated radar employing post-detection integration. $P_d = 0.995$ , $P_{fa} = 10^{-6}$ , (Computed processed $E/N = 17.79$ dB.)	85
38	Signal-to-noise ratio versus Range for the single-ended pulsed radar system with quadrature receiver. $\alpha = 0$ dB/km, $\sigma = 10$ m <sup>2</sup> .	87
39	Signal-to-noise ratio versus Range for the single-ended pulsed radar system with quadrature receiver. $\alpha = 5$ dB/km, $\sigma = 10$ m <sup>2</sup> .	88
40	Signal-to-noise ratio versus Range for the single-ended pulsed radar system with quadrature receiver. $\alpha = 10$ dB/km, $\sigma = 10$ m <sup>2</sup> .	89

Figure		Page
41	Signal-to-noise ratio versus Range for the single-ended pulsed radar system with quadrature receiver. $\alpha = 20$ dB/km, and $\sigma = 10$ m <sup>2</sup> .	90
42	Probability of Detection versus Post-detection Signal-to-noise ratio for a single-ended radar system with quadrature receiver.	91
43	Probability of Detection versus Range for a single-ended pulsed radar system with quadrature receiver. $f = 94$ GHz, $\alpha = 20$ dB/km, and $\sigma = 10$ m <sup>2</sup> .	92
44	Range versus Specific Attenuation for the single-ended pulsed radar system with quadrature receiver. $P_d = 0.995$ , $P_{fa} = 10^{-6}$ (Computed processed E/N = 17.79 dB.)	93
45	Signal-to-noise ratio versus Range for the single-ended pulsed radar system with pulse compression. $\alpha = 0$ dB/km, $\sigma = 10$ m <sup>2</sup> .	95
46	Signal-to-noise ratio versus Range for the single-ended pulsed radar system with pulse compression. $\alpha = 5$ dB/km, $\sigma = 10$ m <sup>2</sup> .	96
47	Signal-to-noise ratio versus Range for the single-ended pulsed radar system with pulse compression. $\alpha = 10$ dB/km, $\sigma = 10$ m <sup>2</sup> .	97
48	Signal-to-noise ratio versus Range for the single-ended pulsed radar system with pulse compression. $\alpha = 20$ dB/km, $\sigma = 10$ m <sup>2</sup> .	98
49	Probability of Detection versus Post-detection Signal-to-noise ratio for a single-ended pulsed radar system with pulse compression.	99
50	Probability of Detection versus Range for a single-ended pulsed radar system with pulse compression. $f = 94$ GHz, $\alpha = 20$ dB/km, and $\sigma = 10$ m <sup>2</sup> .	100
51	Range versus Specific Attenuation for the single-ended pulsed radar system with pulse compression. $P_d = 0.995$ , $P_{fa} = 10^{-6}$ (Computed processed E/N = 17.79 dB.)	101
52	Range versus Rain Rate for the double-ended system with square-law detection. E/N = 10 dB and $T = 20^\circ\text{C}$ .	105

Figure		Page
53	Range versus Rain Rate for the single-ended system with square-wave modulation and square-law detection. $P_d = 0.995$ , $P_{fa} = 10^{-6}$ , $\sigma = 125 \text{ m}^2$ , and $T = 20^\circ\text{C}$ .	106
54	Range versus Rain Rate for the single-ended CW system with a quadrature receiver. $P_d = 0.995$ , $P_{fa} = 10^{-6}$ , $\sigma = 125 \text{ m}^2$ , and $T = 20^\circ\text{C}$ .	107
55	Range versus Rain Rate for the single-ended pulsed system with a quadrature receiver. $P_d = 0.995$ , $P_{fa} = 10^{-6}$ , $\sigma = 10 \text{ m}^2$ , and $T = 20^\circ\text{C}$ .	108
56	Range versus Rain Rate for the single-ended pulsed radar with pulse compression. $P_d = 0.995$ , $P_{fa} = 10^{-6}$ , $\sigma = 10 \text{ m}^2$ , and $T = 20^\circ\text{C}$ .	109
57	Range versus Rain Rate for the single-ended pulsed source range gated radar employing post-detection integration. $P_d = 0.995$ , $P_{fa} = 10^{-6}$ , $\sigma = 125 \text{ m}^2$ , and $T = 20^\circ\text{C}$ .	110
58	Range versus Liquid Water Content in fog for the single-ended CW system with a quadrature receiver. $P_d = 0.995$ , $P_{fa} = 10^{-6}$ , $\sigma = 125 \text{ m}^2$ , and $T = 20^\circ\text{C}$ .	112

## LIST OF TABLES

Table		Page
I	Input Data for Computer Algorithms	53
II	Calculated Complex Index of Refraction of Pure Water for Various Wavelengths and Temperatures	104

## SUMMARY

The effects of rain and fog are examined for three transmissometer and three radar systems: double-ended (direct path) with square-wave modulation and square-law detector, single-ended (folded path) with square-wave modulation and square-law detection, single-ended CW with quadrature receiver, single-ended pulsed with post-detection pulse integration, single-ended pulsed with quadrature receiver, and single-ended with linear FM pulse compression. Computer algorithms were developed to find the probability of detection as a function of range for the radar systems, and the signal-to-noise ratio as a function of range for the transmissometer systems. These algorithms are used recursively to determine the range at which specified performance is attained as a function of rain rate or fog liquid water content. Calculated results are presented for exponential drop-size distributions; provision has been made for the extension to other distributions.



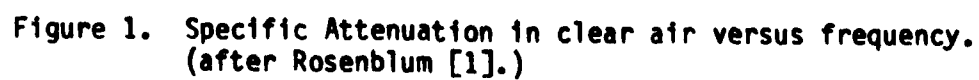
## SECTION I

### INTRODUCTION

The basic purpose of this study is to investigate the performance of transmissometers which could be used to measure the transmission over a path on which millimeter wave radars are simultaneously evaluated. For the most part, a detailed analysis of six different types of transmission systems was performed for frequencies of 35, 94, 140, and 240 Gigahertz (GHz). Three of these systems were transmissometers and three were radars that might be evaluated on the range. These frequencies have been selected because they represent the "windows" of low molecular absorption as shown below by Figure 1.

In this project two major problems were examined. First, we consider the problem of accurately modeling the attenuation through rain and fog due to scattering and absorption. These effects are characterized in terms of frequency and meteorological quantities such as rain and fog drop-size distributions, rain rate, temperature, and liquid water content.

Second, the six systems were analyzed in terms of the common performance parameters, false alarm probability and probability of detection for the radars and signal-to-noise ratio for transmissometers. Equations which predict the performance parameters at a specified range are derived. Then these equations are used to find the effect of



weather on this range at the various frequencies.

The term "double-ended" will be used to describe a system in which transmitter and receiver are separated and direct transmission occurs between them. A "single-ended" system is one in which the signal is reflected by a target to the receiver, which is located close to the transmitter.

In this project, the following transmissometer and radar systems were examined:

- (1.) Double-ended transmission path with audio (square-wave) modulation and square-law detection. Note this cannot be used as a radar. Analysis is not sensible for probability of detection because there is no target. Instead, a detailed analysis in terms of signal-to-noise ratio is performed.
- (2.) Single-ended transmission path with audio (square-wave) modulation, and square-law detection using a calibrated target. This is a transmissometer which could be used as a radar if range information is not required. Analysis in terms of signal-to-noise or probability of detection could be performed, however, signal-to-noise ratio analysis is more meaningful.
- (3.) Single-ended transmission path with audio modulation, quadrature detection and a calibrated target. Similar to the previous system, this is a transmissometer which could be used as a radar if range information is not required. Once again, signal-to-noise ratio analysis techniques are more useful, however, a probability of detection and probability of false

alarm can be defined since we do have a calibrated target.

(4.) Post-detection (boxcar) integration over a single-ended transmission path. This is a true radar. It could be used as a relatively inefficient transmissometer by ranging on a calibrated target. For this system, analysis in terms of probability of detection and probability of false alarm is useful.

(5.) Quadrature-detection over a single-ended transmission path. As with the previous system, this is a true pulsed radar which could be used as a relatively inefficient transmissometer. Once again, probability of detection and probability of false alarm is most useful for analysis of this system.

(6.) Pulse compression with quadrature detection over a single-ended transmission path. This radar system is identical to the previous system except pulse compression is used. This system can also be used as a transmissometer. As with the last system, probability of detection and probability of false alarm is most useful for analyzing this system.

The basic format of this thesis is such that expressions for signal-to-noise ratio are given in Section II. A derivation of expressions relating probability of detection to signal-to-noise ratio is given in Section III. Equations for calculating drop-size distributions and for determining the attenuation due to rain and fog are derived in Section IV. The results obtained from computer models using the equations derived in Sections II to IV are described in Section V.

## SECTION II

### DERIVATION OF SIGNAL-TO-NOISE EXPRESSIONS

In this section, the signal-to-noise ratio expressions for the six configurations of instrumentation discussed in Section I are derived. In Section II.A, the signal-to-noise ratio expressions are derived for a point in the receiver prior to any demodulation or nonlinear signal processing. Therefore, the expressions for signal-to-noise ratio correspond to the output signal of the intermediate frequency amplifier. These signal-to-noise expressions depend upon whether a one-way or a two-way transmission path is considered, however, they are independent of the type of signal detection. The detection process is considered in Section II.B. The expressions given in Sections II.A and II.B.1 to II. B.5 are based on Report AFWAL-TR-81-1281 [2].

#### A. Derivation of Pre-Detection Signal-to-Noise Ratio Expressions.

Each transmission configuration studied may be described in terms of one of the following groups:

- (1.) The system uses signal transmission over a one-way path.
- (2.) The receiver is located next to the transmitter and the signal from the transmitter is reflected from a calibrated target back to the receiver. This is a radar system but possibly without a requirement for range resolution (transmissometers.)

Let's consider the derivation of the signal-to-noise expressions for

each transmission system separately.

For a one-way path, the power density at the receiving antenna is

$$S_{re} = \frac{P_t G_t}{4\pi R^2} \quad (1)$$

where  $P_t$  = transmitted power,  
 $G_t$  = transmitter antenna gain in direction of the receiver,  
 and  $R$  = distance between transmitting and receiving antennas.

Therefore, the power received is given by

$$P_r = \frac{P_t G_t A_e}{4\pi R^2} \quad (2)$$

where  $P_r$  = power received by receiving antenna,  
 and  $A_e$  = effective aperture of receiving antenna.

The effective aperture of the receiving antenna is in units of area and may be defined as

$$A_e = \frac{G_r \lambda^2}{4\pi} \quad (3)$$

where  $G_r$  = gain of the receiver antenna in the direction of the transmitter,  
 $\lambda$  = wavelength of the signal.

The Friis transmission equation is obtained by combining Equations (2) and (3).

$$P_r = \frac{P_t G_t G_r \lambda^2}{(4\pi)^2 R^2} \quad (4)$$

If losses in the transmitter and receiver system, as well as attenuation factors such as rain or fog in the transmission path, are included, then the received power is given by

$$P_r = \frac{P_t G_t G_r \lambda^2 L_t L_r}{(4\pi)^2 R^2} 10^{\frac{-\alpha R}{10}} \quad (5)$$

where  $\alpha$  = specific attenuation in decibels per unit length,  
 $L_t$  = transmitter-to-transmitting antenna loss (expressed as efficiency),

$L_r$  = receiving antenna-to-receiver loss (expressed as efficiency.)

Now, if the thermal noise power at the pre-detection filter output signal (usually the intermediate frequency (IF) amplifier) is

$$\psi = kT_0BF \quad (6)$$

where  $k$  = Boltzman's constant ( $1.38 \times 10^{-23}$  Joules/°K),  
 $T_0$  = reference noise temperature (290 °K),  
 $B$  = effective pre-detection receiver filter bandwidth (Hz),  
 $F$  = receiver noise figure referenced to 290 °K,

an expression for the signal-to-noise ratio in the output signal of the intermediate frequency can be found. This signal-to-noise ratio for a one-way transmission path is determined by combining Equations (5) and (6). Thus, for propagation over a one-way path, the signal-to-noise is

$$\frac{S}{N} = \frac{P_t G_t G_r \lambda^2 L_t L_r}{(4\pi)^2 R^2 k T_0 B F} 10^{\frac{-\alpha R}{10}} \quad (7)$$

Now, consider systems of the radar type transmitting over a two-way path. The power density at the target is given as

$$S_t = \frac{P_t G_t}{4\pi R^2} 10^{\frac{-\alpha R}{10}} \quad (8)$$

If the radar cross section of the target is defined as  $\sigma$ , in units of area, the power reradiated in the receiver direction is

$$P' = \frac{P_t G_t \sigma}{4\pi R^2} 10^{\frac{-\alpha R}{10}} \quad (9)$$

Since propagation is over a two-way path, the power density of the echo signal at the receiving antenna is

$$S_r = \frac{P_t G_t \sigma}{(4\pi R^2)^2} 10^{\frac{-2\alpha R}{10}} \quad (10)$$

The received power is obtained by multiplying  $S_r$  by the effective aperture area. By use of Equation (3), the radar equation becomes

$$P_r = \frac{P_t G_t G_r \sigma \lambda^2}{(4\pi)^3 R^4} 10^{\frac{-2\alpha R}{10}} \quad (11)$$

Including effects of the losses in the transmitting and receiving system

$$P_r = \frac{P_t G_t G_r L_t L_r \lambda^2 \sigma}{(4\pi)^3 R^4} 10^{\frac{-2\alpha R}{10}} \quad (12)$$

Therefore, from Equations (6) and (12), the pre-detection signal-to-noise ratio for the radar transmissometer is

$$\frac{S}{N} = \frac{P_t G_t G_r L_t L_r \sigma \lambda^2}{(4\pi)^3 R^4 k T_0 B F} 10^{\frac{-2\alpha R}{10}} \quad (13)$$

Equation (7) gives the pre-detection signal-to-noise ratio for a one-way transmission path, whereas Equation (13) is for a two-way transmitter-receiver configuration.

## B. Derivation of the Processed Signal-to-Noise Ratio Expressions.

The six configurations described in Section I are examined to determine the signal-to-noise ratio after detection and signal processing.

### 1. One-way Transmission and Square-Law Detection.

This configuration transmits and receives a chopped signal over a one-way propagation path. As shown by the block diagram of the receiver in Figure 2, the received signal is heterodyned to form an intermediate frequency signal, amplified, detected by a square-law device, and



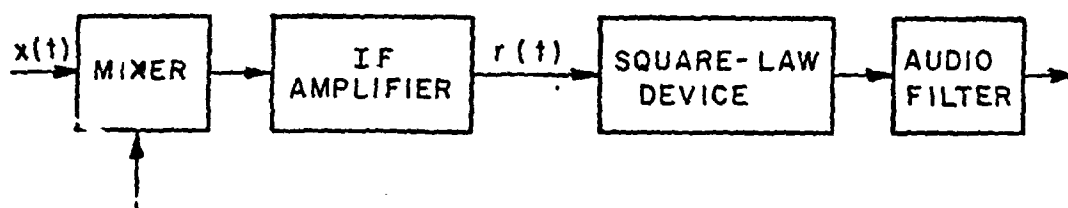


Figure 2. Receiver system with square-law detector.

filtered by a narrow-band (audio) filter. The signal-to-noise ratio expression given by Equation (7) applies to  $r(t)$ .

The chopped signal may be approximated as an amplitude-modulated signal with a modulation index ( $\mu$ ) of 100% since only the fundamental harmonic component is selected by the audio filter. Therefore, the input signal to the square-law device is given by

$$r(t) = A_c[1 + \mu \cos \omega_a t] \cos \omega_c t + n(t) \quad (14)$$

where  $A_c$  = carrier amplitude,  
 $\mu$  = modulation index,  
 $\omega_c$  = intermediate amplifier angular frequency,  
 $\omega_a$  = angular center frequency of audio filter.

The factor  $n(t)$  represents narrowband Gaussian noise with a spectral density determined by the spectral response of the intermediate frequency amplifier and centered at the intermediate angular frequency  $\omega_c$ . Typical values for  $\omega_a/2\pi$  and  $\omega_c/2\pi$  are 1 KHz and 1 GHz respectively.

With an input signal-to-noise as given by Equation (7), the signal-to-noise power ratio at the audio filter output signal is

$$(E/N) = \mu^2 [S/N]^2 [B_{if}/B_a] \{1 + [S/N](2 + \mu^2)\}^{-1} \quad (15)$$

where  $S/N$  = pre-detection signal-to-noise ratio given by Equation (7),  
 $B_{if}$  = equivalent rectangular bandwidth of the intermediate frequency amplifier, same as  $B$  in Equation (6),  
 $B_a$  = bandwidth of the audio filter.

Finally, the expression for signal-to-noise ratio of a system with a chopped waveform, modulation index of 100%, and square-law detection is

$$(E/N) = \frac{(S/N)^2 [B_{if}/B_a]}{1 + 3(S/N)} \quad (16)$$

where  $(S/N)$  is given by Equation (7).

## 2. Two-way Transmission and Square-Law Detection.

For this system, the receiver is identical to that of the system with one-way transmission and square-law detection previously discussed. However, in this case a reflective target produces the received signal. The processed signal-to-noise ratio is again given by Equation (16), but with (S/N) defined by Equation (13).

## 3. CW Signal Transmission with a Quadrature Receiver.

This receiving configuration consists of the transmission of a CW signal over a two-way path with the use of a reflecting target. However, a quadrature detector is used rather than a square-law device as in the previous system. A block diagram for a quadrature receiver is shown in Figure 3, where  $u(t)$  is the unit step function. This unit step function is included only to show that all integrators are reset at  $t=0$  (i.e., all earlier signals are disregarded.)

If the integrators, which are not continuously operating devices, are replaced with equivalent continuously operating filters as discussed below, then the unit step function  $u(t)$  should be omitted. In this case, the detector input signals are identical for Figures 2 and 3. For mathematical convenience, the integrators may be used when deriving the output signal-to-noise ratio.

Following Buyukdura [2] and Schwartz [3] to obtain the output signal-to-noise ratio, a single correlation detector is considered as shown in Figure 4a. The integrator output signal is given by

$$y(T) = \int_0^T r(t)s(t)dt . \quad (17)$$

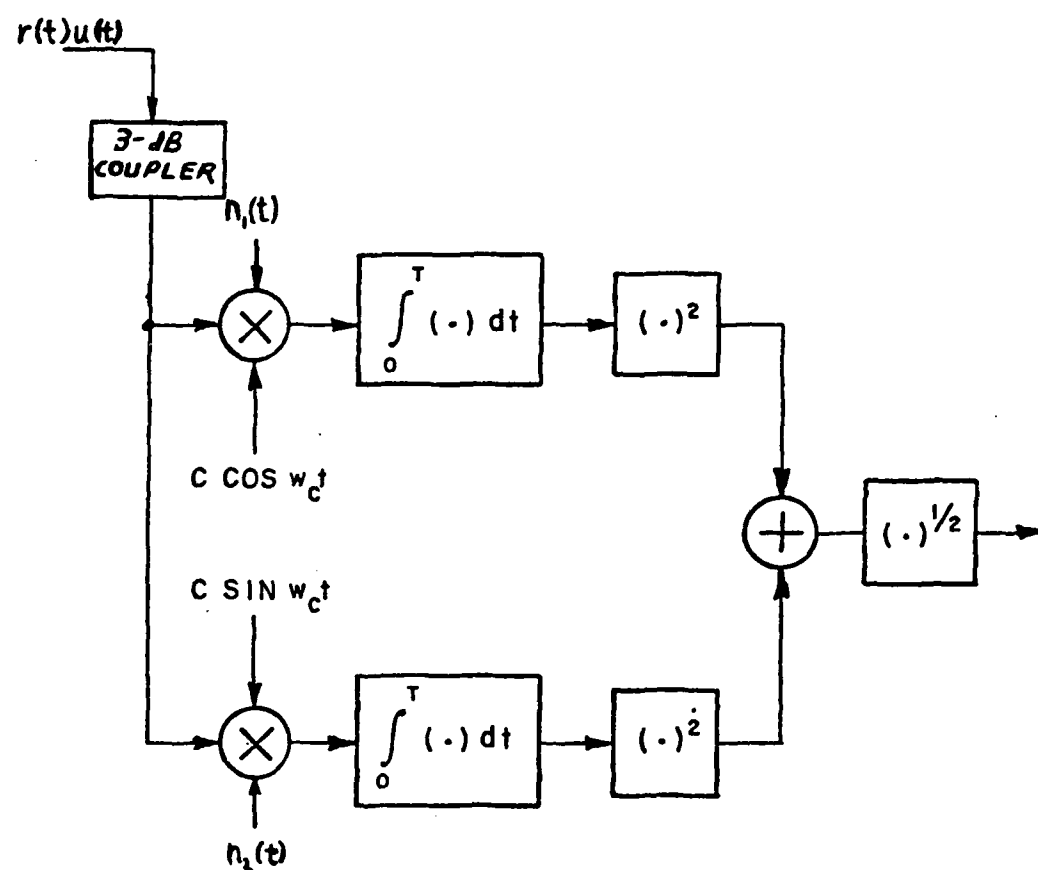
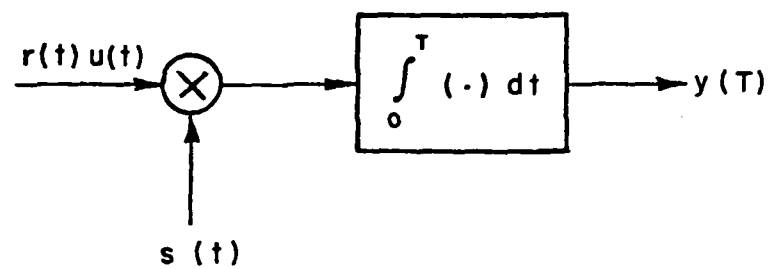
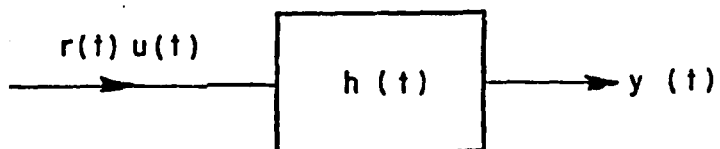


Figure 3. Quadrature receiver.



(a.)



(b.)

Figure 4. (a.) Correlation detector,  
(b.) Matched filter.

Now, consider the matched filter shown in Figure 4b. The filter output signal at  $t=T$  is given by the convolution

$$y(T) = r(t)u(t)*h(t), \quad (18)$$

that is,

$$y(T) = \int_{-\infty}^{\infty} r(t)u(t)h(T-t)dt. \quad (19)$$

However, the definition of the unit step function and the causality requirement for the filter requires

$$u(t) = 0, \quad t < 0 \quad (20)$$

and

$$h(T-t) = 0, \quad t > T. \quad (21)$$

The solution of Equations (20) and (21) with Equation (19) gives

$$y(T) = \int_0^T r(t)h(T-t)dt. \quad (22)$$

Note that if the filter response satisfies

$$h(T-t) = s(t), \quad 0 < t < T \quad (23)$$

or that

$$h(t) = s(T-t), \quad t > 0 \quad (24)$$

then  $y(T)$  is the same as for the correlation detector of Figure 4a.

From this figure, let's consider that the signals are

$$r(t) = A \cos \omega_c t \quad (25)$$

and

$$s(t) = C \cos \omega_c t. \quad (26)$$

From Equation (22), the filter impulse response which makes it equivalent to the integrator network must then be

$$h(t) = C \cos \omega_c (T-t). \quad (27)$$

If  $T$  is chosen to be an integer multiple of the period of  $r(t)$ , then Equation (26) is the impulse response of a matched filter. That is, when

$$T = \frac{2n\pi}{\omega_c} \quad n = 0, \pm 1, \pm 2, \dots$$

then Equation (26) becomes

$$h(t) = C \cos(2\pi n - \omega_c t) = C \cos \omega_c t = s(t). \quad (28)$$

Imposing the restrictions placed by Equations (20) and (21), one obtains

$$h(t) = C \cos \omega_c t \, u(t) \, u(T-t). \quad (29)$$

To specify the transfer function of the filter, we must find the Fourier transform of the impulse response. This can be found from

$$H(j\omega) = C \int_0^T \cos \omega_c t e^{j\omega t} dt. \quad (30)$$

Applying Euler's identity for  $\cos \omega_c t$ ,

$$H(j\omega) = \frac{C}{2} \int_0^T [e^{j\omega_c t} + e^{-j\omega_c t}] e^{j\omega t} dt$$

or

$$H(j\omega) = \frac{C}{2} \int_0^T [e^{j(\omega+\omega_c)t} + e^{j(\omega-\omega_c)t}] dt.$$

Performing the integration shows the transfer function of the filter to be of the form

$$H(j\omega) = \frac{CT}{2} \left[ e^{j(\omega+\omega_c)\frac{T}{2}} \frac{\sin(\omega+\omega_c)\frac{T}{2}}{(\omega+\omega_c)\frac{T}{2}} + e^{j(\omega-\omega_c)\frac{T}{2}} \frac{\sin(\omega-\omega_c)\frac{T}{2}}{(\omega-\omega_c)\frac{T}{2}} \right]. \quad (32)$$

Because the matched filter shown in Figure 4b is linear, the signal and noise components of the output signal may be examined separately.

The signal at the output can be obtained directly from the correlation detector of Figure 4a. and Equations (25) and (26) as

$$Y(T) = \int_0^T r(t)s(t)dt \quad (33)$$

$$= \int_0^T AC \cos^2 \omega_c t dt$$

$$Y(T) = \frac{ACT}{2} . \quad (34)$$

This expression for  $Y(T)$  can be used to define an expression for the signal power (normalized to a characteristic impedance of 1 ohm) by

$$P_s = [ACT/2]^2 . \quad (35)$$

According to Haykin [4] and Taub and Schilling [5], the noise power at the output is

$$P_{ny} = \frac{1}{2\pi} \int_{-\infty}^{\infty} S_{ny}(\omega) d\omega \quad (36)$$

where  $S_{ny}(\omega)$  is the power spectral density of the noise component of  $Y(T)$ . It is given in terms of the power spectral density of the noise component at the input by

$$S_{ny}(\omega) = S_{nr} |H(\omega)|^2 . \quad (37)$$

If one assumes a filter with a rectangular bandwidth  $B$  of unit amplitude, the noise power referred to the output is given by

$$P_{ny} = \frac{1}{2\pi} \int_{-\infty}^{\infty} S_{nr} |H_{rect}(\omega)|^2 d\omega = kT_0 B F \quad (38)$$

Then, assuming a flat input noise power spectral density, from Equations (36) and (38) we have

$$S_{nr}(\omega) \approx \frac{kT_0 F}{2} \quad (39)$$

at the input. Using  $H(j\omega)$  as defined by Equation (32), the output



noise power is given by

$$P_{ny} = \frac{1}{2\pi} S_{nr} \int_{-\infty}^{\infty} |H(\omega)|^2 d\omega. \quad (40)$$

If we assume  $\omega_c \gg \frac{2\pi}{T}$  in Equation (32), we can approximate the noise power by

$$P_{ny} \cong \frac{1}{\pi} S_{nr} \left[ \frac{C^2 T^2}{4} \right] \int_0^{\infty} \frac{\sin^2(\omega - \omega_c) \frac{T}{2}}{\left[ (\omega - \omega_c) \frac{T}{2} \right]^2} d\omega. \quad (41)$$

By a simple change of variables, this integral can be put into the familiar form of  $\text{sinc}(x)$ , i.e.,

$$P_{ny} \cong \frac{1}{\pi} S_{nr} \left[ \frac{C^2 T^2}{4} \right] \left[ \frac{2}{T} \right] \int_{-\omega_c T/2}^{\infty} \text{sinc}^2 x \, dx. \quad (42)$$

Evaluating this integral with the restriction of  $\omega_c > \frac{2\pi}{T}$ , we have

$$P_{ny} \cong \frac{1}{\pi} S_{nr} \left[ \frac{C^2 T^2}{4} \right] \int_{-\infty}^{\infty} \text{sinc}^2 x \, dx = S_{nr} C^2 \frac{T}{2}. \quad (43)$$

Using Equation (39), the output noise power can be obtained as

$$P_{ny} = \frac{kT_0 F C^2 T}{4}. \quad (44)$$

Now, consider an input signal with an unknown phase

$$r(t) = A \cos(\omega_c t + \theta) \quad (45)$$

applied to the quadrature receiver of Figure 3. It can be shown by reasoning similar to that which led to Equation (44) that the noise power at the output is given by

$$P_n = 2FkT_0 C^2 \frac{T}{4},$$

and that the desired signal power at the output of the system is again given by Equation (35). Therefore, we have

$$\begin{aligned}
\frac{E}{N} &= \frac{P_s}{P_n} = \frac{[ACT/2]^2}{2FkT_0C^2T} = \frac{A^2T}{2kFT_0} \\
&= \frac{SB_{if}T}{N} \\
\frac{E}{N} &= [S/N]TB_{if} \quad (46)
\end{aligned}$$

where (S/N) is given by Equation (13). Equation (46) is the required signal-to-noise expression for a quadrature receiver after signal processing has been employed.

#### 4. Pulsed Source with Incoherent Pulse Integration.

This configuration represents a pulsed-source range-gated radar. Such a radar can be used as a transmissometer by measuring the reflection from a calibrated target such as a corner reflector.

At the receiver, the signal is heterodyned to form an intermediate frequency signal, passed through a detector and sampled sequentially by range gates. The purpose of each range gate is to quantize the radar return into range intervals. Each range gate opens in sequence just long enough to sample the signal voltage corresponding to a different range interval along the propagation path. In general, the range gate acts as a switch (or gate) which opens and closes at a proper instant of time. These gates are activated once for each pulse-repetition interval and produce a series of pulses of constant amplitude at the gate output when using a stationary target.

The output of the range gates is passed through a circuit called a box-car device which integrates (sums) the pulses. Basically, the box-car device is a sample and hold circuit which stretches each pulse in

time to cover the entire repetition period. The purpose of using a box-car device is to aid in the filtering and detection process by emphasizing the fundamental of the modulation frequency and eliminating harmonics of the pulse repetition frequency.

The receiver system now examined uses incoherent (post-detection) integration rather than coherent (pre-detection) integration. In post-detection integration, a smaller signal-to-noise ratio exists when compared to pre-detection integration. This is due primarily to the non-linear nature of the detector which creates a rectifying effect and causes harmonic distortion that decreases the available signal power.

If pre-detection were used and 'n' pulses of the same signal-to-noise ratio were integrated, then the resulting signal-to-noise power ratio would be identically 'n' times that of a single pulse. However, for post-detection integration, a smaller signal-to-noise power ratio would be found. In fact, we can account for the reduced signal-to-noise ratio after integration by using

$$\frac{E}{N} = nE_i(n) \left[ \frac{S}{N} \right] \quad (47a)$$

where  $E_i(n)$  is the integration efficiency factor defined by Marcum [6] as

$$E_i(n) = \frac{[S/N]_1}{n[S/N]_n} \quad (47b)$$

Here,  $[S/N]_1$  is the signal-to-noise ratio of a given pulse required to yield a specified probability of detection, and  $[S/N]_n$  is the value of signal-to-noise ratio of a single pulse required to achieve the same probability of detection when 'n' similar pulses are integrated.  $E_i(n)$  has been calculated by Marcum [6] and plotted by Skolnik [7]. The plots

shown in Figure 5 are for the integration improvement factor  $I = nE_i(n)$  and integration loss  $L = 10 \log_{10}[1/E_i(n)]$  both versus 'n', the total number of pulses integrated.

For the present, consider  $[S/N]_n$  in Equation (47b) to be equal to  $[S/N]$  in Equation (47a). We see when 'n' such pulses are integrated to give the same probability of detection as one pulse with a signal-to-noise ratio of  $[S/N]_1$  this value is approximately the same as the total signal-to-noise ratio of n pulses,  $[E/N]$  in Equation (47a). In general, the signal-to-noise expression with 'n' integrated pulses can be given by

$$[S/N]_n = \frac{P_t G_t G_r \lambda^2 \alpha L_t L_r}{(4\pi)^3 R^4 k T_0 B F} 10^{\frac{-2\alpha R}{10}} \quad (48)$$

To use this equation it is necessary to use a set of curves as shown in Figure 5 for each value of 'n'. Therefore, combining Equations (47b) and (48) yields

$$[E/N] = \frac{P_t G_t G_r \lambda^2 \alpha L_t L_r n E_i(n)}{(4\pi)^3 R^4 k T_0 B F} 10^{\frac{-2\alpha R}{10}} \quad (49)$$

where  $E_i(n)$  comes from Figure 5. Note in this figure that  $n_f$  is the false alarm number and relates to false alarm probability by  $n_f = 1/P_{fa}$ . This will be important in probability of detection calculations to be discussed in Section III.

##### 5. Pulsed Source with a Quadrature Receiver.

This configuration is a true pulsed radar which uses a range gated quadrature receiver. That is, the input to Figure 4a is given as

$$s(t) = C p(t) \cos \omega_c t \quad (50)$$

Here  $p(t)$  is a unit amplitude pulse train of width  $\tau$  and repetition period  $T_r$  contained in the time interval  $(0, T)$ . The output  $Y(T)$  of Figure

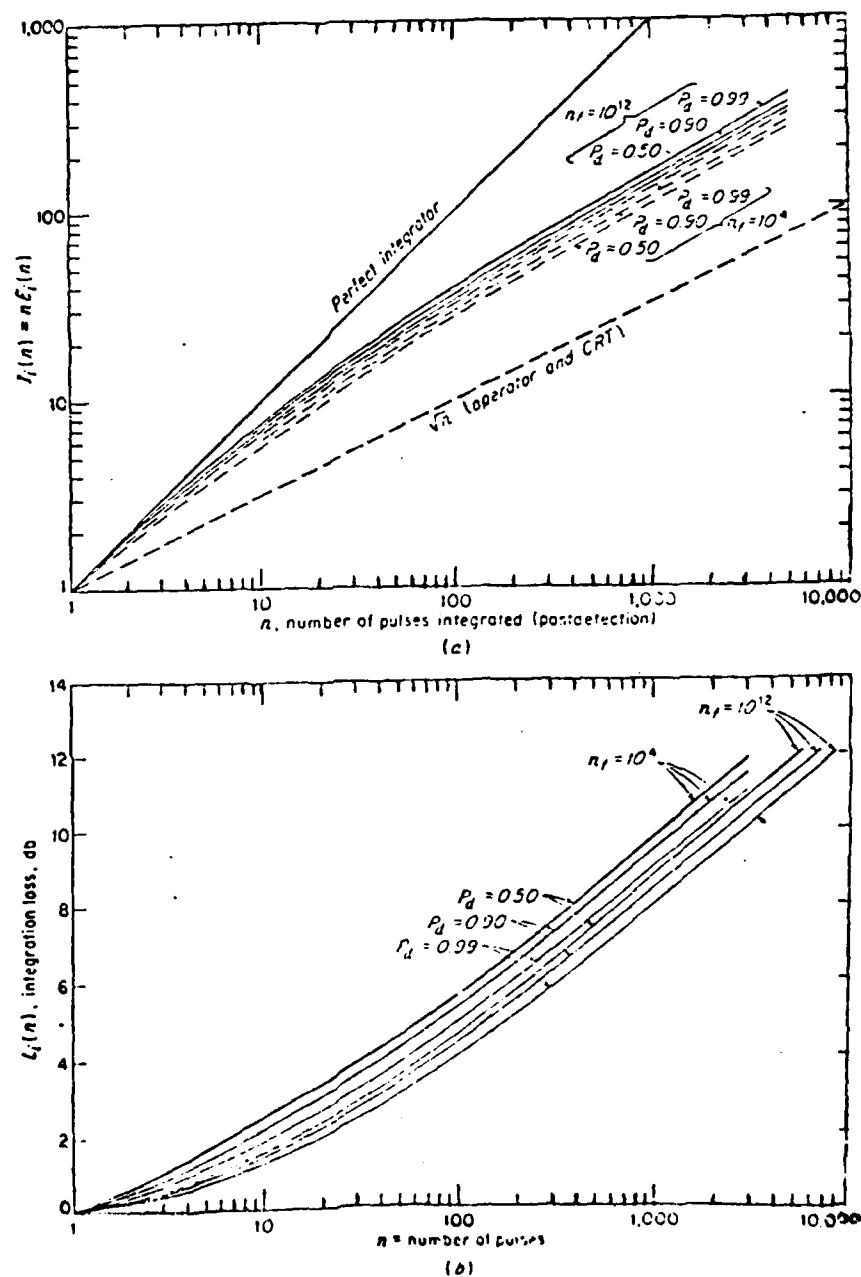


Figure 5. ( a.) Integration Improvement Factor,  
 ( b.) Integration loss versus number of  
 pulses integrated. (after Skolnik  
 [7].)

4a is then

$$Y(T) = \int_0^T s(t)r(t)p(t) dt = \frac{ACTd}{2} \quad (51)$$

where  $d$  is the duty cycle of the signal, described as

$$d = \tau/T_r \quad (52)$$

This integral for  $Y(T)$  can be used to define an expression for the signal power by a method analogous to Equation (35). That is,

$$P_s = [ACTd/2]^2 \quad (53)$$

Once we choose convenient values for  $\tau$ ,  $T_r$ , and  $T$ , the impulse response of the equivalent filter of Figure 4b is

$$h(t) = Cp(t)\cos\omega_c t \quad (54)$$

in order to match the input signal  $s(t)$ .

If the filter were matched only to one pulse of duration  $\tau$ , we could use Equation (44) for noise power at the output, i.e.,

$$P_\tau = \frac{kT_0FC^2\tau}{4} \quad (55)$$

If we define the number of integrated pulses as

$$n = T/T_r \quad (56)$$

then the noise power of the filter output signal with impulse response given by Equation (54) is

$$P_n = \frac{kT_0FC^2\tau n}{4} \quad (57)$$

Therefore, the signal-to-noise ratio at the system output is

$$\frac{E}{N} = \frac{P_s}{P_n} = \frac{[A^2 C^2 \tau / 2 T_r]^2}{\frac{F k T_0 C^2 \tau (T/T_r)}{4}} = \frac{[A/2]^2 T \tau}{\frac{F k T_0 T_r}{4}} .$$

Since the power of a sine wave of amplitude A into a 1-ohm load is given by  $S=A^2/2$ , then the processed signal-to-noise ratio for a single coherently detected channel is

$$\frac{E}{N} = \frac{2STdB_{if}}{N}$$

where  $[S/N]$  is defined by Equation (13).

However, in practice we will not know the phase, so we must use a quadrature receiver.

Note that the quadrature receiver produces a signal-to-noise ratio at the output that is just one-half as large as the phase-coherent detector of Figure 4, this occurs because the 2-phase detectors have one channel processing one component of signal and its associated noise component, and the other channel processing the quadrature signal and its associated quadrature noise component. Therefore, we end up with the effects of the received signal and two noise components, which halves the output signal-to-noise ratio, i.e.,

$$\frac{E}{N} = \frac{STdB_{if}}{N} \quad (58)$$

gives the signal-to-noise ratio at the system output. Note this equation is very similar to Equation (46) except we are including a duty cycle for the pulse.

#### 6. Pulsed Source with Linear FM Rectangular-Envelope Pulse Compression.

This transmission configuration is the pulsed source range-gated

radar discussed in Section II.B.5. However, the transmitted signal is on during most of the entire repetition period but swept in frequency. At the receiver, after the signal is heterodyned to an intermediate frequency, it is passed through a matched pulse compression filter and detected as shown in Figure 6 [8].

If the carrier frequency of a transmitted pulse is linearly swept, a pulse compression filter can be used to delay one end of the pulse relative to the other. At the filter output, this produces a narrowed pulse of greater peak amplitude. The linear time-delay characteristic of the filter acts to delay the high-frequency components at the start of the input pulse more than the low-frequency components at the end of the pulse. The frequency components experience a proportional delay so that the net result is a time compression of the pulse. The effects of pulse compression are summarized in Figure 7.

It can be shown, as in Appendix B, the pre-detection signal-to-noise ratio for the radar transmissometer is

$$\frac{S}{N} = \frac{P_t K G_t G_r L_t L_r \sigma \lambda^2}{(4\pi)^3 R^4 k T_0 B F} 10^{\frac{-2\alpha R}{10}} \quad (59)$$

where  $K$  is the pulse compression ratio defined by

$$K = T/\tau \quad (60)$$

where  $T$  and  $\tau$  are defined in Figure 7. The ratio of pulse widths before and after pulse compression is shown in Figure 8.

If we consider a pulse compression radar with a quadrature receiver system as in Section II. B.5, then the output signal-to-noise ratio can be found from Equation (58) to be



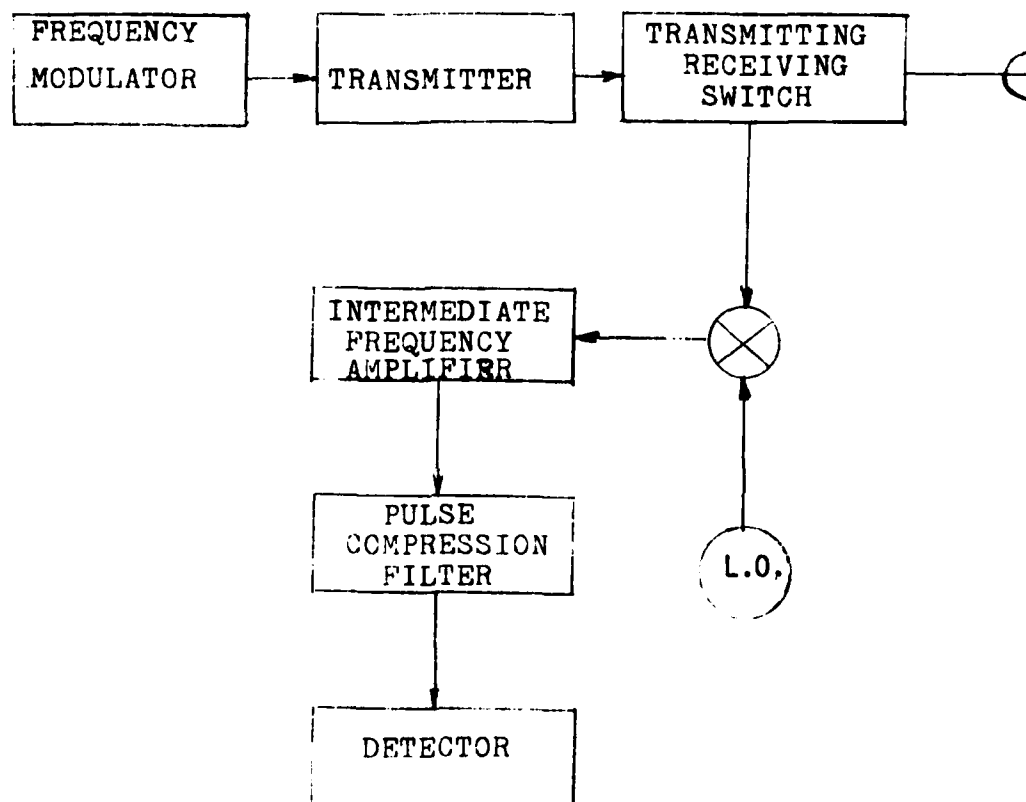


Figure 6. Typical Intrapulse Linear Frequency Pulse Compression Radar.

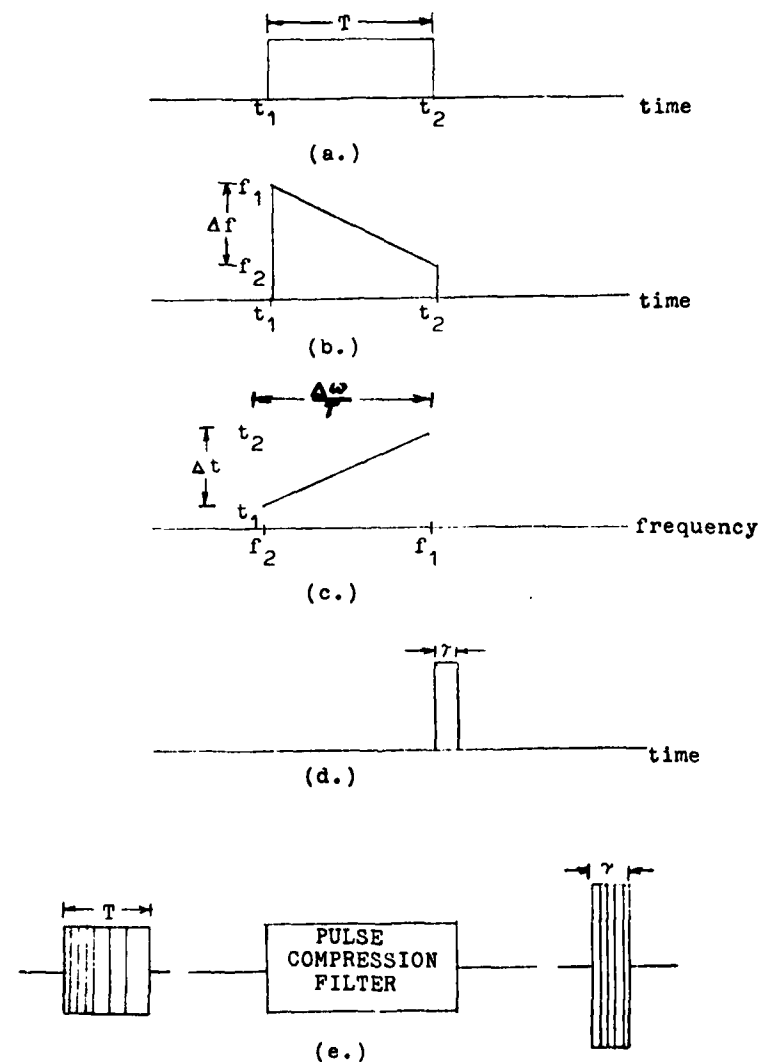


Figure 7. Idealized Pulse Compression Characteristics. (a.) Wide-pulse envelope, (b.) Carrier frequency modulation, (c.) Filter time-delay characteristics, (d.) Compressed pulse envelope, (e.) Input-output waveforms of compression filter.

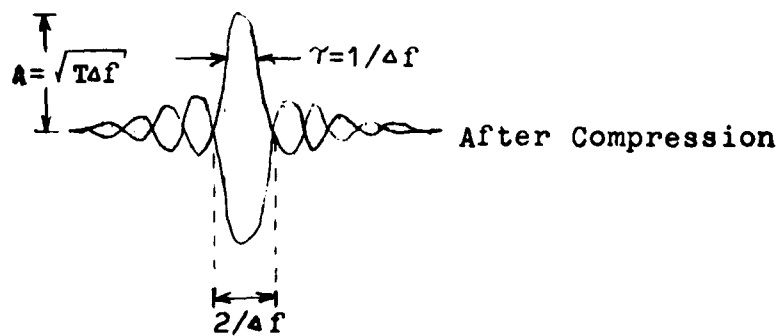
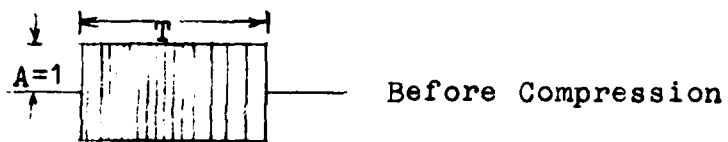


Figure 8. Wide-pulse and Compressed Pulse Waveforms.

$$\frac{E}{N} = \frac{P_t K G_t G_r L_t L_r \sigma \lambda^2 T_d B_{if}}{(4\pi)^3 R^4 k T_0 B_F} 10^{\frac{-2\alpha R}{10}}. \quad (61)$$

#### D. Summary

In this section, signal-to-noise ratio expressions before signal processing were derived in Section II.A for both double-ended and single-ended systems, they are given by Equations (7) and (13).

Also, post-detection signal-to-noise ratio expressions for the six systems were derived in Section II.B. These signal-to-noise ratio expressions are given by Equations (16), (46), (49), (58), and (61). In all cases, the pre-detection signal-to-noise ratios to be used are those derived in Section II.A.

Pre-detection signal-to-noise ratios are denoted by S/N and post-detection signal-to-noise ratios denoted by E/N.

Note that all the equations derived in this section are dependent on the attenuation parameter  $\alpha$ . A derivation of equations for  $\alpha$  will be given in Section IV for attenuation in rain and fog.

## SECTION III

### DERIVATION OF PROBABILITY OF DETECTION

For transmissometers, the output (post-detection) signal-to-noise ratio is probably the most useful specification of performance. For radars, most radar designers prefer to use a specification of probability of detection and probability of false alarm rather than signal-to-noise ratio. Thus, in this section a derivation of expressions for the probability of detection as a function of signal-to-noise ratio will be presented. Since the signal-to-noise ratio is directly related to range as shown by the equations in Section II, it will be possible to derive probability of detection expressions in terms of range for given system parameters and meteorological conditions. In addition, a specification of false alarm probability must be given. The discussion presented in this section is related closely to the modified Neyman-Pearson detection theory described by Skolnik [9].

The method presented in this section is derived with the assumption of either a square-law or linear detector since the effect on the detection probability by assuming one instead of the other is small. We will also apply this technique to quadrature detection systems since the probability of detection will be only a function of processed signal-to-noise ratio and false alarm probability.

#### A. Description of Noise in the Radar System.

To successfully define the probability of detection in terms of

signal-to-noise ratio (or range) we need a suitable representation of the noise. One of the best noise models is discussed by Skolnik where we consider narrowband Gaussian noise which is both amplitude and phase modulated. For instance, if we let  $\tilde{n}(t)$  represent the random noise function (where  $\sim$  denotes a random variable), then set

$$\tilde{n}(t) = \tilde{g}(t)\cos[\omega_c t + \tilde{\phi}(t)] \quad (62)$$

where  $\tilde{g}(t)$  and  $\tilde{\phi}(t)$  are random variables representing amplitude and phase which vary slowly when compared to the cosine factor. Thus,

$$\tilde{n}(t) = \tilde{g}(t)\cos\tilde{\phi}(t)\cos\omega_c t - \tilde{g}(t)\sin\tilde{\phi}(t)\sin\omega_c t. \quad (63)$$

However, these leading terms are simply time varying random variables. To simplify the notation, consider

$$\tilde{a}(t) = \tilde{g}(t)\cos\tilde{\phi}(t) \quad (64)$$

and

$$\tilde{b}(t) = \tilde{g}(t)\sin\tilde{\phi}(t), \quad (65)$$

so that

$$\tilde{g}(t) = [\tilde{a}^2(t) + \tilde{b}^2(t)]^{1/2} \quad (66)$$

$$\tilde{\phi}(t) = \tan^{-1} \frac{\tilde{b}(t)}{\tilde{a}(t)}. \quad (67)$$

Therefore, the noise function can be represented as

$$\tilde{n}(t) = \tilde{a}(t)\cos\omega_c t - \tilde{b}(t)\sin\omega_c t. \quad (68)$$

From a careful examination of the statistical properties of typical receiver noise, it has been found that

- (1.) The random variables  $\tilde{a}(t)$  and  $\tilde{b}(t)$  are statistically

independent. Since they are uncorrelated, it follows that

$$E[\tilde{a}(t)\tilde{b}(t)] = 0.$$

- (2.) The mean values  $E[\tilde{a}(t)] = E[\tilde{b}(t)]$  are zero, and the variances  $E[\tilde{a}^2(t)] = E[\tilde{b}^2(t)]$  are equal to a constant  $\psi_0$ .

Therefore, we can write the signal input to the detector in the form

$$y(t) = [f(t) + \tilde{a}(t)]\cos\omega_c t - \tilde{b}(t)\sin\omega_c t \quad (69a)$$

if a signal is present, and

$$y(t) = \tilde{a}(t)\cos\omega_c t - \tilde{b}(t)\sin\omega_c t \quad (69b)$$

if no signal is present. For a pulsed signal,

$$f(t) = \begin{cases} A & |t| < T/2 \\ 0 & |t| > T/2 \end{cases} \quad (70)$$

represents the constant amplitude of a pulse. For a CW signal,  $A/\sqrt{2}$  represents the r.m.s. amplitude of the carrier when  $f(t)=A$  is used.

If  $y(t)$  is passed through a noncoherent detector (such as a half or full-wave rectifier followed by a low pass filter,) then all phase information is lost in the detection process. The output of the detector,  $r(t)$ , assuming unity gain in the detection process will be given by

$$r(t) = \{[f(t) + \tilde{a}(t)]^2 + [\tilde{b}(t)]^2\}^{1/2} \quad (71)$$

if a signal is present, and

$$r(t) = \{\tilde{a}(t)^2 + \tilde{b}(t)^2\}^{1/2} \quad (72)$$

if no signal is present.

#### B. Derivation of the Probability of Detection.

For our work, we are primarily interested in Type II error. This error occurs during the detection process if we decide no signal is

present when it actually is present. If we choose an arbitrary threshold level  $V_T$ , the probability of having a Type II error can be defined as

$$P_{od} = \int_0^{V_T} p(r(t)) dr \quad (73)$$

and the probability of detection defined as

$$P_d = \int_{V_T}^{\infty} p(r(t)) dr \quad (74)$$

where  $p(r)$  is the probability density function of  $r(t)$ , which will be assumed to be a Gaussian random variable. We can describe the probability of detection and probability of Type II error as shown in Figure 9.

Also, for convenience in the notation, let's consider

$$\tilde{z}(t) = f(t) + \tilde{a}(t) \quad (75)$$

in Equation (69a). Since the random variables  $\tilde{a}(t)$  and  $\tilde{b}(t)$  are statistically independent, it follows that  $\tilde{z}(t)$  and  $\tilde{b}(t)$  are also independent. Therefore, Equation (69a) becomes

$$r(t) = \{[\tilde{z}(t)]^2 + [\tilde{b}(t)]^2\}^{1/2} \quad (76)$$

when a signal is present.

Now, consider the case where  $f(t)=A$  for a pulsed radar. Then  $\tilde{z}(t)=A+\tilde{a}(t)$  is a Gaussian random variable with mean  $A$ . That is,

$$E[\tilde{z}(t)] = E[A] + E[\tilde{a}(t)] = A \quad (77)$$

since  $E[\tilde{a}(t)]=0$  and the expected value of a constant is the value of the constant. Also, we can show

$$E[(\tilde{z}(t)-A)^2] = E[\tilde{a}^2(t)] = \psi_0. \quad (78)$$

From the bottom of page 30, we see  $E[\tilde{b}^2(t)] = \psi_0$ . Since we have shown



$E[z(t)] = A$  and  $E[b(t)] = 0$ , we can write the probability density functions for  $\tilde{z}(t)$  and  $\tilde{b}(t)$  as

$$p[\tilde{z}(t)] = \frac{1}{\sqrt{2\pi\psi_0}} e^{-\frac{[\tilde{z}(t)-A]^2}{2\psi_0}}$$

and

$$p[\tilde{b}(t)] = \frac{1}{\sqrt{2\pi\psi_0}} e^{-\frac{[\tilde{b}(t)]^2}{2\psi_0}} .$$

However, since  $\tilde{a}(t)$  and  $\tilde{b}(t)$  are uncorrelated, we can show  $\tilde{z}(t)$  and  $\tilde{b}(t)$  are independent, i.e.,

$$\begin{aligned} E[\tilde{z}(t)\tilde{b}(t)] &= E[(\tilde{a}(t)+A)\tilde{b}(t)] = E[\tilde{a}(t)\tilde{b}(t)] + E[A\tilde{b}(t)] \\ &= AE[\tilde{b}(t)] \end{aligned}$$

so

$$E[\tilde{z}(t)\tilde{b}(t)] = 0 .$$

Knowing  $\tilde{z}(t)$  and  $\tilde{b}(t)$  are independent, we see the joint probability density function can be expressed as the product

$$p[\tilde{z}(t)\tilde{b}(t)] = p[\tilde{z}(t)]p[\tilde{b}(t)] .$$

That is, the joint probability density function becomes

$$p[\tilde{z}(t)\tilde{b}(t)] = \frac{1}{2\pi\psi_0} e^{-\frac{[\tilde{z}(t)-A]^2 + \tilde{b}^2(t)}{2\psi_0}} . \quad (79)$$

We wish to convert this expression into a density function in terms of  $\tilde{r}(t)$  at the output of the noncoherent detector.

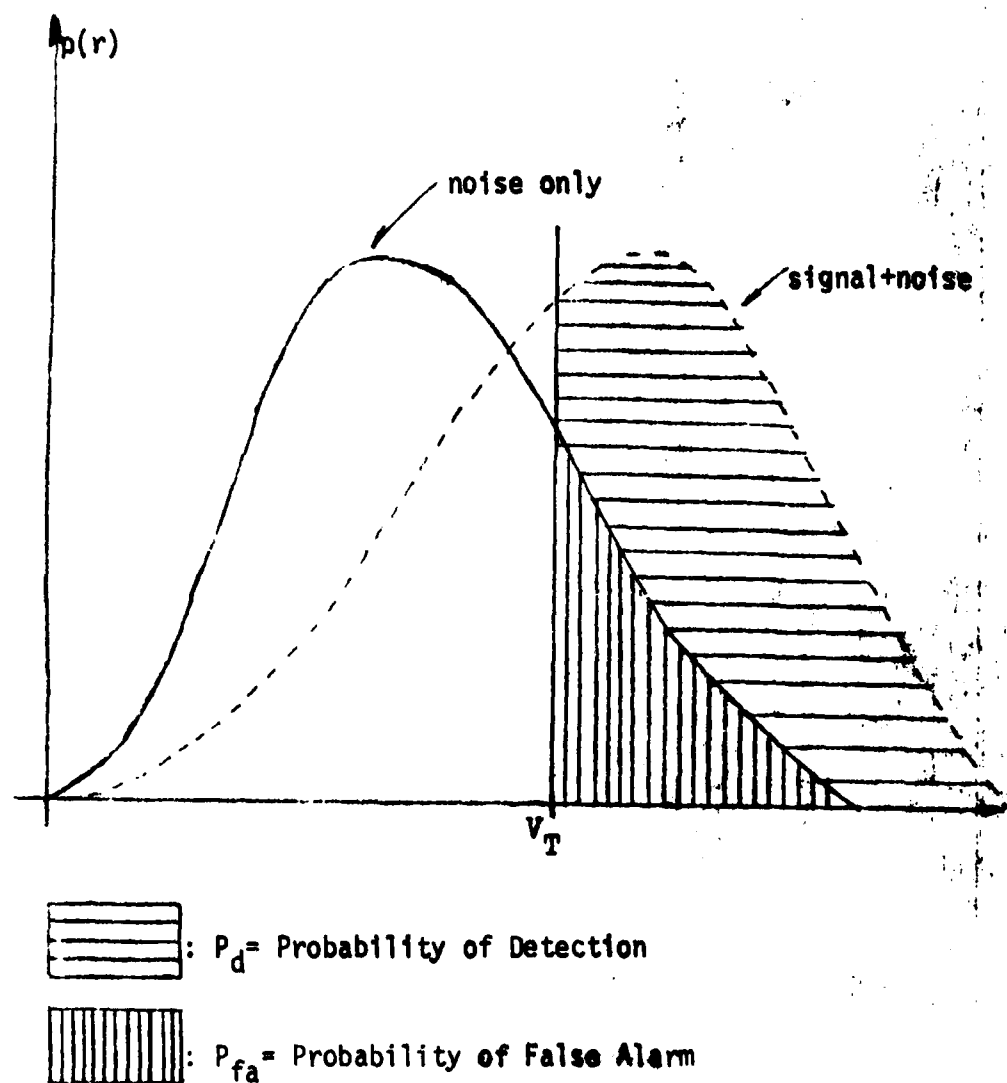


Figure 9. Probability of Detection and Probability of False Alarm in terms of density function plot  $p(r)$ .

Suppose we consider the two random variables  $\tilde{z}(t)$  and  $\tilde{b}(t)$  as rectangular coordinates. Then we are able to convert to polar coordinates where computations are much easier. This is equivalent to using the polar representation of the noise given by Equation (66) and (67).

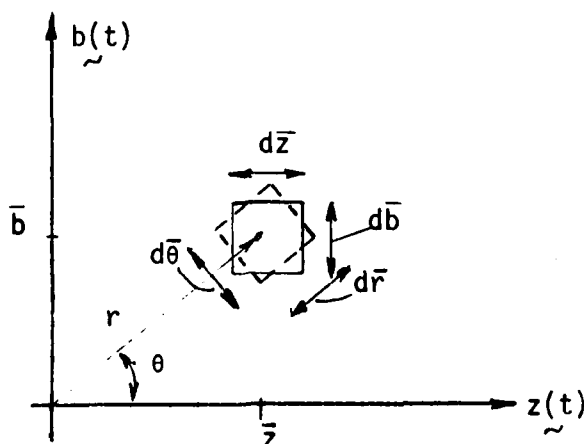
By Equation (79), we actually mean

$$p\left[\tilde{z}-\frac{d\tilde{z}}{2} < \tilde{z}(t) < \tilde{z}+\frac{d\tilde{z}}{2}, \tilde{b}-\frac{d\tilde{b}}{2} < \tilde{b}(t) < \tilde{b}+\frac{d\tilde{b}}{2}\right] = \frac{1}{2\pi\psi_0} e^{-\left[\frac{[\tilde{z}-A]^2 + \tilde{b}^2}{2\psi_0}\right]} d\tilde{z} d\tilde{b}. \quad (80)$$

This defines the probability of finding  $\tilde{z}(t)$ ,  $\tilde{b}(t)$  in the small neighborhood  $\tilde{z}, \tilde{b}$  in a cartesian system. We can transform to polar coordinates by using

$$\tilde{z} = \tilde{r} \cos \theta \quad \tilde{b} = \tilde{r} \sin \theta$$

so the elemental area  $d\tilde{z}d\tilde{b}$  becomes  $\tilde{r}d\tilde{r}d\theta$ . These coordinate transformations are sketched in the drawing below.



Therefore, we can write

$$p\left[\tilde{r}-\frac{d\tilde{r}}{2} < \tilde{r} < \tilde{r}+\frac{d\tilde{r}}{2}, \theta-\frac{d\theta}{2} < \theta < \theta+\frac{d\theta}{2}\right] = \frac{1}{2\pi\psi_0} e^{-\left[\frac{[\tilde{r}\cos\theta-A]^2 + [\tilde{r}\sin\theta]^2}{2\psi_0}\right]} \tilde{r}d\tilde{r}d\theta$$

or

$$\begin{aligned}
 p(r, \theta) &= \frac{r}{2\pi\psi_0} e^{-\left[\frac{[r\cos\theta-A]^2 + [r\sin\theta]^2}{2\psi_0}\right]} \\
 &= \frac{r}{2\pi\psi_0} e^{-\left[\frac{r^2 + A^2 - 2rA\cos\theta}{2\psi_0}\right]} \quad (81)
 \end{aligned}$$

Now, the total probability of finding  $r$  between  $\bar{r} - \frac{d\bar{r}}{2}$  and  $\bar{r} + \frac{d\bar{r}}{2}$  corresponds to a ring of width  $\bar{r}$  about the circle  $r = \bar{r}$ . Therefore,

$$\begin{aligned}
 p(r) &= \int_0^{2\pi} p(r, \theta) d\theta = \int_0^{2\pi} \frac{r}{2\pi\psi_0} e^{-\left[\frac{r^2 + A^2 - 2rA\cos\theta}{2\psi_0}\right]} d\theta. \\
 p(r) &= \int_0^{2\pi} p(r, \theta) d\theta = \frac{r}{\psi_0} e^{-\left[\frac{r^2 + A^2}{2\psi_0}\right]} \frac{1}{2\pi} \int_0^{2\pi} e^{\left[\frac{rA\cos\theta}{\psi_0}\right]} d\theta. \quad (82)
 \end{aligned}$$

This latter integral is defined as the modified Bessel function of the first kind and order zero with argument  $Ar/\psi_0$ . That is,

$$p(r) = \frac{r}{\psi_0} e^{-\left[\frac{r^2 + A^2}{2\psi_0}\right]} I_0[Ar/\psi_0] \quad (83)$$

Now, knowing the probability density function  $p(r)$ , we can calculate the probability of detection via Equation (74).

$$P_d = \int_{V_T}^{\infty} p(r) dr = \int_{V_T}^{\infty} \frac{r}{\psi_0} e^{-\left[\frac{r^2 + A^2}{2\psi_0}\right]} I_0[Ar/\psi_0] dr \quad (84)$$

This integral is evaluated by Skolnik [9] in terms of an infinite sum, so that

$$P_d = \frac{1}{2} \left[ 1 - \operatorname{erf} \left( \frac{V_T - A}{\sqrt{2\psi_0}} \right) \right] + \frac{e^{-\frac{(V_T - A)^2}{2\psi_0}}}{2A \sqrt{\frac{2\pi}{\psi_0}}} \left\{ 1 - \frac{V_T - A}{4A} + \frac{1 + \frac{(V_T - A)^2}{\psi_0}}{8A^2} - \dots \right\} \quad (85)$$

Note:  $\operatorname{erf}(z)$  is the error function defined as

$$\operatorname{erf}(z) = \frac{2}{\sqrt{\pi}} \int_0^z e^{-u^2} du \quad (86)$$

A valid series approximation to Equation (85) can be found when we choose a sensible threshold, i.e.,  $(V_T - A)^2 / \psi_0 < 1$  and we have a good signal-to-noise ratio so  $A^2 / \psi_0 \gg 1$ . If these conditions are valid, as often occurs for fairly large signal-to-noise ratios, we can use

$$P_d = \frac{1}{2} \left[ 1 - \operatorname{erf} \left( \frac{V_T - A}{\sqrt{2\psi_0}} \right) \right] + \frac{e^{-\frac{(V_T - A)^2}{2\psi_0}}}{2A \sqrt{\frac{2\pi}{\psi_0}}} \left\{ 1 - \frac{V_T - A}{4A} + \frac{1 + \frac{(V_T - A)^2}{\psi_0}}{8A^2} \right\}. \quad (87)$$

According to Skolnik, if we examine the envelope of the IF sine wave rather than the signal after detection, it is then possible for the equation for probability of detection to be converted to a power relationship by defining signal-to-noise ratio at the output of the detector as  $E/N$ . That is,

$$\frac{E}{N} = \frac{\text{Power in Signal}}{\text{Power in Noise}} = \begin{cases} [A/\sqrt{\psi_0}]^2 & \text{for a pulsed signal} \\ [A/\sqrt{2\psi_0}]^2 & \text{for a CW signal.} \end{cases} \quad (88)$$

Using these relationships, we can see

$$P_d = \frac{1}{2} \left[ 1 - \operatorname{erf} \left( \frac{\frac{V_T}{A} - 1}{\sqrt{\frac{2}{E/N}}} \right) \right] + \frac{e^{-\frac{1}{2} \frac{E}{N} \left( \frac{V_T}{A} - 1 \right)^2}}{\sqrt{8\pi [E/N]}} \left\{ 1 - \frac{1}{4} \left( \frac{V_T}{A} - 1 \right) + \frac{1}{8} \left[ \frac{1}{[E/N]} + \left( \frac{V_T}{A} - 1 \right)^2 \right] \right\} \quad (89)$$

where  $[E/N] \gg (A/V_T)^2$  for a pulsed signal and  $[E/N] \gg (A/2V_T)^2$  for a CW

signal. We will see in Section V that Equation (89) proves to be accurate for signal-to-noise ratios in excess of 0 dB.

### C. Derivation of Probability of False Alarm.

The probability of false alarm is the probability that the threshold voltage is exceeded when no signal is present. Commonly called Type I error, the false alarm probability is defined by the integral

$$P_{fa} = \int_{V_T}^{\infty} p(r) dr \quad (90)$$

where  $p(r)$  is given by Equation (83) when no signal is present. Because  $I(Ar/\psi_0)=1$  when there is no signal, we find

$$p(r) = \frac{r}{\psi_0} e^{-\frac{r^2}{2\psi_0}}. \quad (91)$$

This probability density function is commonly known as the Rayleigh density function.

Substituting Equation (91) into (90) and integrating gives

$$P_{fa} = e^{-\frac{V_T^2}{2\psi_0}} \quad (92)$$

for false alarm probability. Using Equation (89) allows a definition of probability of false alarm in terms of signal-to-noise ratios at the output of the detector. That is,

$$P_{fa} = \begin{cases} e^{-\frac{V_T^2[E/N]}{2A^2}} & \text{for pulse signal} \\ e^{-\frac{V_T^2[E/N]}{A^2}} & \text{for CW signal} \end{cases} \quad (93)$$

Solving this equation for the ratio of  $V_T/A$ , yields

$$\frac{V_T}{A} = \begin{cases} \sqrt{\frac{2 \ln(1/P_{fa})}{[E/N]}} & \text{for pulse signal} \\ \sqrt{\frac{1 \ln(1/P_{fa})}{[E/N]}} & \text{for CW signal.} \end{cases} \quad (94)$$

Substitution of Equation (94) into Equation (89) allows us to obtain a probability of detection in terms of a specified false alarm probability and processed signal-to-noise ratio.

The processed signal-to-noise expressions  $(E/N)$  have been derived in Section II.B. as a function of system parameters. Therefore, once the radar system designer has specified a probability of false alarm, the required threshold ratio can be determined from equation (94) and the probability of detection from Equation (89). Or, as often is needed, the radar designer may desire to specify both probability of detection and a probability of false alarm. In this case, the required signal-to-noise ratio at the detector output can be calculated and the range at which it is equalled or exceeded can be found. Both methods will be discussed with graphs and computer algorithms in Section V.

Typical plots showing probability of detection as a function of signal-to-noise ratio or range are shown below in Figures 10 and 11. In both cases a specification of false alarm probability must be given. Figure 10 can be plotted by using Equation (89). Figure 11 is plotted by using Equation (89) and the signal-to-noise ratio expressions as a function of range derived in Section II. Therefore, for all of the radar systems, we can plot probability of detection either in terms of signal-to-noise ratio or range for a fixed probability of false alarm.

Finally, the proper choice of the signal-to-noise ratio given by

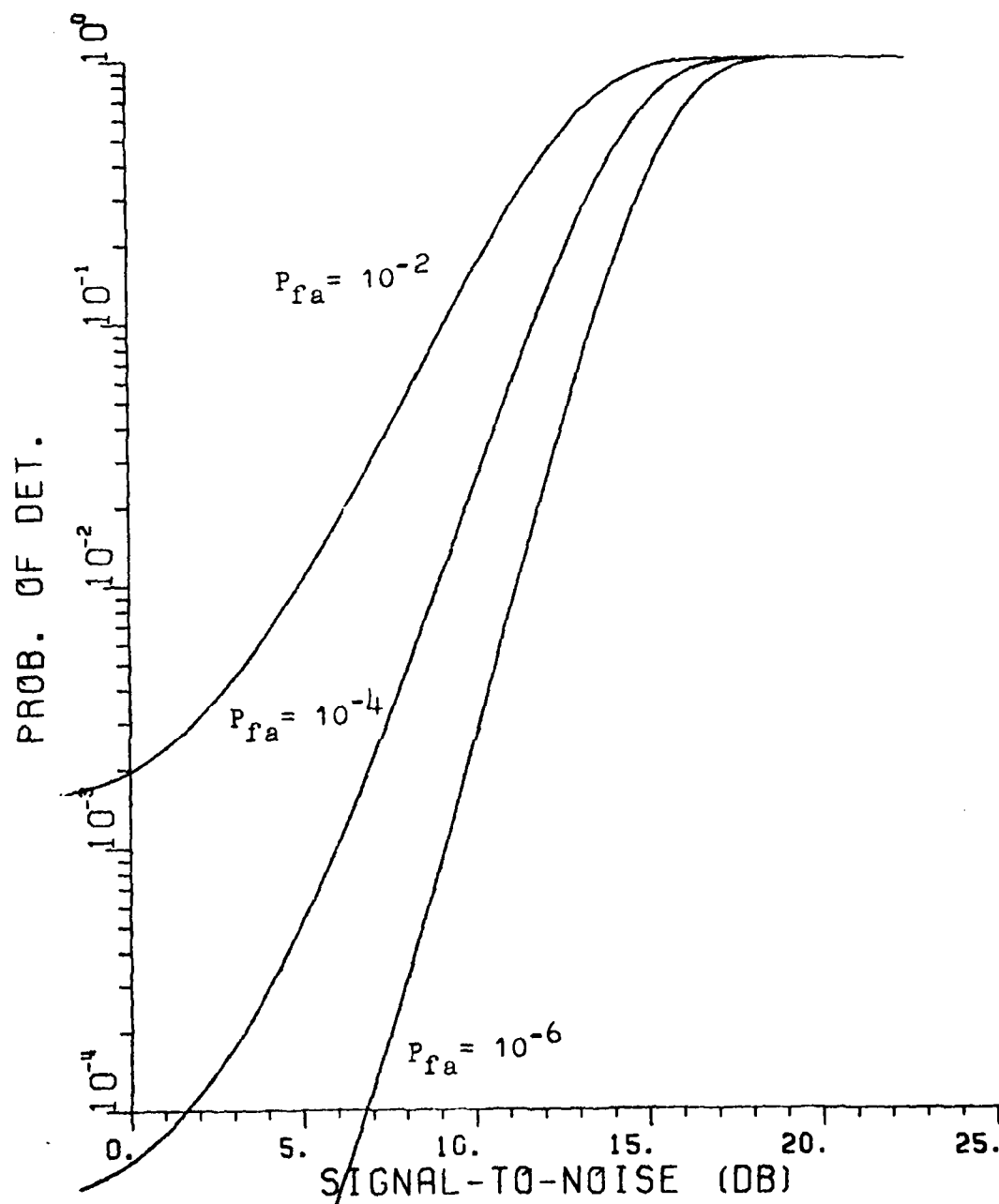


Figure 1). Typical plot of Probability of Detection versus Signal-to-Noise Ratio for a specified Probability of False Alarm.



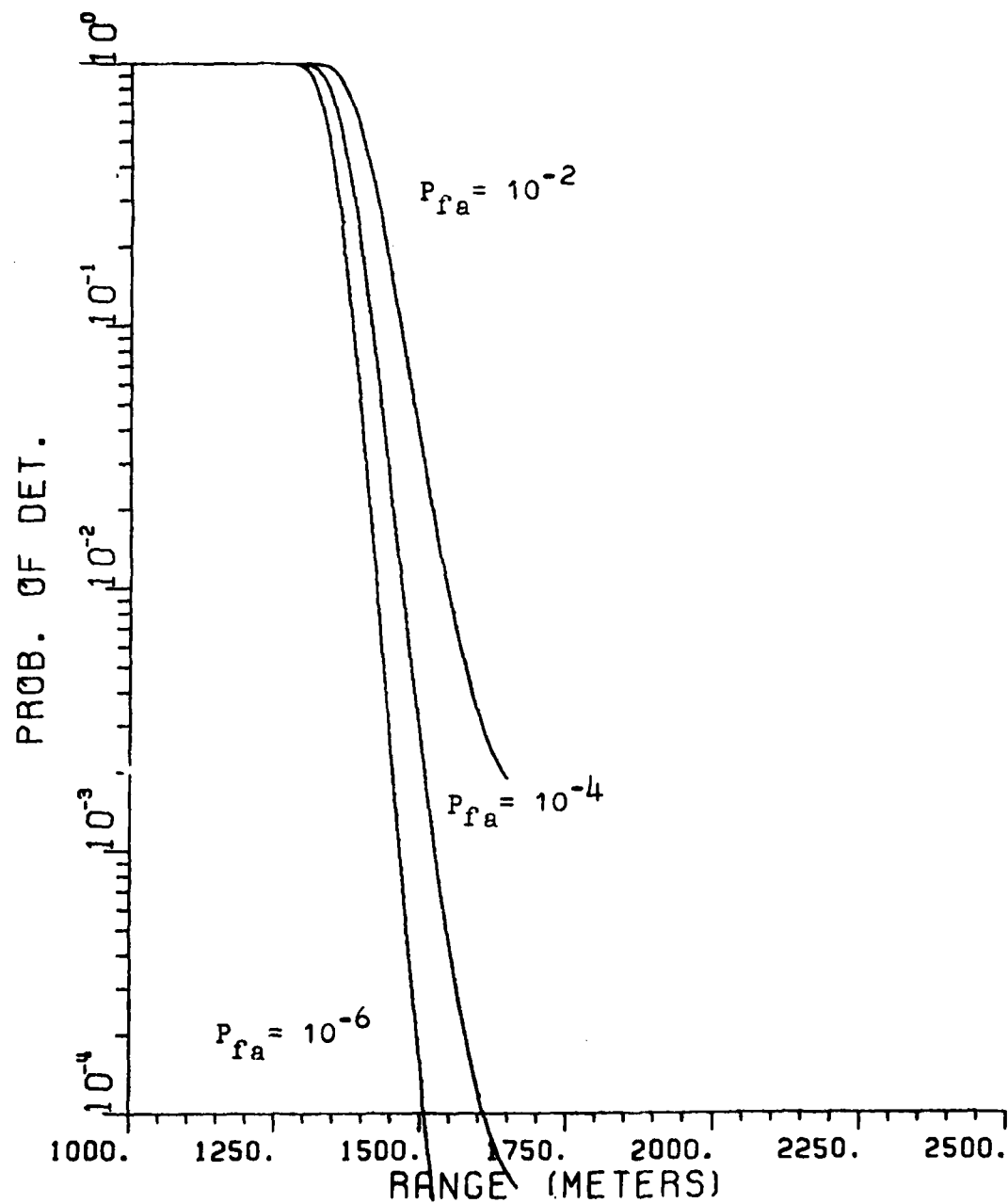


Figure 11. Typical plot of Probability of Detection versus Range for a specified Probability of False Alarm.

Equation (88) will be given for each system discussed in Section II.

The derivation of the equations for probability of detection deals only with the envelope of the IF output signal, which is a sine wave. Therefore,  $A$  is the amplitude of the IF signal in the absence of noise and  $S=A^2/2$  is the power in the IF channel due to signal when a pulse is present.

For the two-way transmission and square-law detection system of Section II.B.2, we use a "chopped" signal with square-law detector followed by an audio filter. In Equation (16), we have  $S$  representing the carrier power at the output of the intermediate frequency amplifier and  $E$  representing  $E_p^2/2$  where  $E_p$  is the peak value of the audio sine wave. If we consider that this audio wave will be envelope detected, then this reflects Equation (88) be used for a CW signal and  $E=A^2/2$ . Therefore, in  $S/N$  for this system, interpret  $P_t$  as the carrier power so for "chopped" signal and square-law detection use the bottom right side of Equations (88) and (94).

For the CW signal transmission with a quadrature receiver of Section II.B.3, the post-detection "power" was obtained by taking a sample of signals with mean value of  $A^2$ , i.e.,  $E=A^2$ . Therefore, in  $S/N$  for this system, interpret  $P_t$  as the carrier power which is equal to the average or peak power. In this case, use the top right side of Equation (88) to determine post-detection signal-to-noise ratio  $E/N$ .

For the pulsed source system with incoherent pulse integration discussed in Section II.B.4, the pre-detection  $S/N$  refers to a sine wave signal and  $P_t$  represents the peak power radiated during a pulse. If  $A$  is the envelope of the IF signal in the absence of noise, then  $S=A^2/2$

is the power in the IF channel due to signal when a pulse is present. In this case, use the bottom right side of Equations (88) and (94).

For the pulsed source with quadrature receiver of Section II.B.5 and the pulsed source with linear FM rectangular envelope pulse compression of Section II.B.6, the same reasoning applies to  $E/N$  as to the CW signal and quadrature receiver discussed above. In each of these cases, the post-detection "power" was taken from a sample of signals. That is,  $P_t$  is the peak power transmitted during a pulse so that  $S=A^2/2$  (i.e.,  $S=(A^2\cos\theta)/2$  in one channel and  $S=(A^2\sin\theta)/2$  in the other channel) leads to Equation (58). In the pulse compression case, the peak and average power are the same if pulse width before pulse compression  $T$ , equals the repetition period  $T_r$ . Once again, the peak power transmitted during a pulse is  $S=A^2/2$ . For these two cases, we use the top right side of Equations (88) and (94) for the probability of detection calculation.

## SECTION IV

### ATTENUATION DUE TO RAIN AND FOG

The attenuation parameter  $\alpha$  in the signal-to-noise ratio expressions is highly dependent upon weather conditions and frequency. Approximate values at sea level in clear air are shown in Figure 1, but they are subject to variation because the absorption by oxygen and water vapor changes substantially with weather conditions. Even more pronounced is the attenuation due to rain and fog for which we now wish to present a model.

For our path attenuation model, assume that rain and fog consist of small spherical water droplets of complex refractive index to account for dissipation and scattering effects. The scattering effects from a sphere were examined in detail by Mie [10], are presented in an excellent tutorial book by Kerker [11], and have been recently utilized in propagation algorithms by Buyukdura [2]. Therefore, a detailed examination of these scattering effects will not be given in this thesis. Instead the work by Buyukdura will be modified to include effects of frequency and temperature on the complex index of refraction for water. These effects are discussed in an article by Peter S. Ray [12]. Corrections to this article are given by [13] and the calculations for the complex index of refraction in terms of frequency and temperature are shown in Appendix A.

In general, the attenuation factor caused by a spherical drop-size distribution using the extinction efficiency factor is given by Buyukdura [2] as

$$\alpha = 4.343 \int_0^{\infty} Q_{EXT}(a)N(a)da \quad (95)$$

where  $\alpha$  is specific attenuation in dB/km,  $a$  is droplet radius in meters,  $N(a)$  is the volume density of droplets with radius  $a$  in units of  $[m^3 \cdot mm]^{-1}$  and  $Q_{EXT}$  is the extinction efficiency factor

$$Q_{EXT} = \frac{-2}{(k_0 a)^2} \sum_{n=1}^{\infty} (2n+1) [Re(a_n + b_n)]. \quad (96)$$

Here  $k_0$  is the wave number in free space, and  $a_n$ ,  $b_n$  are the spherical Mie coefficients defined in Equations (A63) and (A64) of Buyukdura [2].

#### A. Dropsize Distribution for Rain.

For our work, we will use a Marshall-Palmer dropsize distribution of the form

$$N(a) = N_0 e^{-2\Lambda a} \quad (97)$$

where  $\Lambda = \alpha_1 R^\beta (\text{mm}^{-1})$ ,  
 $N_0 = 8000 [\text{drops}/(\text{m}^3 \cdot \text{mm})]$ ,  
 $\alpha_1 = 4.1$ ,  
 $\beta = 0.21$ ,

and  $R$  is the rain rate in mm/hr,  $a$  is the droplet radius in mm. Therefore, substituting Equations (96) and (97) into Equation (95) gives an expression for the extinction

$$\alpha = \alpha_0 + 4.343 \int_0^{\infty} Q_{EXT}(a)N(a)da \quad (\text{dB/km}) \quad (98)$$

where the constant  $\alpha_0 = 0.02$  dB/km at 35 GHz,  $\alpha_0 = 0.3$  dB/km at 94 GHz,  $\alpha_0 = 1.4$  dB/km at 140 GHz, and  $\alpha_0 = 4$  dB/km at 240 GHz in clear atmosphere [14]

#### B. Dropsize Distribution for Fog.

Dropsize distributions for advection fogs near seacoasts have been

extensively studied in the works of Kunkel [15] and Mallow [16]. We have found no detailed analyses for radiative fogs common in the midwest United States. Therefore, the description of a fog presented in this section is based upon a sparse advection fog model derived by Kunkel.

A widely used dropsize distribution is based upon Kunkel [15]

$$N(A) = CA^{\alpha'} e^{-\frac{\alpha' A}{\gamma}} \quad (99)$$

where  $N(A)$  is the number density of droplets of relative radius  $A=a/R_m$ . Here,  $a$  is the actual radius of the fog droplet and  $R_m$  is the drop radius with the maximum number density in the distribution. The normalization constant is generally determined from the integral

$$\begin{aligned} N &= R_m \int_0^{\infty} N(A) dA \\ &= R_m C \int_0^{\infty} A^{\alpha'} e^{-\frac{\alpha' A}{\gamma}} dA \end{aligned} \quad (100)$$

which can be solved for  $C$  as

$$C = \frac{\mp N \gamma}{R_m} \left[ \frac{\alpha' + 1}{\gamma} \right] \frac{1}{\Gamma \left[ \frac{\alpha' + 1}{\gamma} \right]} \quad (101)$$

where  $N$  is the total number of droplets in the distribution scaled to conform to the total liquid water content of a given fog. Note that the (+) sign is used when  $\alpha'$  and  $\gamma$  are positive. Likewise, the (-) sign is used when  $\alpha'$  and  $\gamma$  are negative.

As Equations (99) and (101) are given, we must determine the scaling factor used to conform to the total liquid water content of the fog. The liquid water content,  $D$ , i.e., mass per unit volume, is given by

$$D = \rho \int_0^{\infty} \frac{4\pi a^3}{3} N(a) da$$

where  $a$  is the actual droplet radius and  $\rho$  is the density of water, then

$$D = \rho R_m^4 \int_0^{\infty} \frac{4\pi A^3}{3} N(A) dA \quad (102)$$

we see

$$\frac{N}{D} = \frac{R_m \int_0^{\infty} N(A) dA}{\rho R_m^4 \int_0^{\infty} \frac{4\pi A^3}{3} N(A) dA} \quad (103)$$

or

$$N = \frac{D R_m \int_0^{\infty} N(A) dA}{\rho R_m^4 \int_0^{\infty} \frac{4\pi A^3}{3} N(A) dA} \quad (104)$$

Substituting Equation (99) and integrating gives  $N$  as a function of liquid water content and relative droplet radius.

$$N = \frac{D R_m \int_0^{\infty} C A^{\alpha'} e^{-\frac{\alpha' A}{\gamma}} dA}{\frac{4\pi \rho R_m^4}{3} \int_0^{\infty} A(3+\alpha') e^{-\frac{\alpha' A}{\gamma}} dA} \quad (105)$$

which can be solved in closed form as

$$N = \frac{D R_m}{\frac{4\pi \rho R_m^4}{3}} \frac{[\alpha'/\gamma]^{(3/\gamma)}}{\Gamma[(4+\alpha')/\gamma]} \frac{\Gamma[(1+\alpha')/\gamma]}{\Gamma[(4+\alpha')/\gamma]} .$$

Substituting into Equation (101) and then into Equation (99) shows

$$N(A, D) = \mp \frac{D |\gamma|}{\frac{4\pi \rho R_m^4}{3}} \frac{[\alpha'/\gamma]^{[(4+\alpha')/\gamma]}}{\Gamma[(4+\alpha')/\gamma]} A^{\alpha'} e^{-\frac{\alpha' A}{\gamma}} \quad (106)$$

for the drop-size distribution in fog. Malow has examined several fogs and has determined  $\alpha'$ ,  $\gamma$ , and  $R_m$  for a light advection fog to be

$$\begin{aligned} R_m &= 15 \text{ } \mu\text{m} \\ \alpha' &= -2.20 \\ \gamma &= -4.54 \end{aligned}$$

which yields units of  $N(A,D)$  in droplets/ $(\mu\text{m})^4$ .

We intend to use the method presented by Buyukdura to determine the attenuation factor. This requires the units of  $N(A,D)$  to be in droplets/ $\text{m}^3 \cdot \text{mm}$  for  $D$  and  $\rho$  in  $\text{g}/\text{m}^3$  and  $a$  in  $\mu\text{m}$ . Therefore, we see

$$N(A,D) = \mp \frac{D |\gamma| 10^{21}}{\frac{4\pi\rho R_m^4}{3}} \frac{[\alpha/\gamma]^{[(4+\alpha)/\gamma]}}{\Gamma[(4+\alpha)/\gamma]} A^\alpha e^{\frac{-\alpha A}{\gamma}} \quad (107)$$

in droplets/ $(\text{m}^3 \cdot \text{mm})$ . Substituting  $\alpha'$ ,  $\gamma$ , and  $R_m$  with the knowledge that  $A=a/R_m$  and  $\rho=10^6 \text{ g}/\text{m}^3$  gives.

$$N(a,D) = 2.9536602 \times 10^{10} D a^{-2.2} e^{-1.0588176 \times 10^5 a^{-4.54}} \quad (108)$$

in droplets/ $(\text{m}^3 \cdot \text{mm})$  for  $a$  in  $\mu\text{m}$ .

We will allow  $D$  to vary between 0.021 and 0.148  $\text{g}/\text{m}^3$  and  $a$  to vary between 10 and 60  $\mu\text{m}$  for a useful algorithm to calculate attenuation by fog. Equation (108) will be substituted into Equation (98) for the calculation of the extinction factor for fog. Finally, this model does not include effects of multiple scattering from each fog droplet.



## SECTION V

### RESULTS AND DISCUSSION

The purpose of this thesis is to compare the performance of three types of transmissometers and three types of radar systems as a function of meteorological conditions in the millimeter-wave windows at 35, 94, 140, and 240 GHz. For the radars, a reasonable criterion is the range at which they would be effective, i.e., at which a specified high detection probability would be achieved, subject to a reasonable false alarm probability. For the transmissometers, the corresponding criterion is the range at which a reasonable signal-to-noise ratio will be achieved. These range criteria have the desirable feature that they do not depend strongly on the detailed system parameters, especially when attenuation due to rain or fog is strong. The plots of range versus rain rate or fog density will be found in Figures 52 through 58; they are discussed in more detail in Sections V.B and V.C, respectively. Other useful criteria, such as signal-to-noise ratio and detection probability as functions of range, are calculated in the process; these will be discussed and sample results will be presented as they are encountered in the discussion.

For each of the six types of instrumentation discussed in Section II, the signal-to-noise ratio before signal processing is computed as a function of range by use of Equation (7) for double-ended systems and Equation (13) for single-ended systems. The range  $R$  is varied from 500

meters to 8 kilometers by increments of 100 meters. Then, one of Equations (16), (46), (49), (58), and (61), as appropriate for the particular system, is used to calculate the signal-to-noise ratio after detection.

In our system calculations, the propagation path is assumed to be uniform, or to be comprised of layers each with homogeneous specific attenuation. The overall effect of these layers is seen by substitution of  $\sum_i \alpha_i R_i$  for  $\alpha R$  in Equations (7) and (13). For the summation,  $\alpha_i$  is the specific attenuation and  $R_i$  is the one-way path length through the the  $i$ th layer.

Computer algorithms were also developed to calculate and plot the probability of detection as a function of processed signal-to-noise ratio, and as a function of range for each of the radar systems. In these radar detection calculations, a specification of probability of false alarm and radar cross section area must be given. These algorithms use Equations (7) and (13) to calculate signal-to-noise ratio before signal processing. Then one of Equations (16), (46), (49), (58), or (61) depending upon the specific type of system is used to determine the signal-to-noise ratio after detection and signal processing. Using the results presented in Section III, the false alarm probability and the processed signal-to-noise expressions can be used in Equation (94) to yield  $V_T/A$ , and the probability of detection is then computed according to Equation (89).

Also, computer routines have been implemented to calculate and plot the maximum attainable range as a function of specific attenuation  $\alpha$ , rain rate, or liquid water content in fog. From the specification of a

fixed probability of detection and probability of false alarm, Equations (89) and (94) are solved for the processed signal-to-noise ratio by a search technique which increases  $E/N$  from a value of 1.0 in steps of 0.001 until the desired value of  $P_d$  is reached. Then specific attenuation is varied from 30 to 0 dB/km in increments of -0.1 dB/km. From the signal-to-noise ratio expressions before signal processing, an iterative solution for maximum range can be determined for large values of  $\alpha$  by using Equations (7) and (13). From Equation (7), an iterative solution for range is given by

$$R_{n+1} = \frac{10}{\alpha} \left[ \log_{10} \left[ \frac{P_t G_t G_r \lambda^2 L_t L_r}{(4\pi)^2 k T_0 B F (S/N)} \right] - 2 \log_{10} R_n \right] \quad (109)$$

for  $n$  an integer. In this equation,  $S/N$  is the signal-to-noise ratio at the output of the intermediate frequency amplifier corresponding to the processed signal-to-noise ratio for a fixed probability of detection and probability of false alarm. By a similar approach, propagation systems over a two-way path can use Equation (13) to solve for range so that

$$R_{n+1} = \frac{10}{2\alpha} \left[ \log_{10} \left[ \frac{P_t G_t G_r \lambda^2 L_t L_r \sigma}{(4\pi)^3 k T_0 B F (S/N)} \right] - 4 \log_{10} R_n \right] \quad (110)$$

In these iterative solutions, for  $\alpha=30$  dB/km, the iterations begin with  $R_0=0$  m. For all other values of specific attenuation, the solution corresponding to the preceeding  $\alpha$  value  $R(\alpha+0.1)$  is used for  $R_0$ . In all cases, the iterations were terminated when  $|R_{n+1}-R_n| < 1$  m. As previously stated, this method was found by Buyukdura to converge only for large values of specific attenuation.

A different iterative scheme is used for small values of  $\alpha$  when Buyukdura's method described by Equations (109) and (110) fails. For this case, the range  $R$  appearing in the denominator of Equation (7) is used on the left hand side of the equation. That is, for the two-ended system

$$R_{n+1} = \sqrt{\frac{P_t G_t G_r \lambda^2 L_t L_r}{(4\pi)^2 k T_0 B F (S/N)}} 10^{\frac{-\alpha R_n}{20}}. \quad (111)$$

Similarly, for systems of the radar type, Equation (13.) leads to

$$R_{n+1} = \sqrt{\frac{P_t G_t G_r \lambda^2 L_t L_r \sigma}{(4\pi)^3 k T_0 B F (S/N)}} 10^{\frac{-2\alpha R_n}{40}}. \quad (112)$$

Again,  $R(\alpha+0.1)$  was taken for the first value of  $R$  to be used on the right-hand side of the equation and the iterations were terminated when  $|R_{n+1}-R_n| < 1$  m.

For all calculations and graphs presented in this thesis, the values used as input parameters for computer algorithms are shown in Table I, unless specified otherwise. These values are typical of experimental millimeter wave transmission systems. Note that all values in the table are not used in each calculation. For some graphs of the six types of instrumentation presented in this section, it is assumed the propagation path is through a homogeneous medium with

TABLE I

Input Data for Computer Algorithms

<u>Input Parameter</u>	<u>Frequency (GHz)</u>				
	<u>35</u>	<u>94</u>	<u>140</u>	<u>240</u>	
Transmitted Power* ( $P_t$ ):	200	200	50	20	mW
Transmitting Antenna Gain ( $G_t$ ):	47	47	47	47	dB
Receiving Antenna Gain ( $G_r$ ):	47	47	47	47	dB
Total System Loss ( $L_t + L_r$ ):	6	8	9	11	dB
Noise Figure (F):	3	4	7	15	dB
IF Amplifier Bandwidth ( $B_{if}$ ):	10	10	10	10	MHz
Audio Filter Bandwidth ( $B_a$ ):	1	1	1	1	Hz
Number of Pulses Integrated (n):	10000	10000	10000	10000	
Integration Efficiency ( $E_i(n)$ ):	0.03	0.03	0.03	0.03	
Integration Time (T):	1	1	1	1	sec
Pulse Compression Ratio (K):	150:1	150:1	150:1	150:1	
Target Cross Section Area ( $\sigma$ ):					
(1) Transmissometers:	125	125	125	125	m <sup>2</sup>
(2) Radars:	10	10	10	10	m <sup>2</sup>
Probability of Detection ( $P_d$ ):	0.995	0.995	0.995	0.995	
Probability of False Alarm ( $P_{fa}$ ):	10 <sup>-2</sup> , 10 <sup>-4</sup> , 10 <sup>-6</sup> , 10 <sup>-8</sup> , or 10 <sup>-10</sup>				
Specific Attenuation ( $\alpha$ ):	0, 5, 10, or 20				dB/km

\* See Section III.C for exact meaning of  $P_t$  for each system.

specific attenuation of either 0, 5, 10, or 20 dB/km.

For the six types of instrumentation discussed in Section II, we see these system parameters are typical of a system using paraboloid antennas, Impatt diode power sources, and a corner reflector for the calibrated target.

The numerical value for total system losses and noise figure are typical of an experimental system. Since all programs are written in an interactive form, it is possible to easily modify input parameters to represent virtually any kind of transmission system.

#### A. Graphical Results and Discussion.

In this section, graphical results for each of the six transmission systems will be presented and examined. At this point attenuation will be considered as an independent parameter. The effect of rain and fog will be included in Section V.B and V.C.

##### 1. One-way Transmission and Square-Law Detection.

Figures 12 through 16, displayed below, show the typical performance of a system with separated transmitter and receiver. Here, the receiver uses a square-law detector as discussed in Section II.B.1. Figures 12 through 15 show processed signal-to-noise ratio versus range for different values of frequency and specific attenuation. Figure 16 shows the variation in range as a function of specific attenuation,  $\alpha$ . Because this transmission system is over a one-way propagation path, no target is involved. Therefore, rather than specifying probability of detection and probability of false alarm as in a radar system, calculations of range as a function of specific attenuation are presented for a predetermined processed signal-to-noise ratio of 10 dB.

From the curves displaying signal-to-noise ratio as a function of range, it can be observed that range decreases significantly as the frequency is increased. Also, notice as specific attenuation increases, the signal-to-noise ratio  $E/N$  at the system output not only decreases, but its rate of decrease with respect to range is significantly increased.

In Figure 16, we see the effects of specific attenuation and frequency on range performance. As expected, when frequency is increased range performance will deteriorate. Also, as specific attenuation increases the range is seen to be greatly reduced. Even under the worst possible weather conditions, a range of between three and four kilometers can be achieved from the two-ended system. All graphs presented in this section are derived from computer program SLDET2E shown in Appendix C.

In these graphs, the systems are compared on the basis of equal specific attenuation at all frequencies. A more basic comparison is on the basis of identical meteorological conditions. This is deferred to the next two sections, B and C.

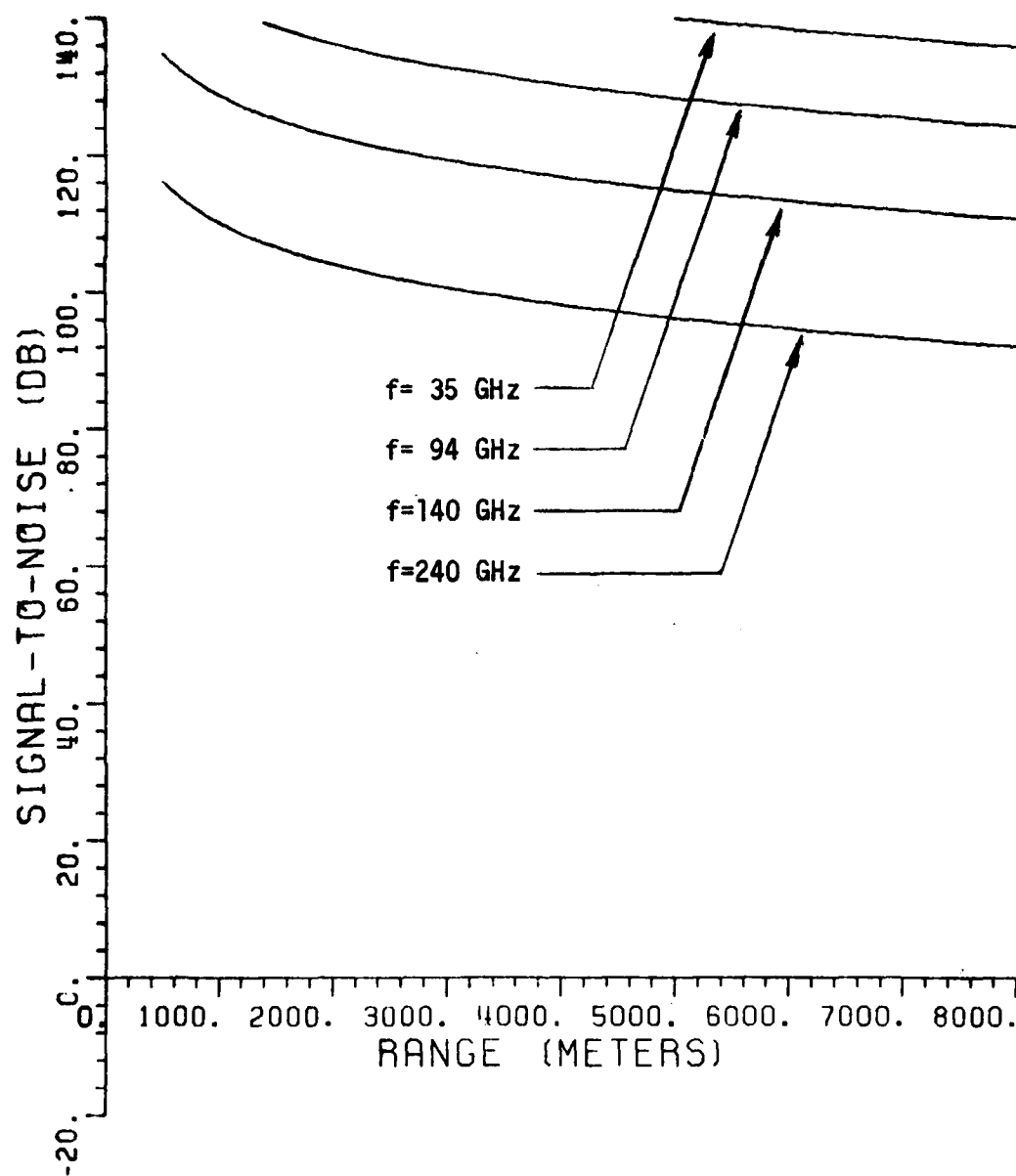


Figure 12. Signal-to-noise ratio versus Range for the double-ended system with square-law detection.  $\alpha = 0$  dB/km. For unspecified system parameters, see Table I, p. 53.



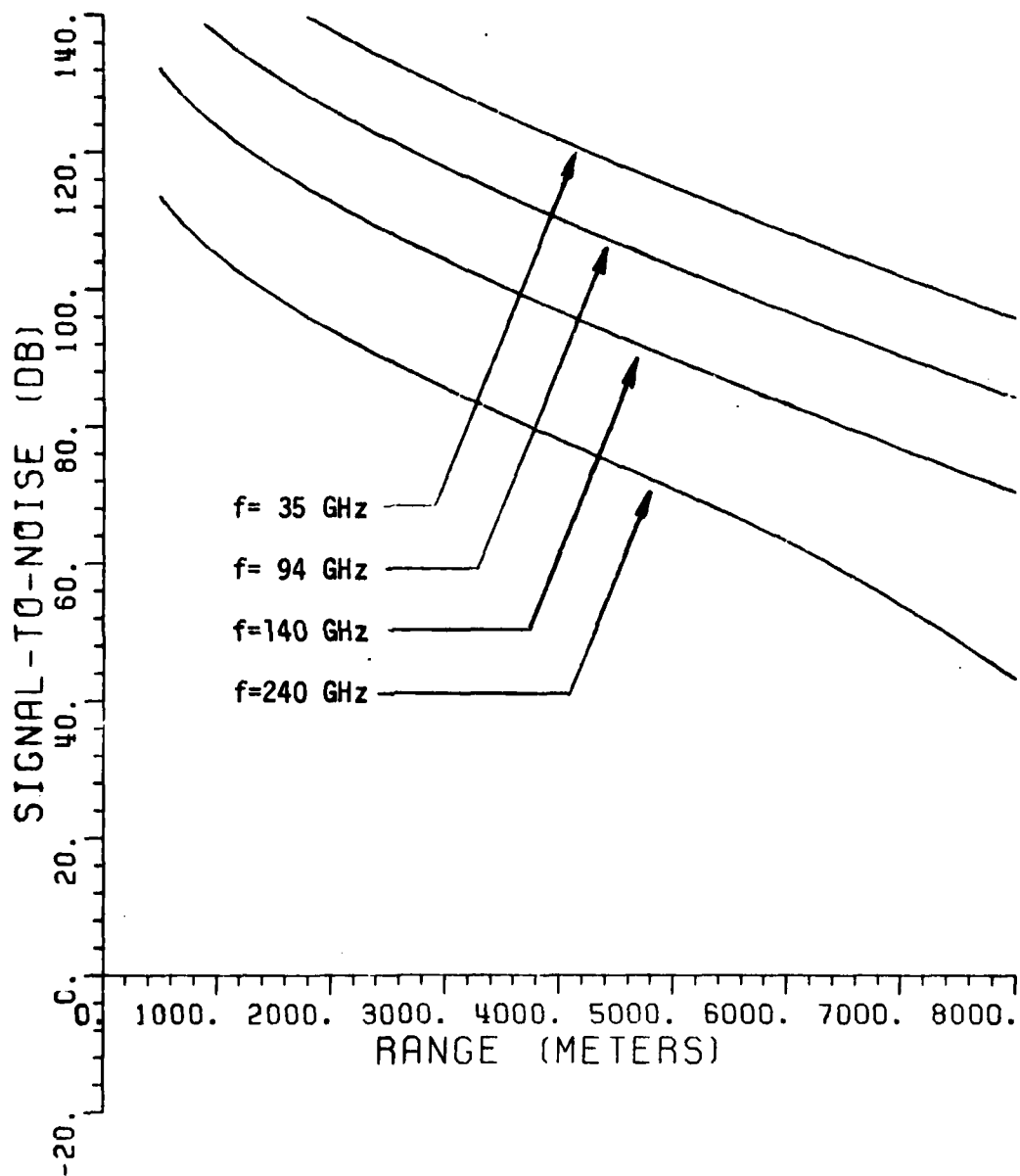


Figure 13. Signal-to-noise ratio versus Range for the double-ended system with square-law detection.  $\alpha = 5$  dB/km. For unspecified system parameters, see Table I, p. 53.

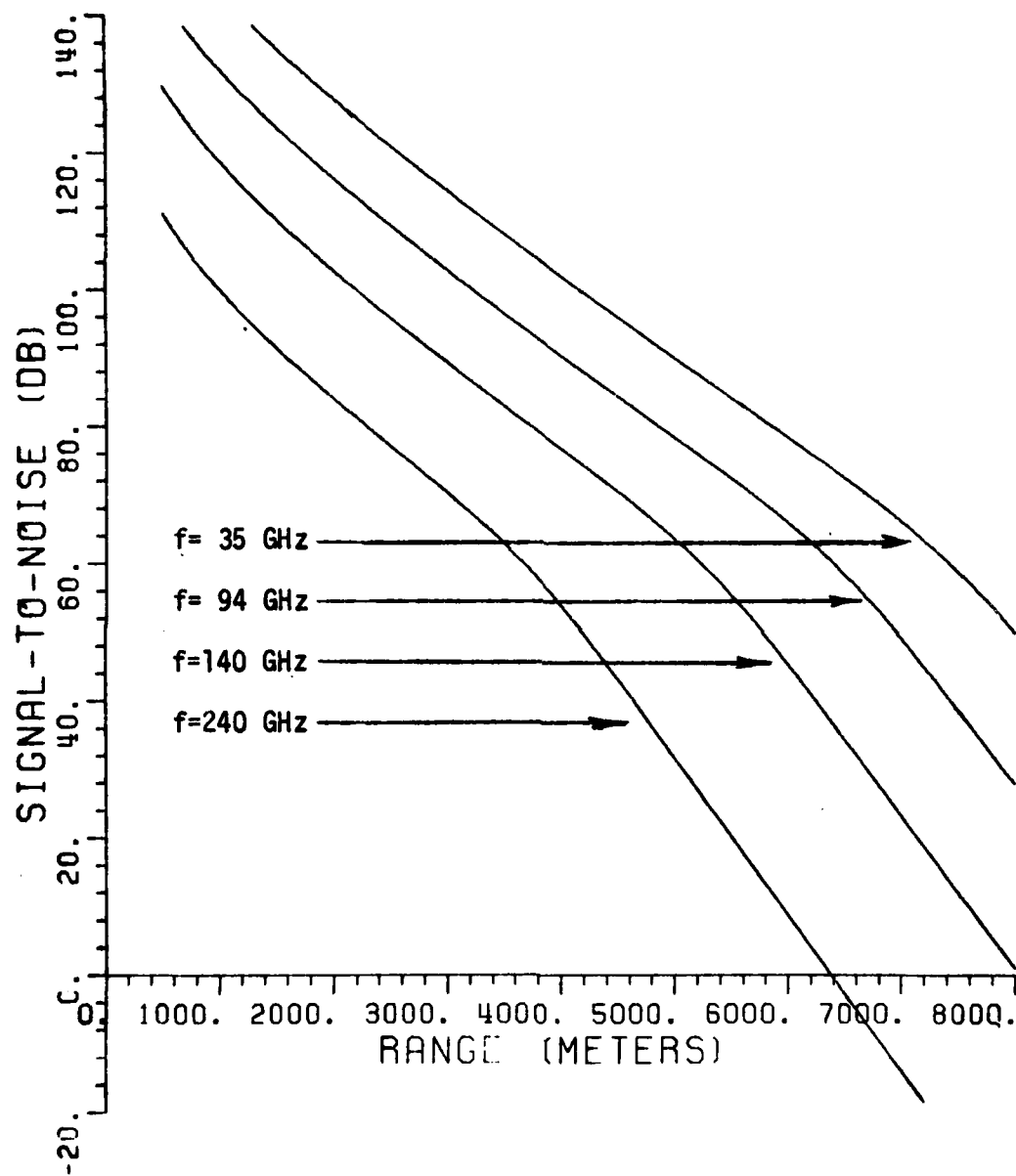


Figure 14. Signal-to-noise ratio versus Range for the double-ended system with square-law detection.  $\alpha = 10$  dB/km. For unspecified system parameters, see Table I, p. 53.

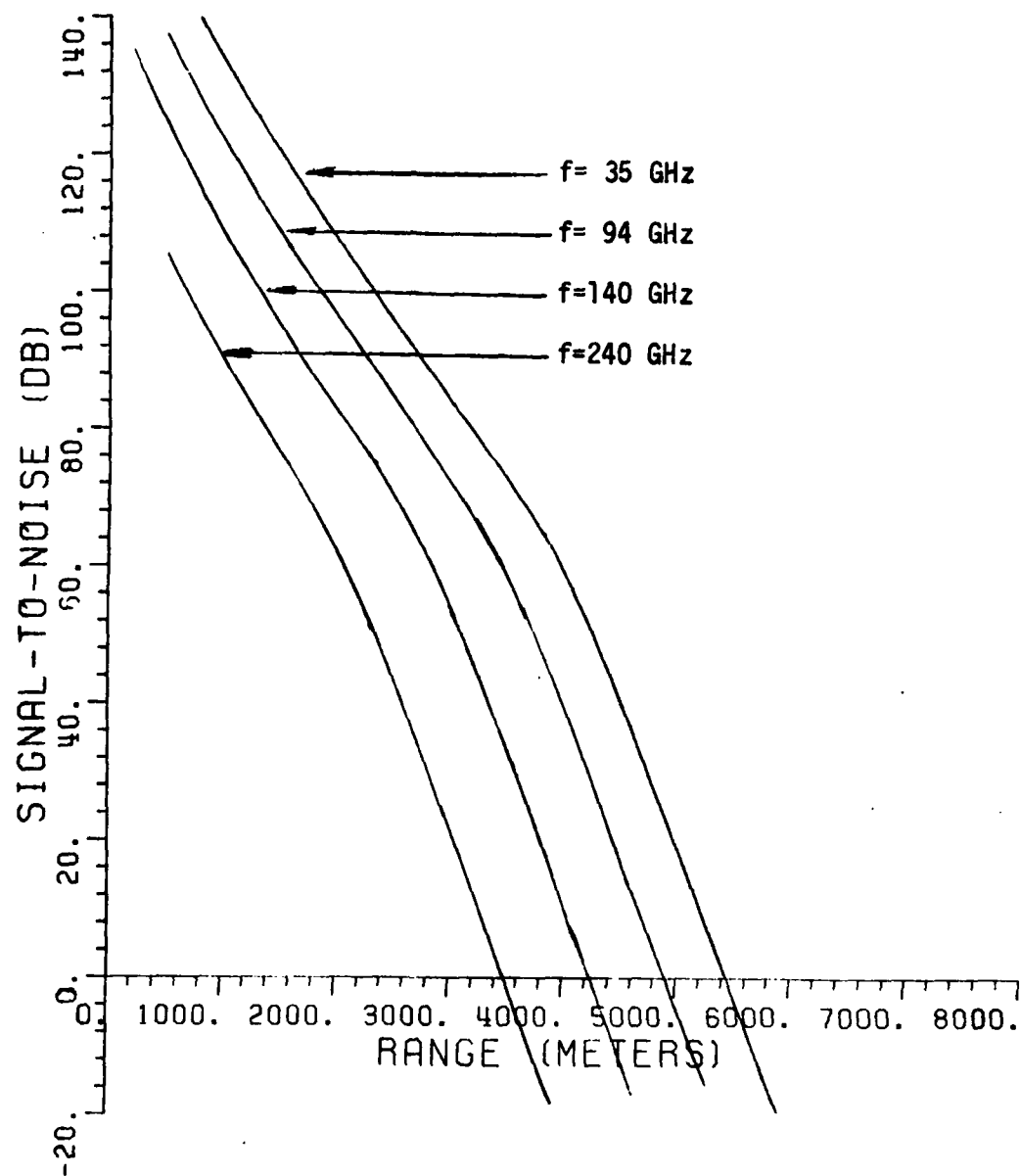


Figure 15. Signal-to-noise ratio versus Range for the double-ended system with square-law detection.  $\alpha = 20$  dB/km. For unspecified system parameters, see Table I, p. 53.

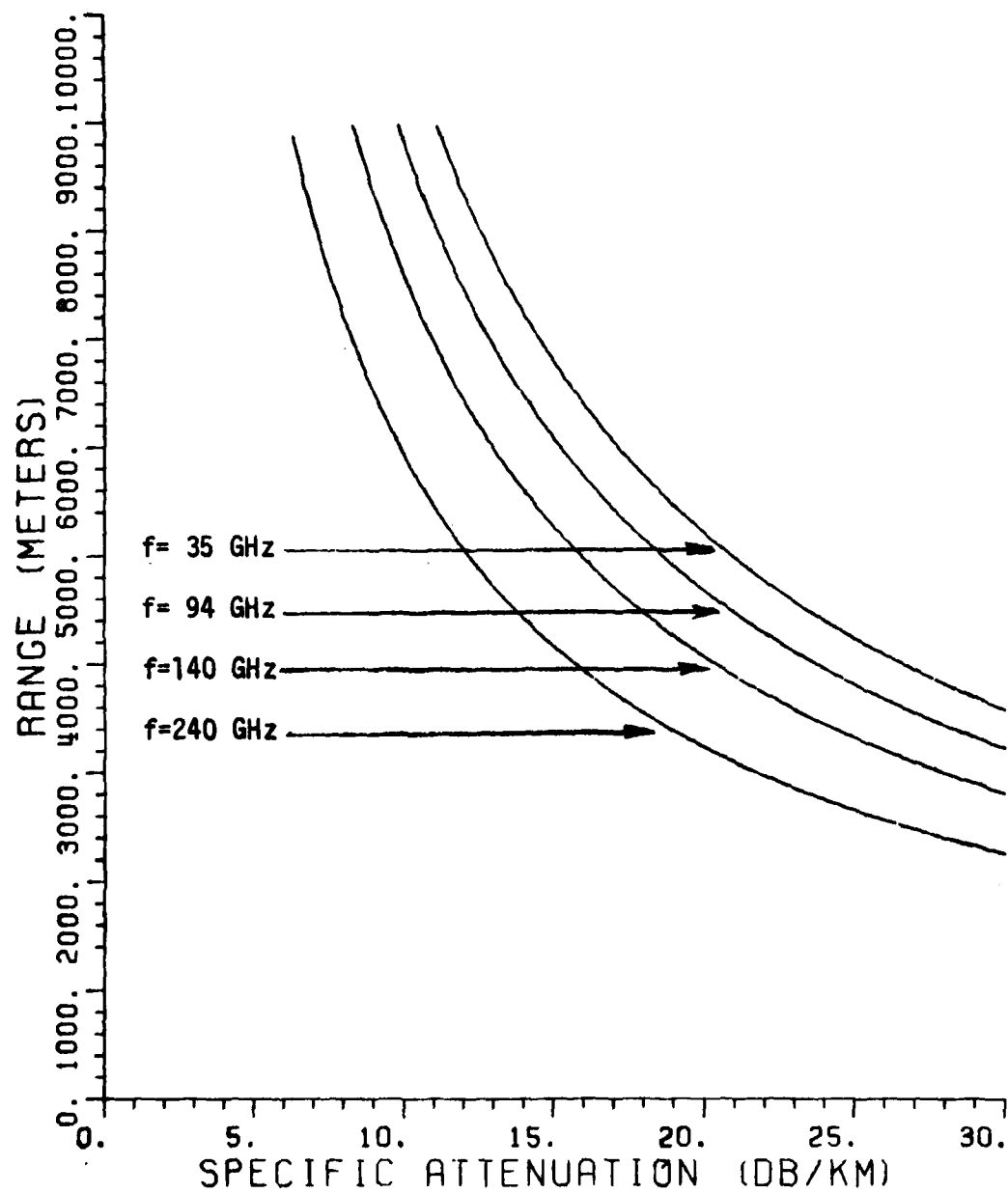


Figure 16. Range versus Specific Attenuation for the double-ended system with square-law detection.  $E/N = 10$  dB. For unspecified system parameters, see Table I, p. 53.

## 2. Two-way Transmission and Square-Law Detection.

Figures 17 through 23, presented below, show typical performance of a single-ended system with the receiver identical to the previous system. Again, the receiver uses a square-law detector as discussed in Section II. B.2. Specific attenuation is treated as an independent parameter. The specific effect of rain and fog is treated in Sections B and C.

Figures 17 through 20 show the signal-to-noise ratio versus range for various values of frequency and specific attenuation. Upon comparison of Figures 17 through 20 with Figures 12 through 15 of the previous system, we can observe this single-ended system is more sensitive to effects of specific attenuation. This is true because doubling the effective length by placing transmitting and receiving antennas near each other causes transmitted signal to be attenuated twice as much as for the double-ended system.

Figures 21 and 22 show the probability of detecting a target both as a function of processed signal-to-noise ratio and range. For both graphs, we are assuming predetermined false alarm probabilities of  $10^{-2}$ ,  $10^{-4}$ ,  $10^{-6}$ ,  $10^{-8}$ , and  $10^{-10}$ ; Figure 22 for a transmitted frequency of 94 GHz. From Figure 21, note the processed signal-to-noise ratio must have a value of at least 18 dB for almost certain detection of the 125 m<sup>2</sup> target. Under the assumptions of Table I, this requires the target to be no more than about 1300 meters from the transmitting and receiving antennas for 94 GHz.

Finally, Figure 23 shows the effects of specific attenuation and

frequency on radar range performance. For a 0.995 probability of detecting the target and  $10^{-6}$  probability of false alarm, the computed processed signal-to-noise ratio at the output of the detector is 15.83 dB.

As in the case of the double-ended system discussed in the last section, performance will decrease as frequency and specific attenuation is increased. All graphs in this section are derived from the computer program SLDET shown in Volume II.

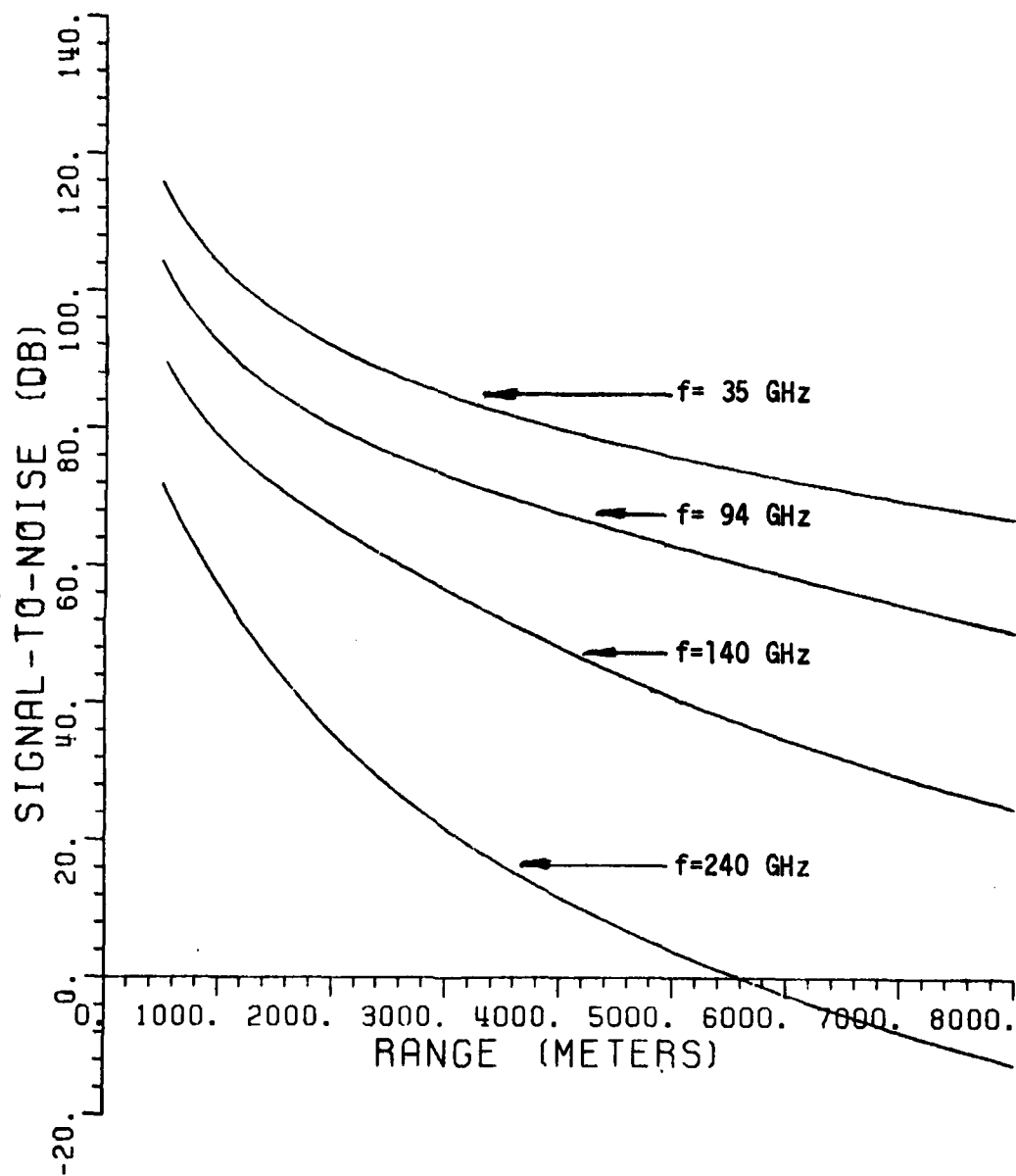


Figure 17. Signal-to-noise ratio versus Range for the single-ended system with square-wave modulation and square-law detection.  $\alpha = 0$  dB/km,  $\sigma = 125$  m<sup>2</sup>. For unspecified system parameters, see Table I, p. 53.

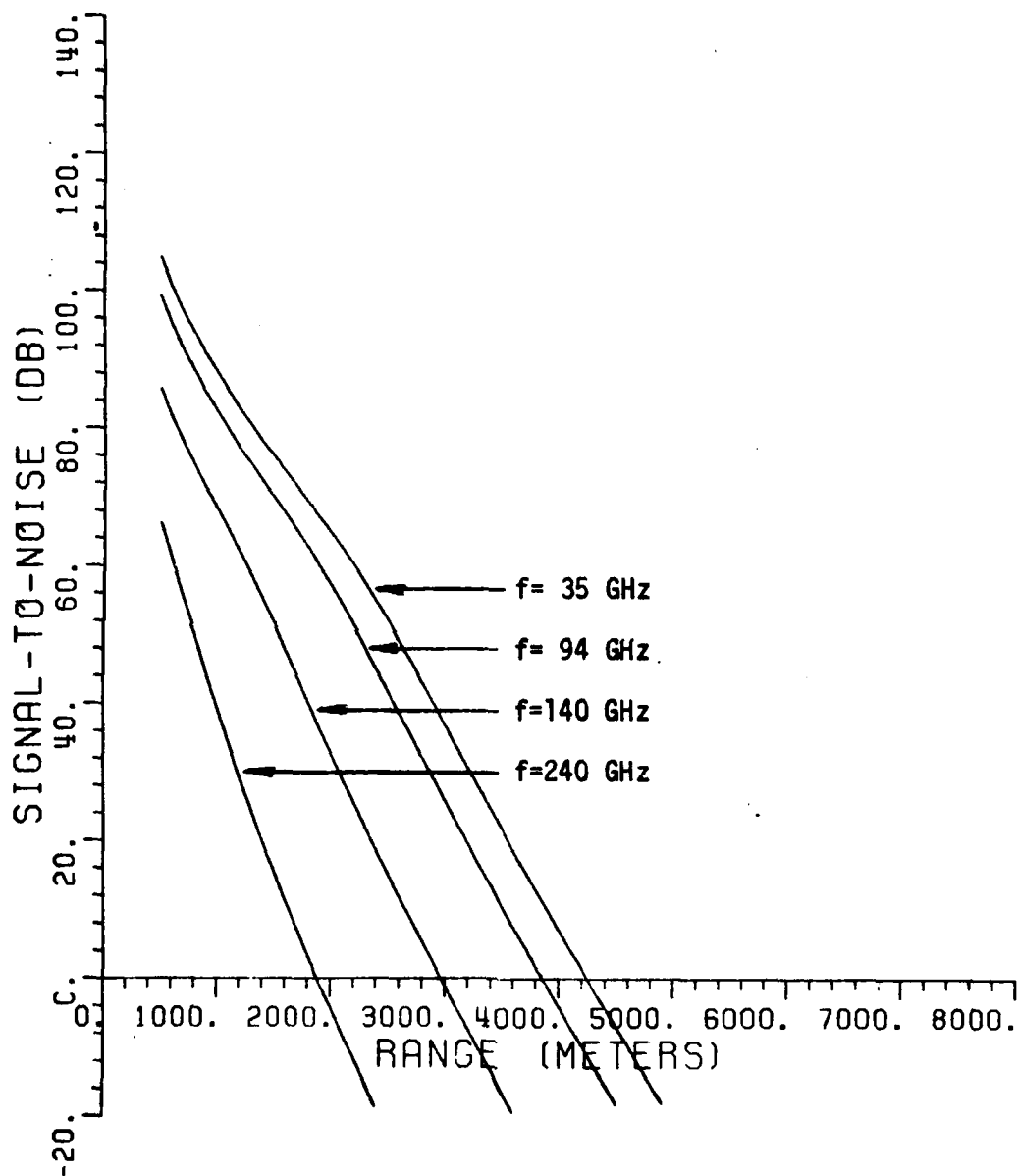


Figure 18. Signal-to-noise ratio versus Range for the single-ended system with square-wave modulation and square-law detection.  $\alpha \approx 5$  dB/km,  $\sigma = 125$  m<sup>2</sup>. For unspecified system parameters, see Table I, p. 53.



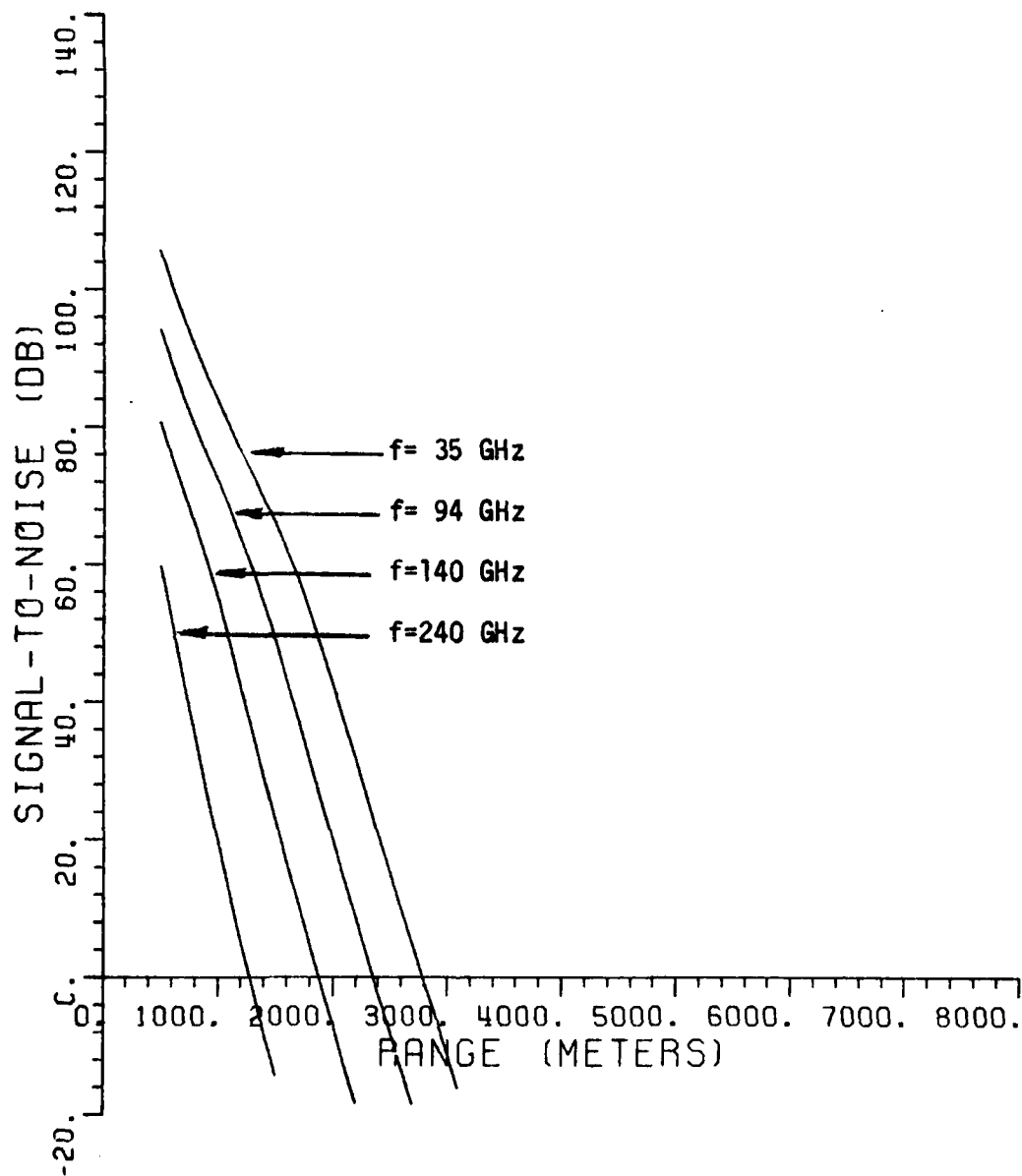


Figure 19. Signal-to-noise ratio versus Range for the single-ended system with square-wave modulation and square-law detection.  $\alpha = 10$  dB/km,  $\sigma = 125$  m<sup>2</sup>.  
For unspecified system parameters, see Table I, p. 53.

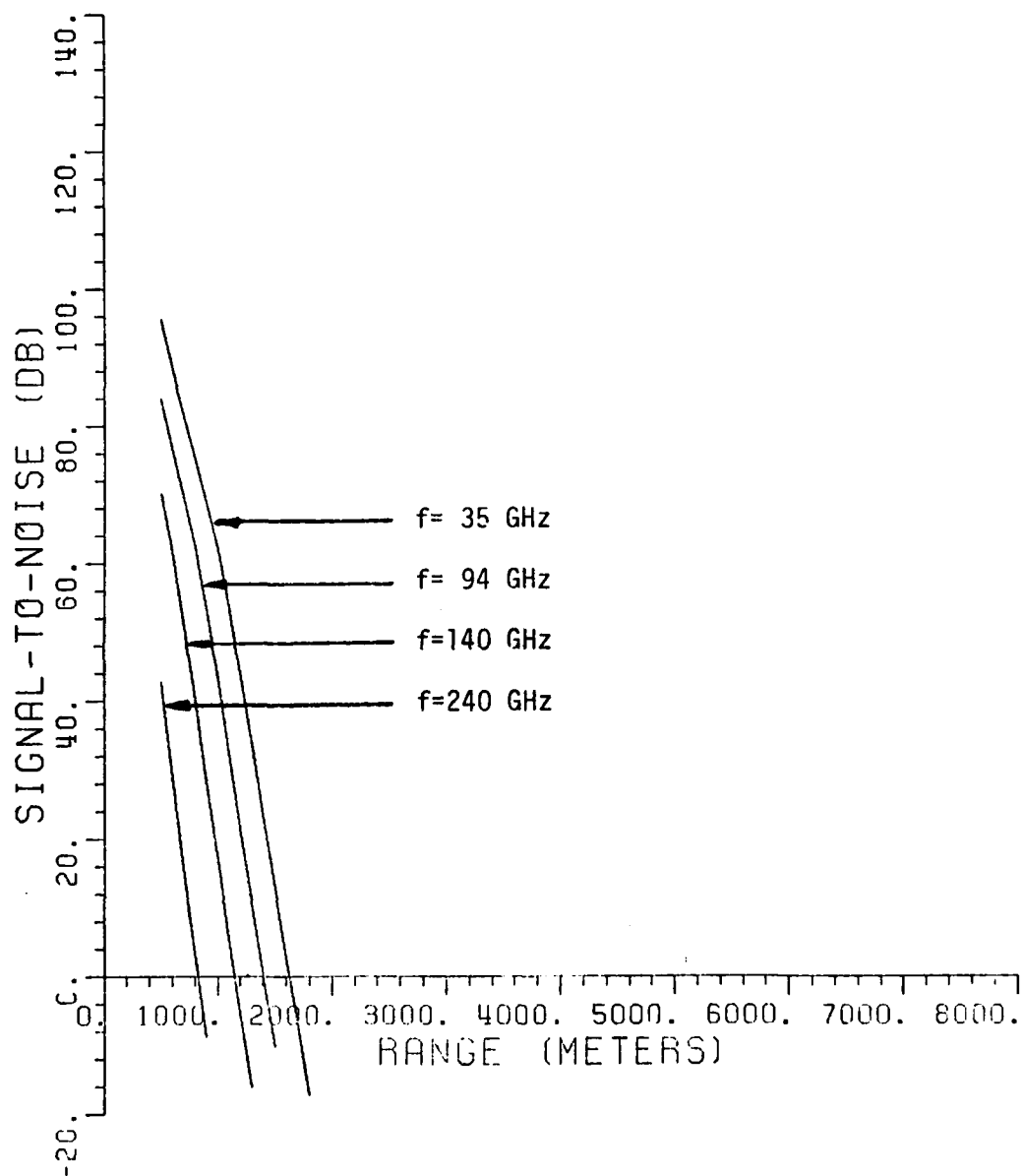


Figure 20. Signal-to-noise ratio versus Range for the single-ended system with square-wave modulation and square-law detection.  $\alpha = 20$  dB/km,  $\sigma = 125$  m<sup>2</sup>.

For unspecified system parameters, see Table I, p. 53.

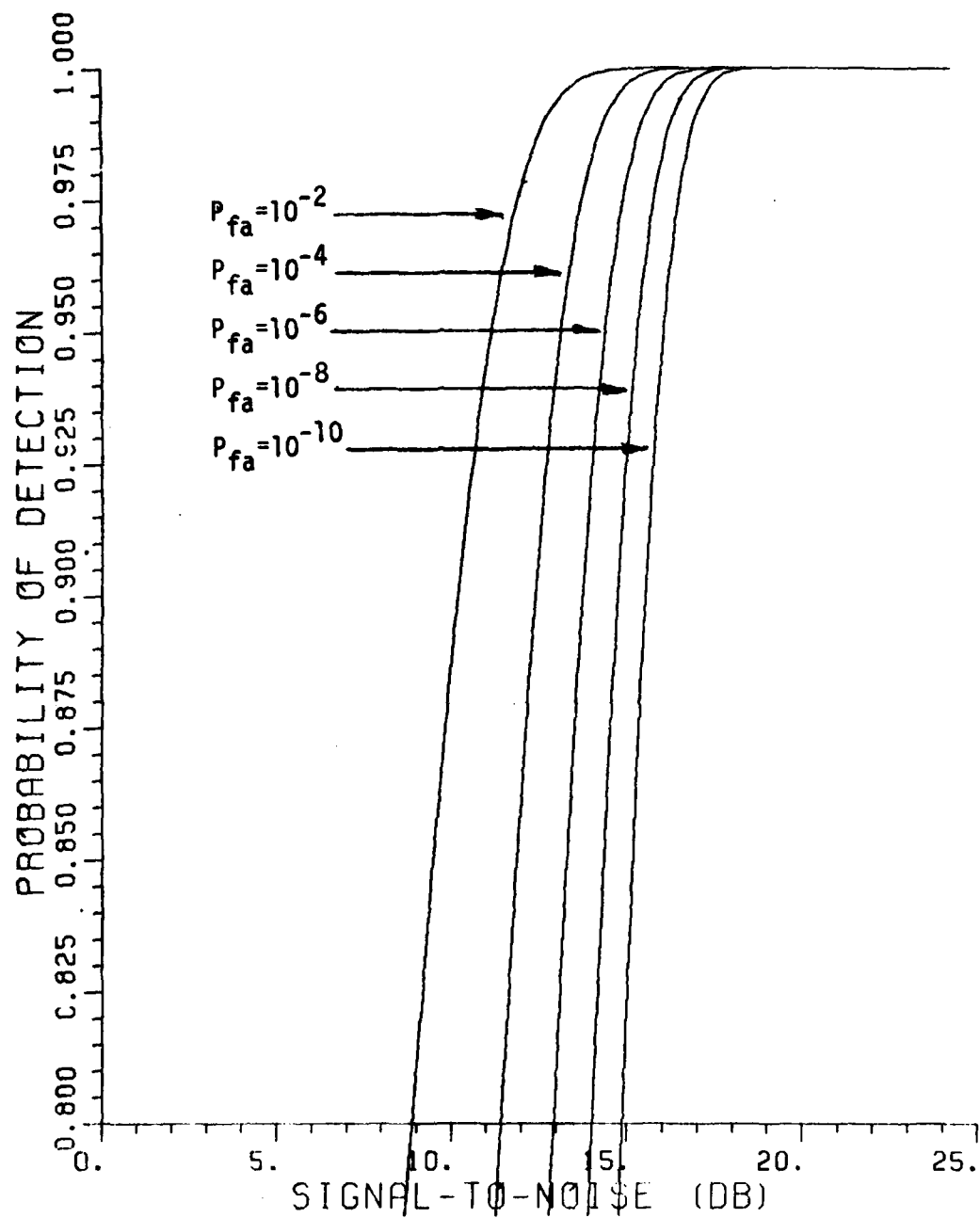


Figure 21. Probability of Detection versus Post-detection Signal-to-noise ratio for the single-ended system with square-wave modulation and square-law detection.

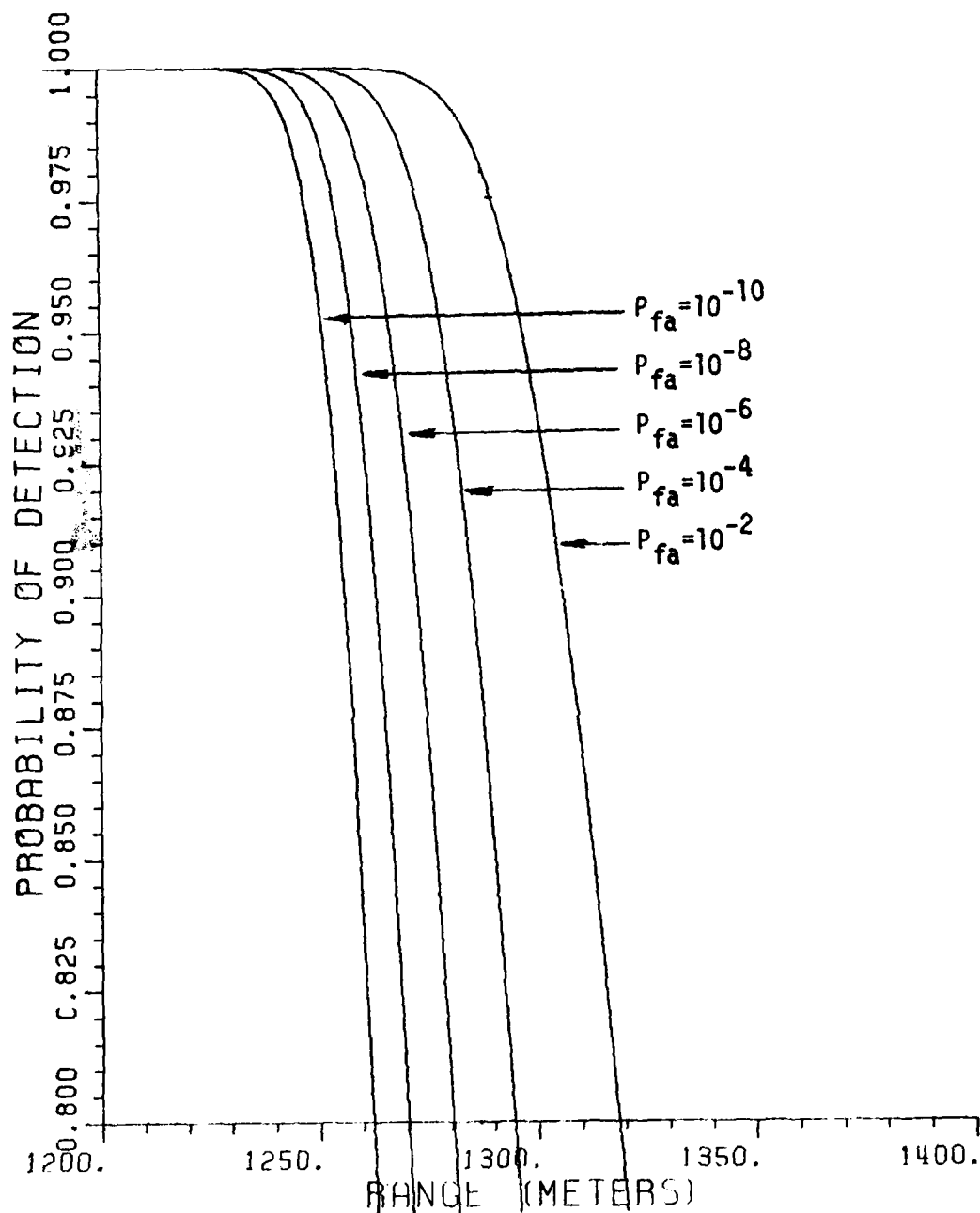


Figure 22. Probability of Detection versus Range for the single-ended system with square-wave modulation and square-law detection.  $f = 94$  GHz,  $\alpha = 20$  dB/km,  $\sigma = 125$  m<sup>2</sup>. For unspecified system parameters, see Table I, p. 53.

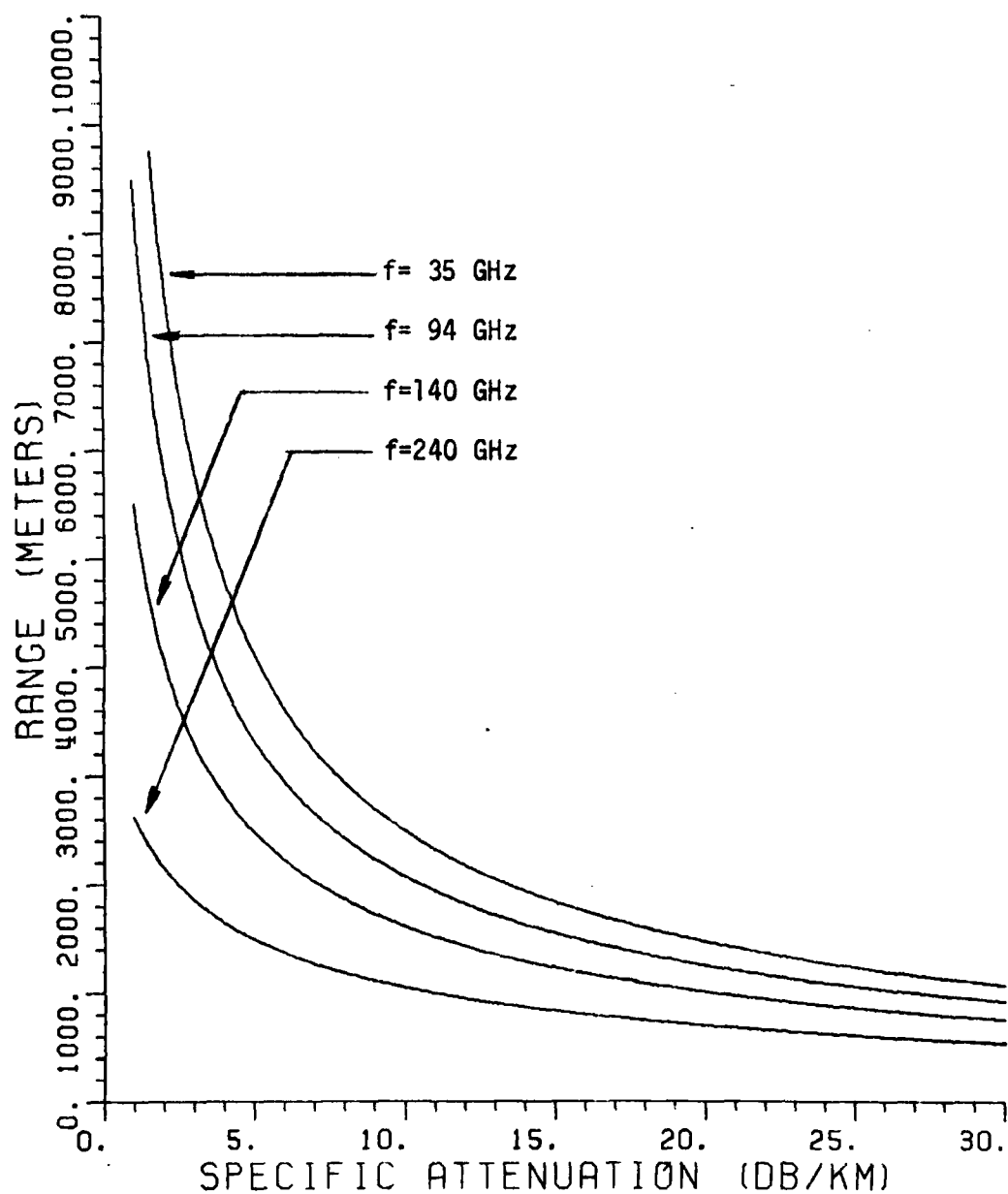


Figure 23. Range versus Specific Attenuation for the single-ended system with square-wave modulation and square-law detection.  $P_d = 0.995$ ,  $P_{fa} = 10^{-6}$  (Computed processed  $E/N = 15.83$  dB.)

For unspecified system parameters, see Table I, p. 53.

### 3. CW Signal Transmission and Quadrature Receiver.

Figures 24 through 30 show typical performance of a radar system which transmits a CW signal toward a target with the transmitting and receiving antennas in close proximity. However, as shown in Section II.B.3, we use a quadrature receiver rather than a square-law device as in the previous systems.

Figures 24 through 27 show the signal-to-noise ratio versus range for various values of frequency and specific attenuation. From these graphs, even with 20 dB/km attenuation at 94 GHz, a range between 1 and 2 kilometers is expected. This is a significant improvement over the two-way transmissometer system using square-law detection.

Figures 28 and 29 show the probability of detecting a 125 m<sup>2</sup> target both as a function of processed signal-to-noise ratio and range. For both graphs, we are assuming false alarm probabilities of 10<sup>-2</sup>, 10<sup>-4</sup>, 10<sup>-6</sup>, 10<sup>-8</sup>, and 10<sup>-10</sup>; Figure 29 assumes a transmitted frequency of 94 GHz. As with the previous system, to be certain of detecting the target a signal-to-noise ratio of about 18 dB is required. A signal-to-noise ratio of about 18 dB would necessitate the target to be no more than about 1700 meters from transmitting and receiving antennas for a near certain probability of detection.

Finally, Figure 30 shows effects of specific attenuation and frequency on radar range performance. For a 0.995 probability of detection and 10<sup>-6</sup> probability of false alarm, the computed processed signal-to-noise ratio at the output of the detector is 15.83 dB. All graphs presented in this section are derived from the computer algorithm CODET1 presented in Volume II.

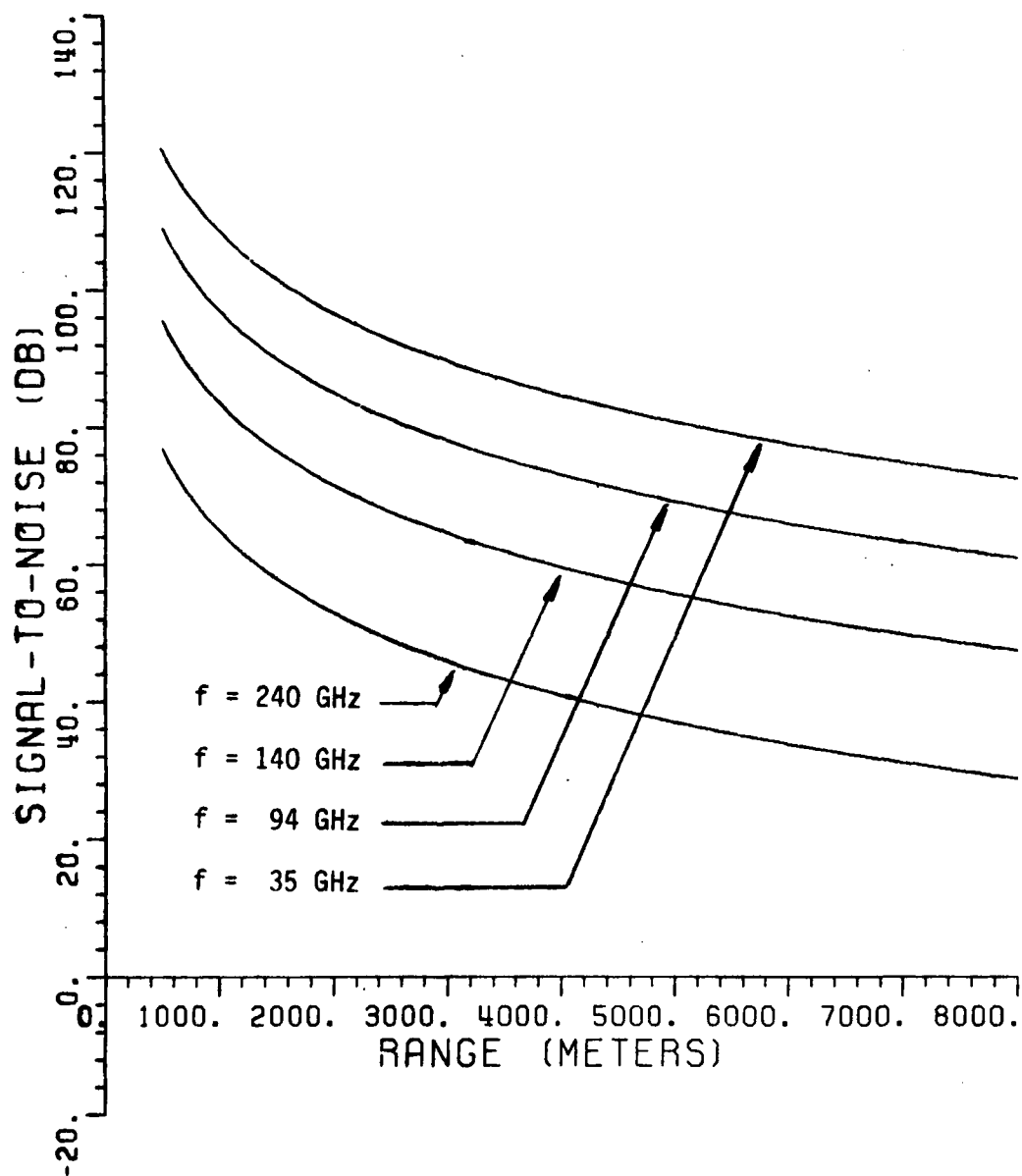


Figure 24. Signal-to-noise ratio versus Range for the single-ended CW system with quadrature receiver.  $\alpha = 0$  dB/km,  $\sigma = 125$  m<sup>2</sup>.

For unspecified system parameters, see Table I, p. 53.

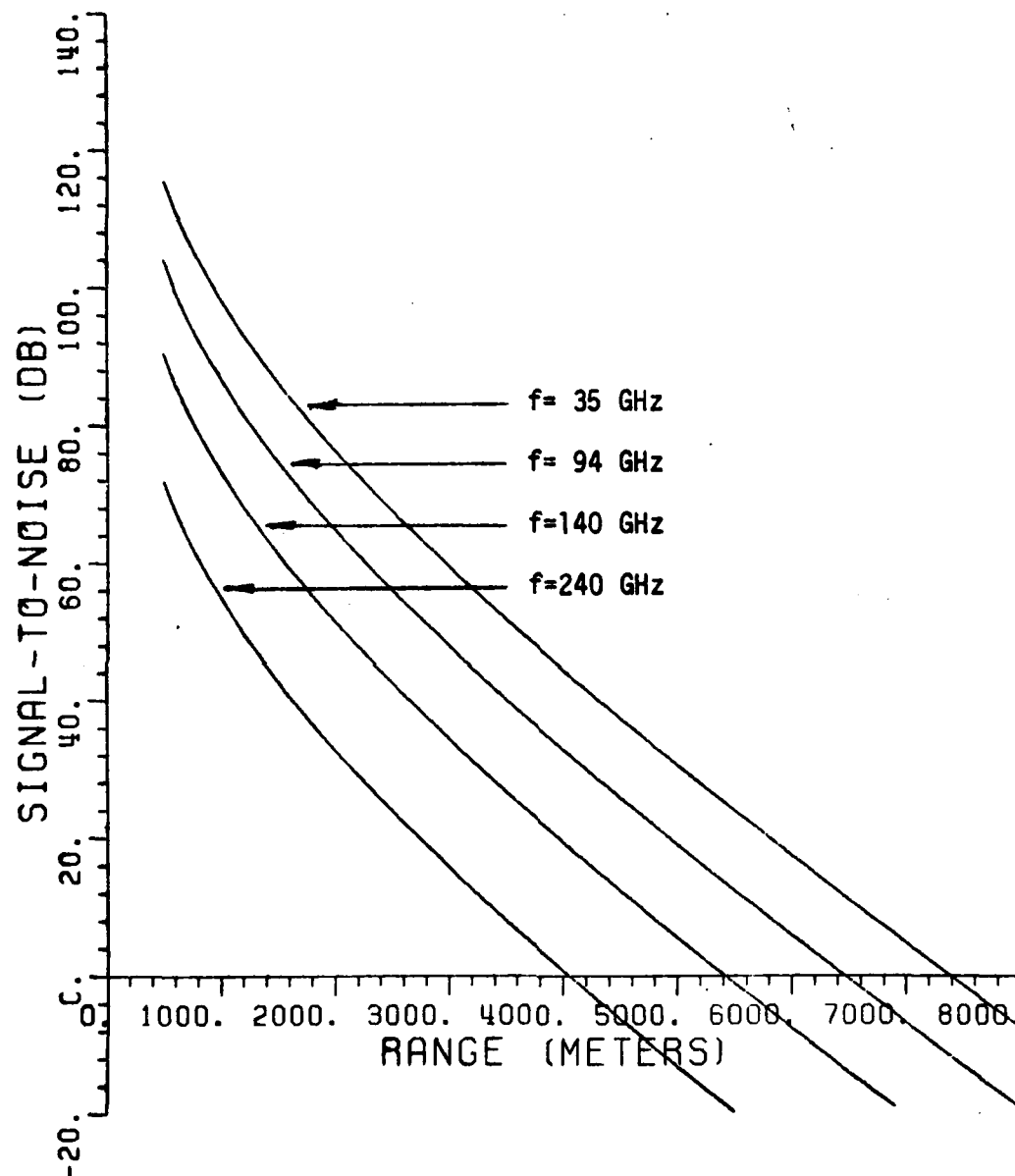


Figure 25. Signal-to-noise ratio versus Range for the single-ended CW system with quadrature receiver.  $\alpha = 5$  dB/km,  $\sigma = 125$  m<sup>2</sup>.

For unspecified system parameters, see Table I, p. 53.



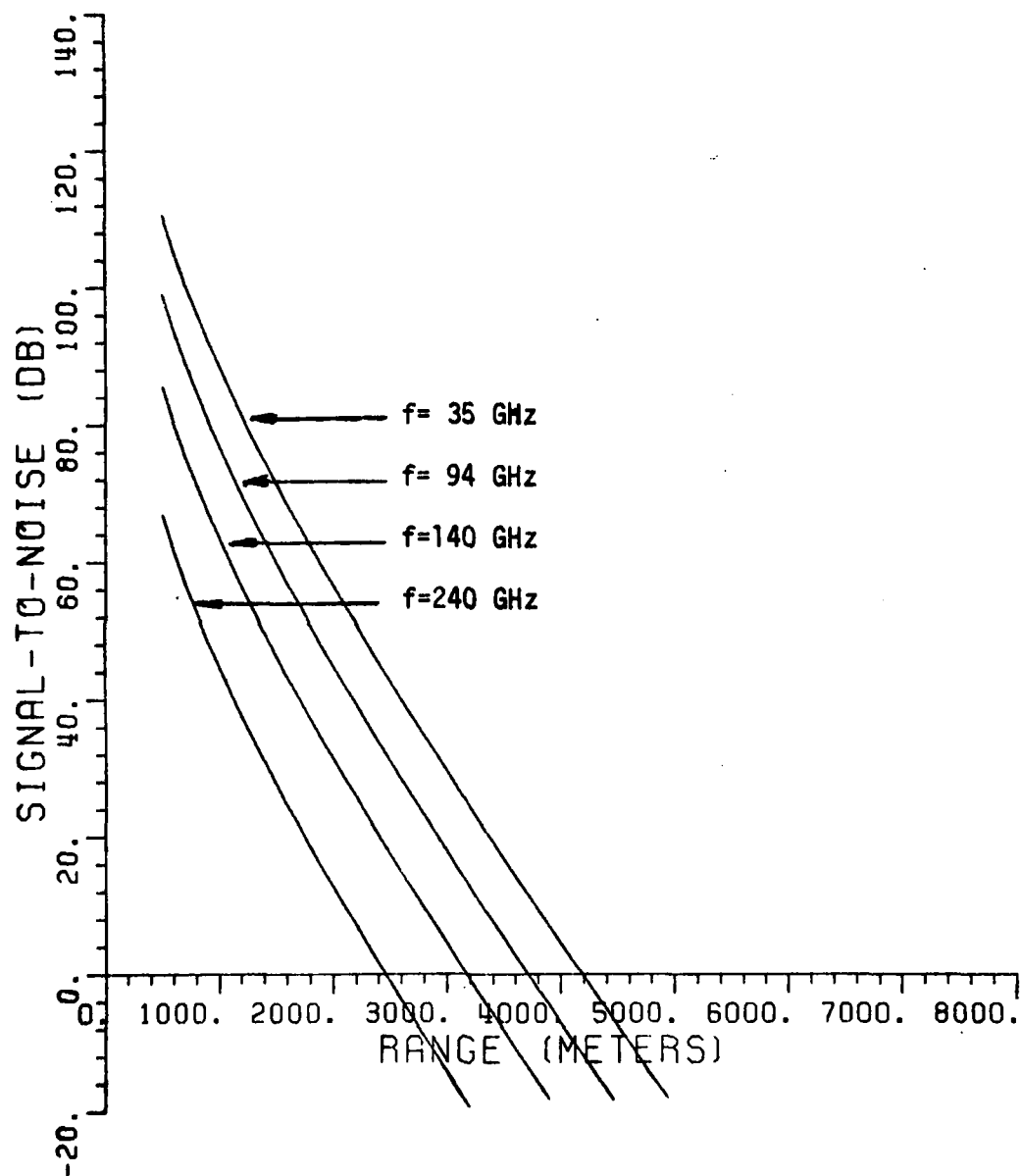


Figure 26. Signal-to-noise ratio versus Range for the single-ended CW system with quadrature receiver.  $\alpha = 10$  dB/km,  $\sigma = 125$  m<sup>2</sup>.

For unspecified system parameters, see Table I, p. 53.

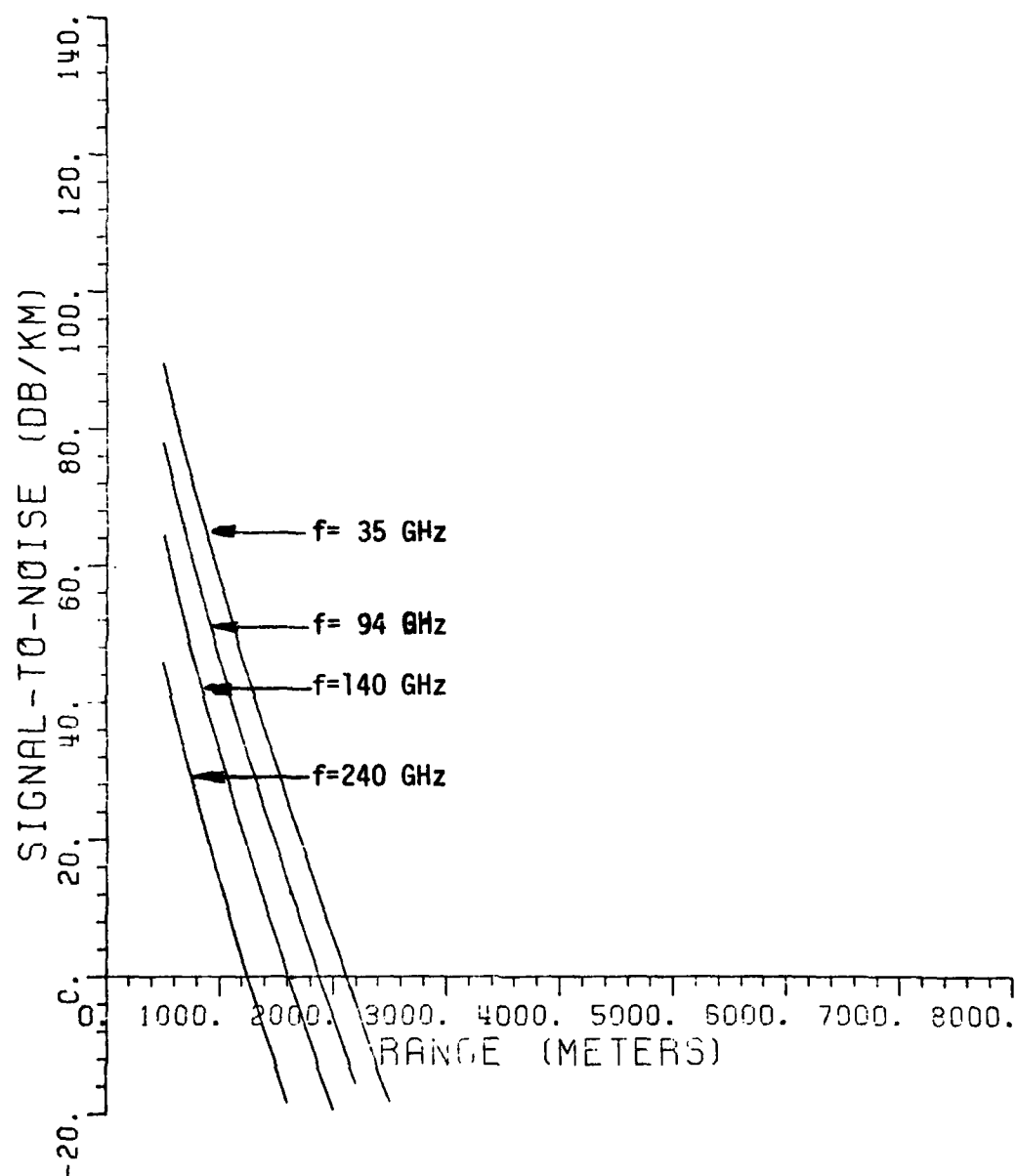


Figure 27. Signal-to-noise ratio versus Range for the single-ended CW system with quadrature receiver.  $\alpha = 20$  dB/km,  $\sigma = 125$  m<sup>2</sup>.

For unspecified system parameters, see Table I, p. 53.

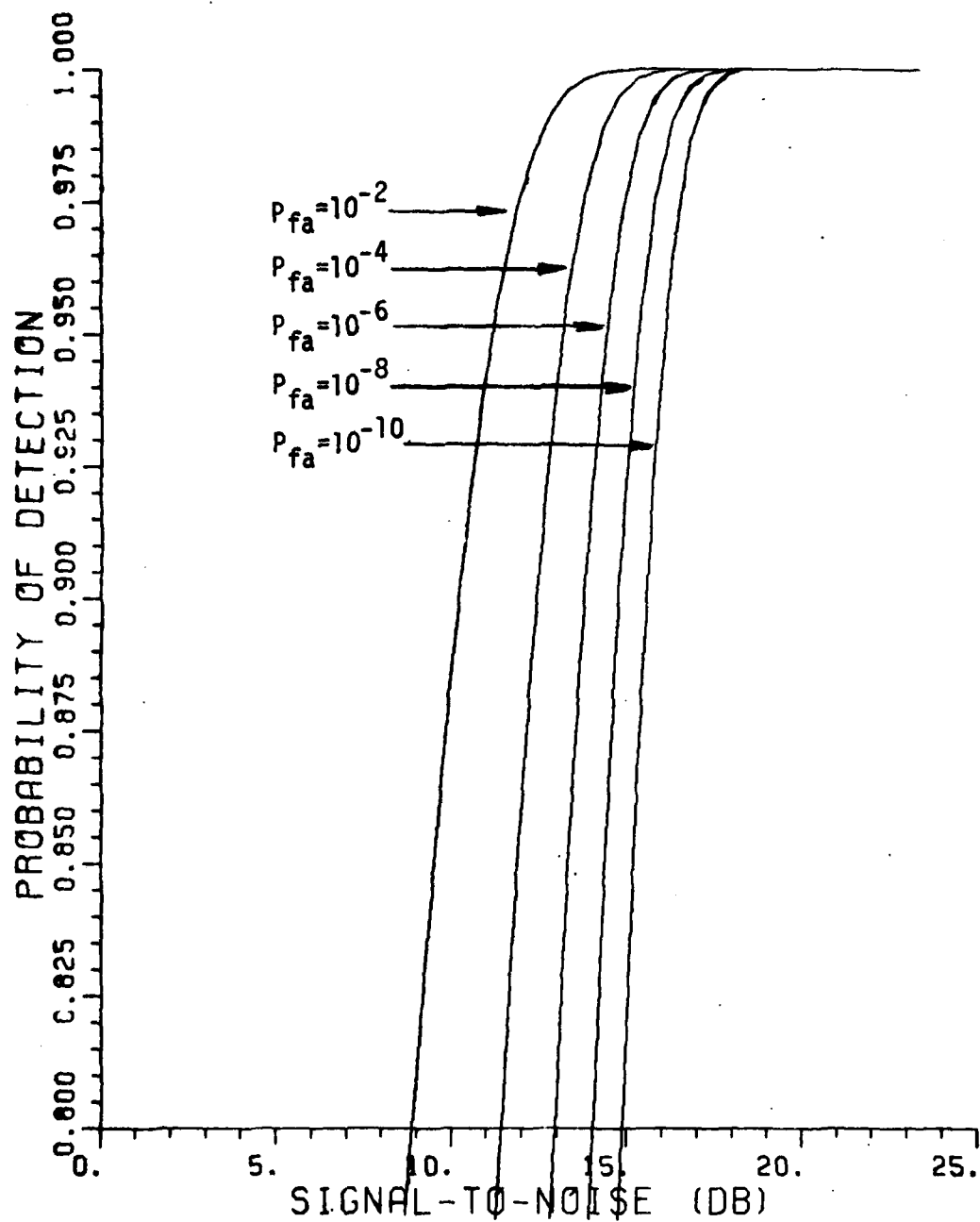


Figure 28. Probability of Detection versus Post-detection Signal-to-noise ratio for a single-ended CW system with quadrature receiver.

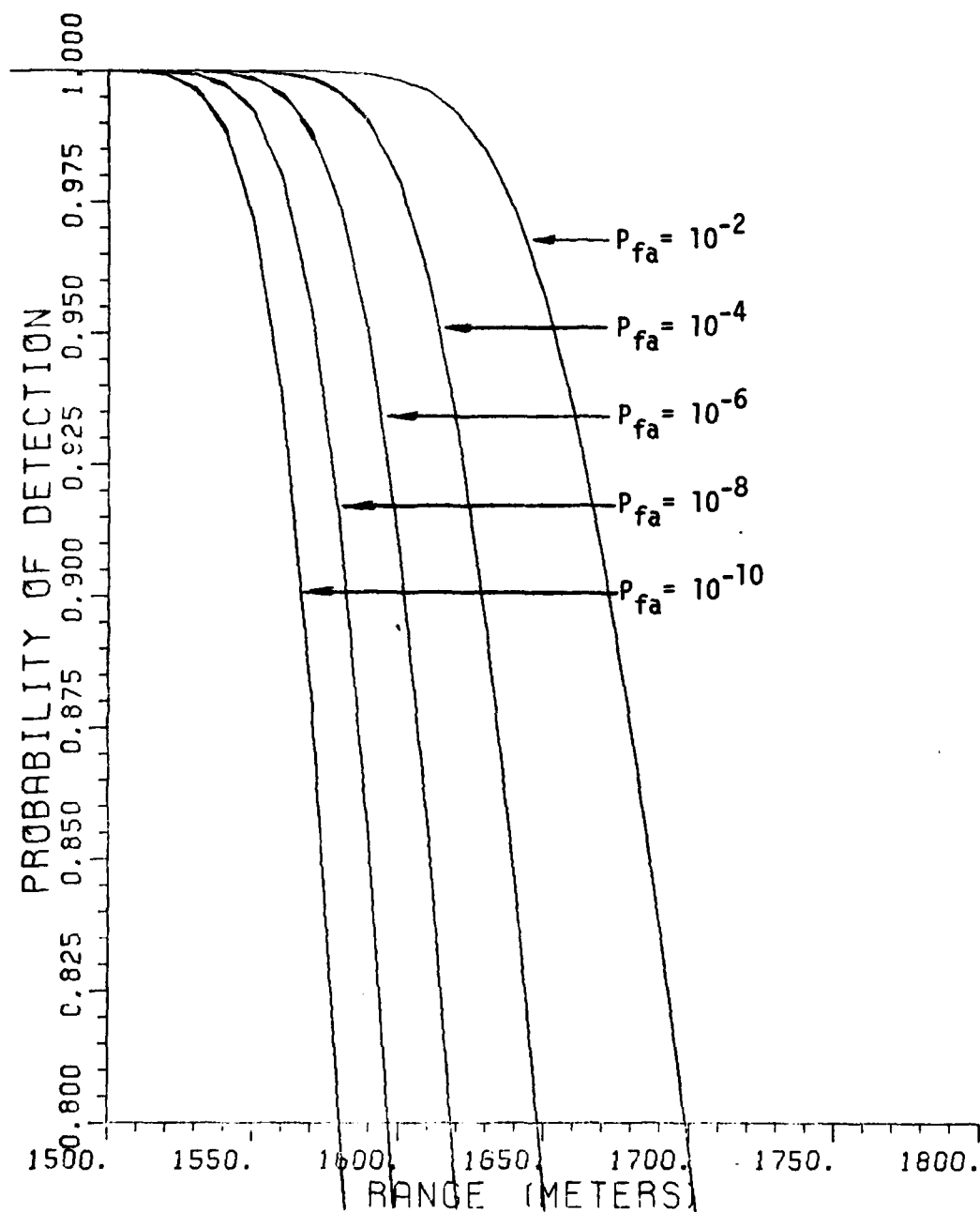


Figure 29. Probability of Detection versus Range for the single-ended CW system with quadrature receiver.  $f = 94$  GHz,  $\alpha = 20$  dB/km, and  $\sigma = 125$  m<sup>2</sup>.  
For unspecified system parameters, see Table I, p. 53.

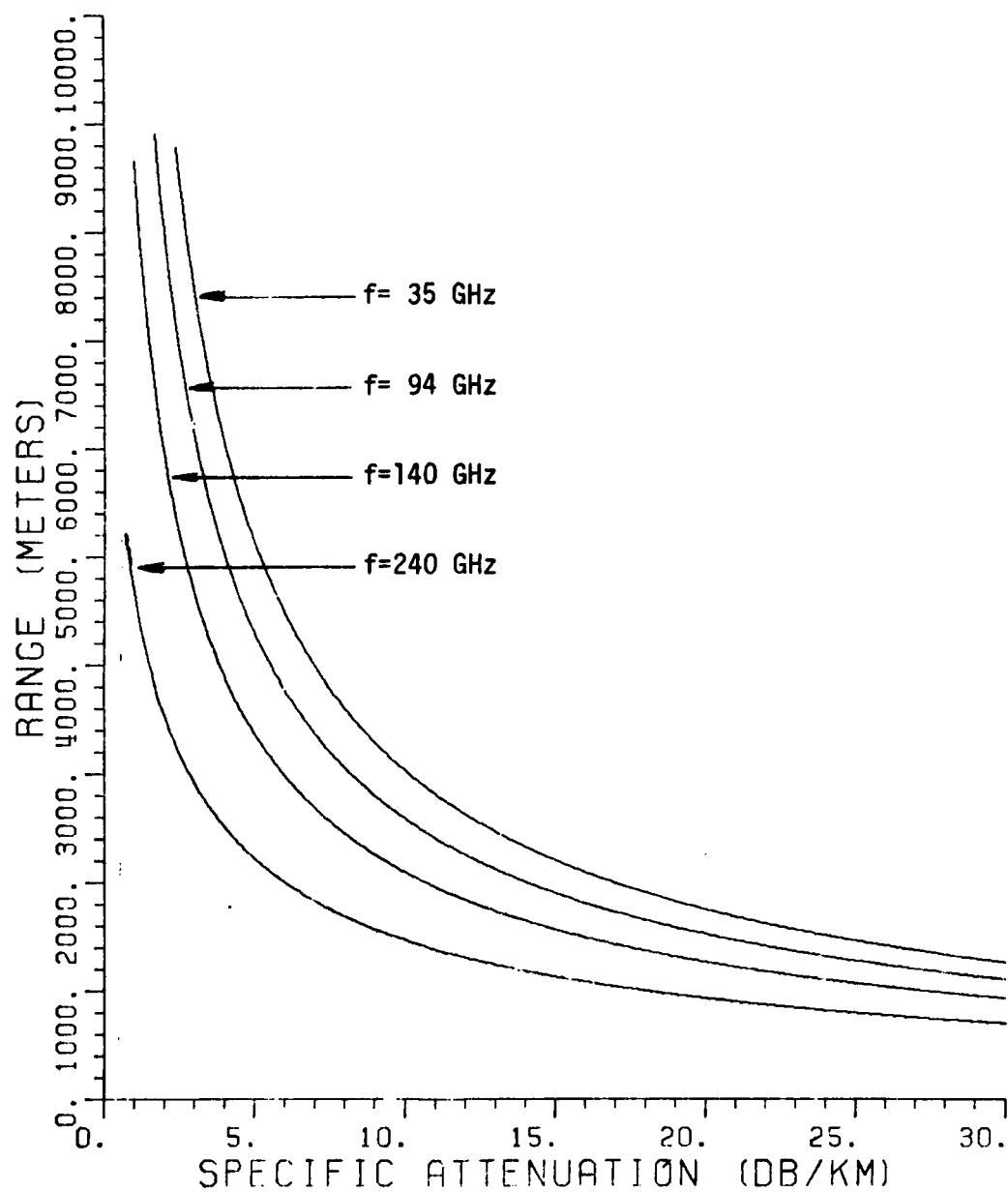


Figure 30. Range versus Specific Attenuation for the single-ended CW system with quadrature receiver.  $P_d = 0.995$ ,  $P_{fa} = 10^{-6}$  (Computed processed E/N = 17.79 dB.)

For unspecified system parameters, see Table I, p. 53.

#### 4. Pulsed Source with Incoherent Pulse Integration.

As discussed in Section II.B.4, this system can represent either a pulsed source range gated radar or a transmissometer detecting the reflection from a calibrated target such as a corner reflector. Typical performance of this radar system is shown in Figures 31 through 37 below.

Figures 31 through 34 display the signal-to-noise ratio versus range for various values of frequency and specific attenuation. In all cases, 10,000 pulses are integrated with an integration efficiency of 3%. Since these graphs are for a pulsed source range gated radar, a target cross section area of  $125 \text{ m}^2$  is used. Upon comparison of Figures 37 through 41 with corresponding figures for the previous transmission systems, we see this system to have shorter range as specific attenuation is increased. However, under the 20 dB/km propagation conditions, minimum ranges of between 800 and 1800 meters can be expected.

Figures 35 and 36 show the probability of detecting a  $125 \text{ m}^2$  target as a function of processed signal-to-noise ratio and radar range. For both graphs, we are again using prescribed false alarm probabilities of  $10^{-2}$ ,  $10^{-4}$ ,  $10^{-6}$ ,  $10^{-8}$ , and  $10^{-10}$ ; in Figure 36 a 94 GHz transmitted frequency is assumed. As in the cases discussed before, it is necessary to have a processed signal-to-noise ratio of at least 18 dB for a near certain probability of detecting the calibrated target. This requires the target to be no more than about 1000 meters from the transmitting and receiving antennas.

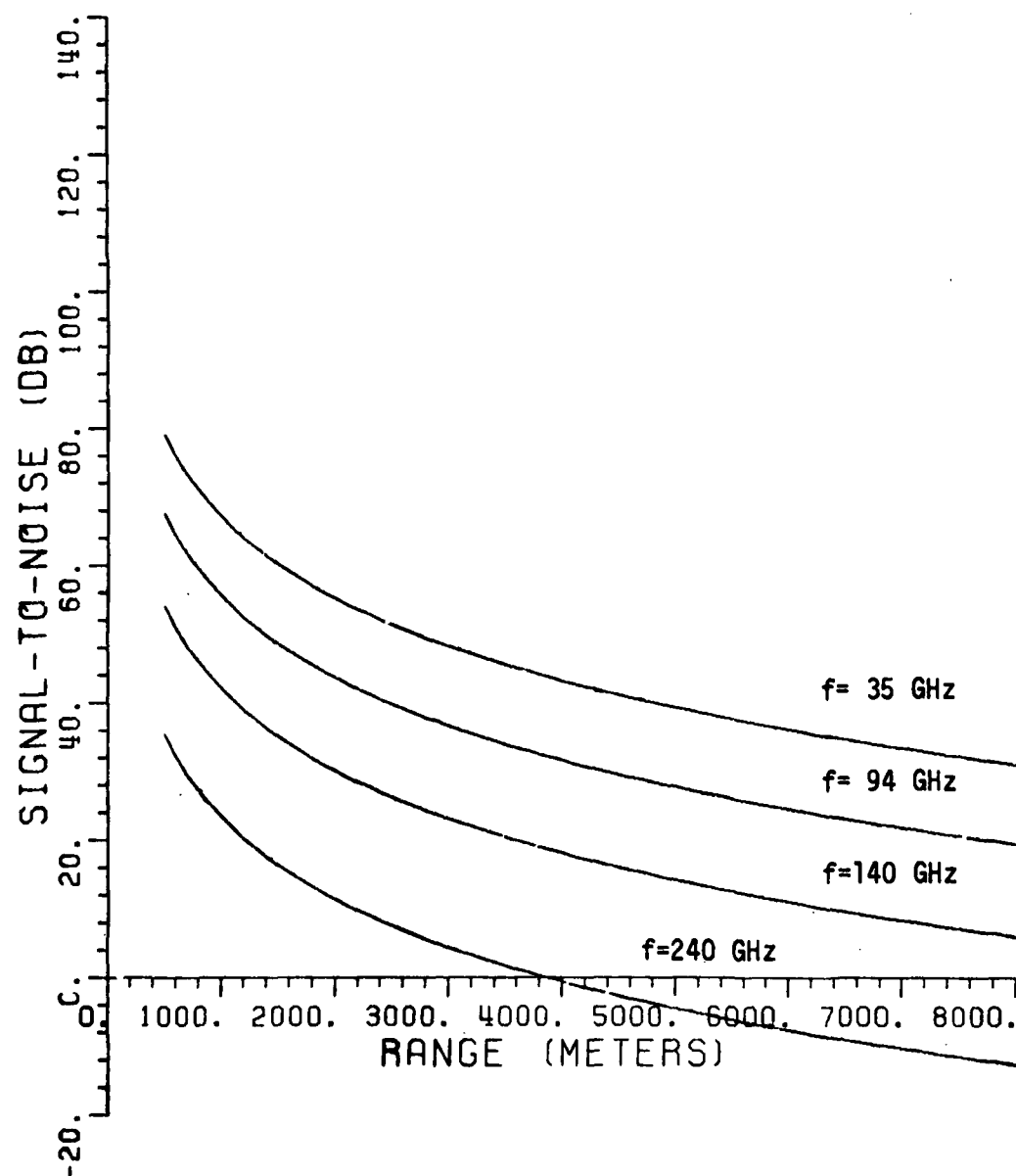


Figure 31. Signal-to-noise ratio versus Range for the single-ended pulsed source range gated radar employing post-detection integration.  $n=10,000$ ,  $\alpha=0$  dB/km, and  $\sigma=125$  m<sup>2</sup>.

For unspecified system parameters, see Table I, p. 53.

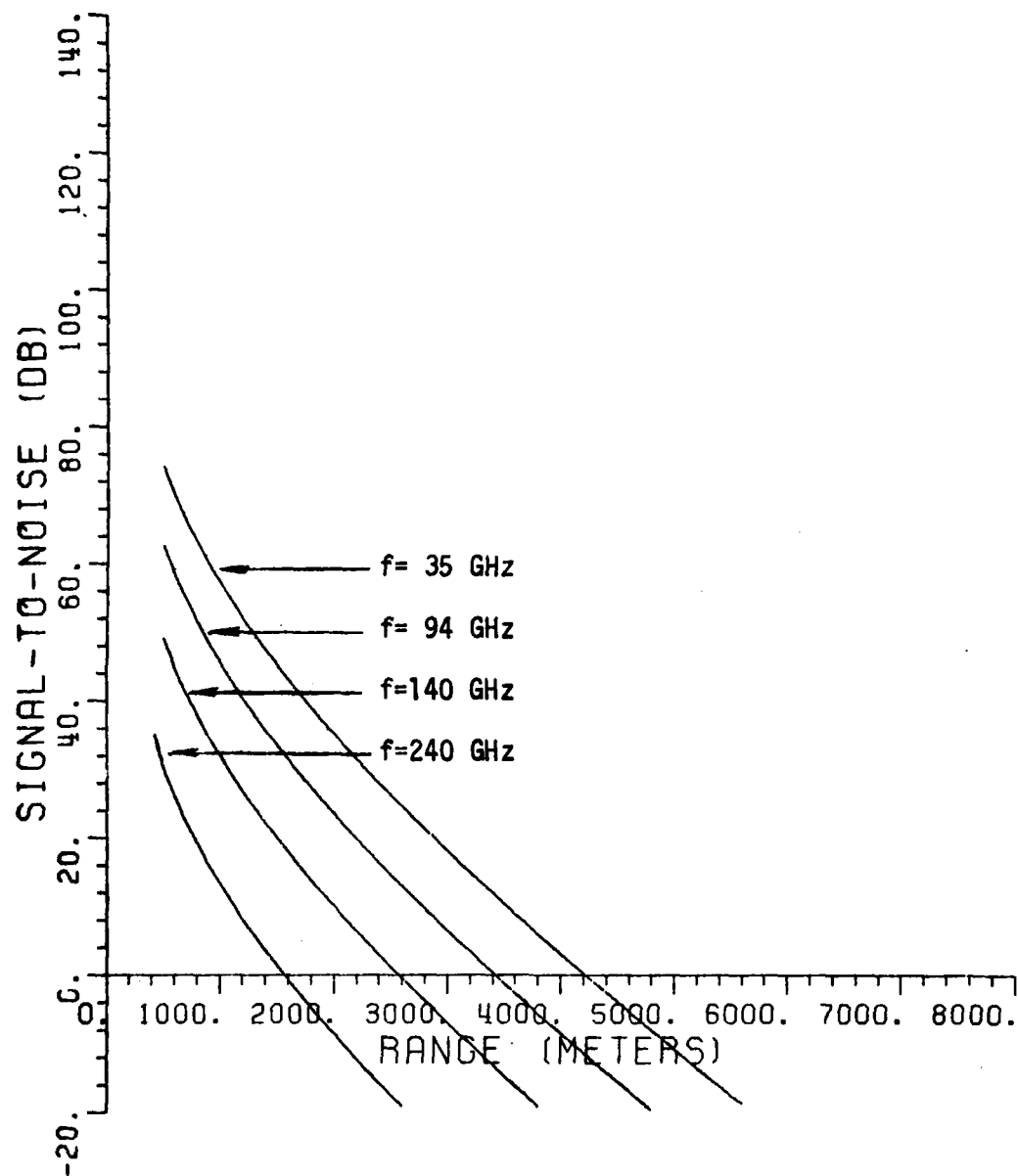


Figure 32. Signal-to-noise ratio versus Range for the single-ended pulsed source range gated radar employing post-detection integration.  $n = 10,000$ ,  $\alpha = 5$  dB/km, and  $\sigma = 125$  m<sup>2</sup>.

For unspecified system parameters, see Table I, p. 53.



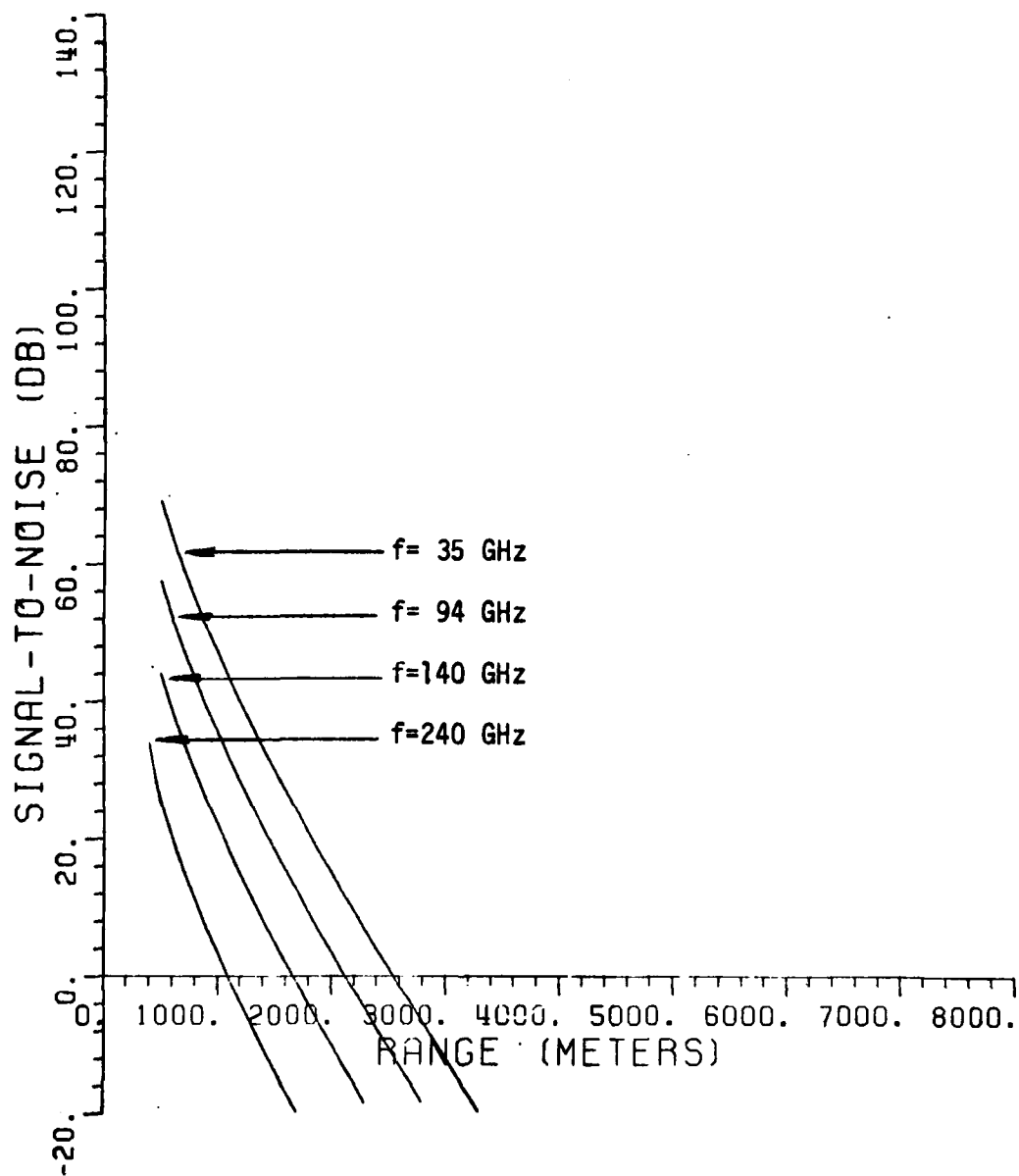


Figure 33. Signal-to-noise ratio versus Range for the single-ended pulsed source range gated radar employing post-detection integration.  $n=10,000$ ,  $\alpha=10$  dB/km, and  $\sigma=125$  m<sup>2</sup>.

For unspecified system parameters, see Table I, p. 53.

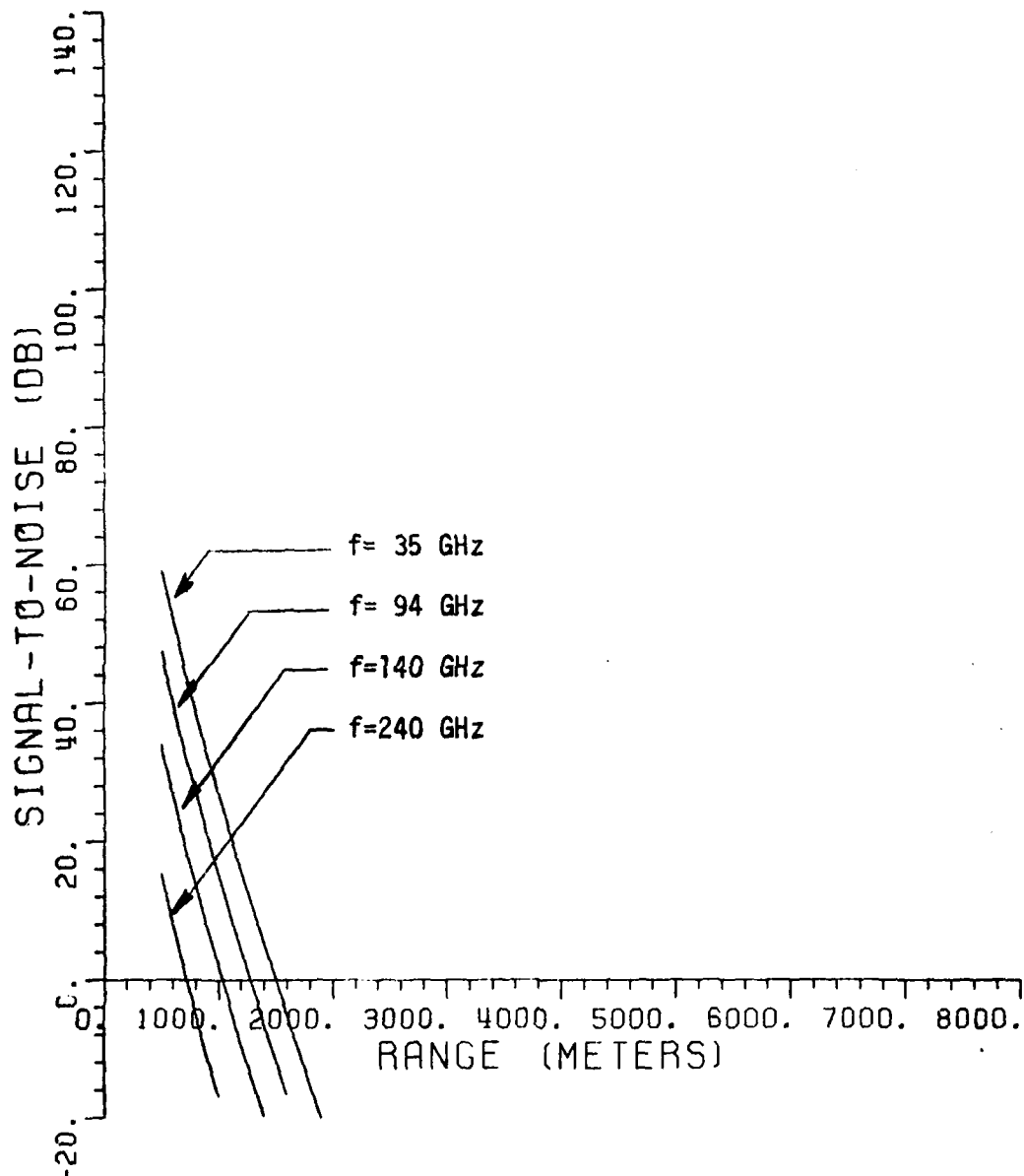


Figure 34. Signal-to-noise ratio versus Range for the single-ended pulsed source range gated radar employing post-detection integration.  $n=10,000$ ,  $\alpha=20$  dB/km, and  $\sigma=125$  m<sup>2</sup>.

For unspecified system parameters, see Table I, p. 53.

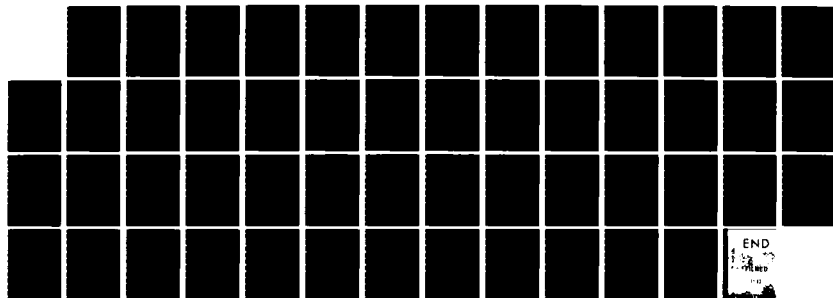
AD-A133 587

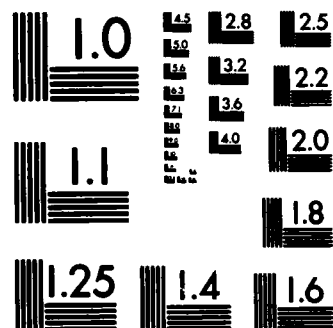
THE CALCULATED PERFORMANCE OF SOME RADAR AND  
TRANSMISSOMETER SYSTEMS IN R. (U) OHIO STATE UNIV  
COLUMBUS ELECTROSCIENCE LAB E L UTT ET AL. DEC 82  
ESL-713671-2-VOL-1 AFWAL-TR-82-1147-VOL-1 F/G 17/9

2/2

UNCLASSIFIED

NL





MICROCOPY RESOLUTION TEST CHART  
NATIONAL BUREAU OF STANDARDS-1963-A

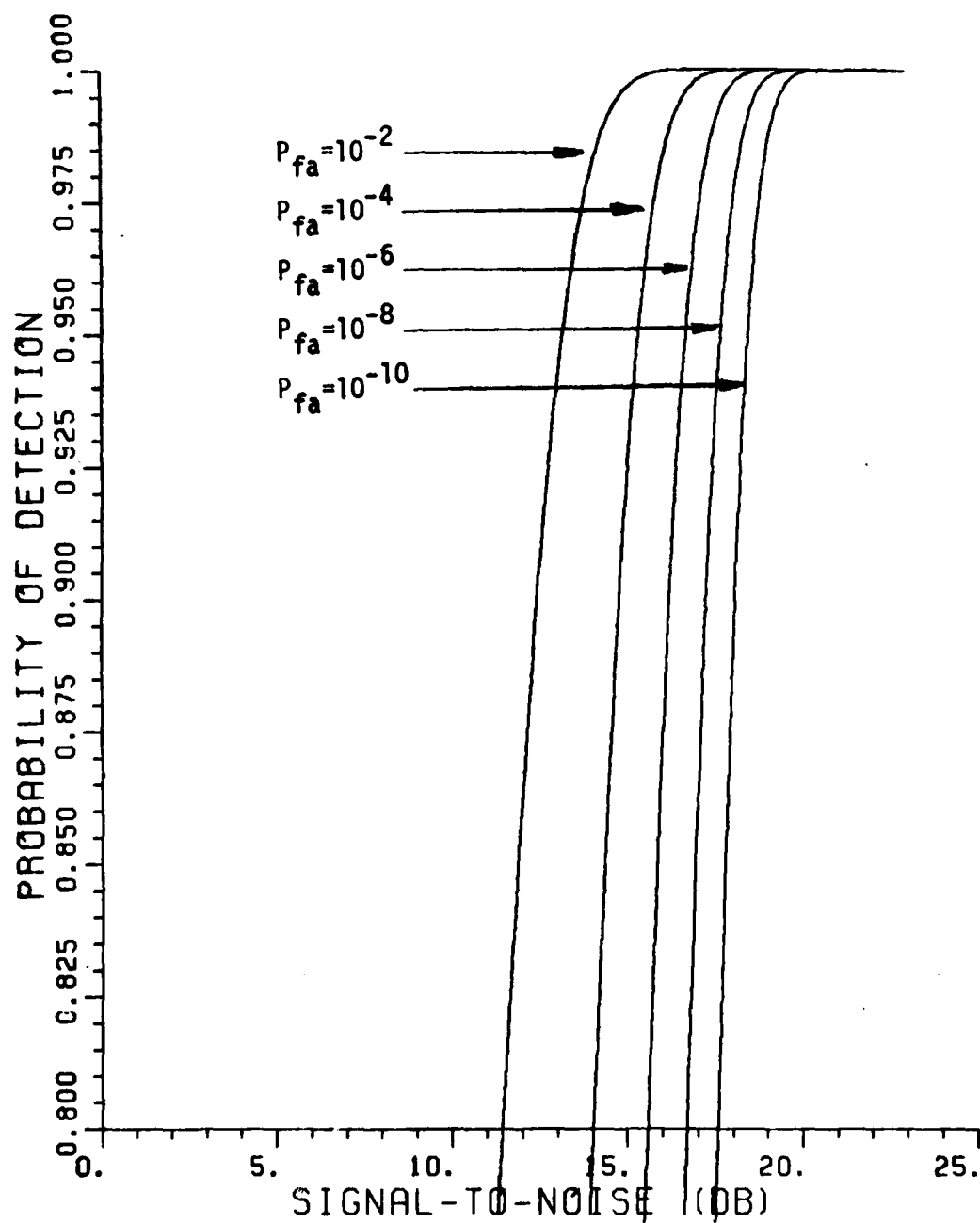


Figure 35. Probability of Detection versus Post-detection Signal-to-noise ratio for the single-ended pulsed source range gated radar.

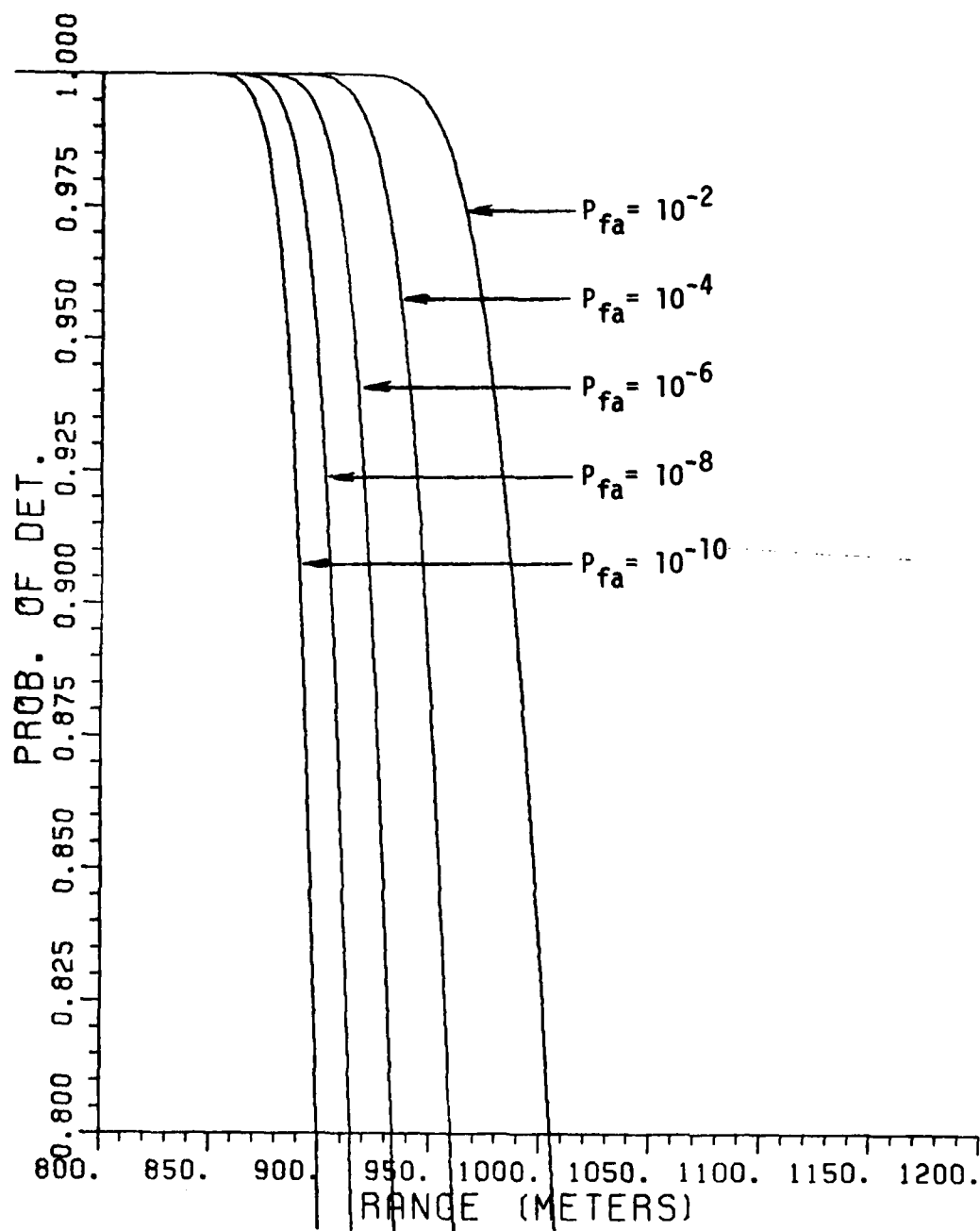


Figure 36. Probability of Detection versus Range for the single-ended pulsed source range gated radar.  $f = 94$  GHz,  $\alpha = 20$  dB/km, and  $\sigma = 125$  m<sup>2</sup>.

For unspecified system parameters, see Table I, p. 53.

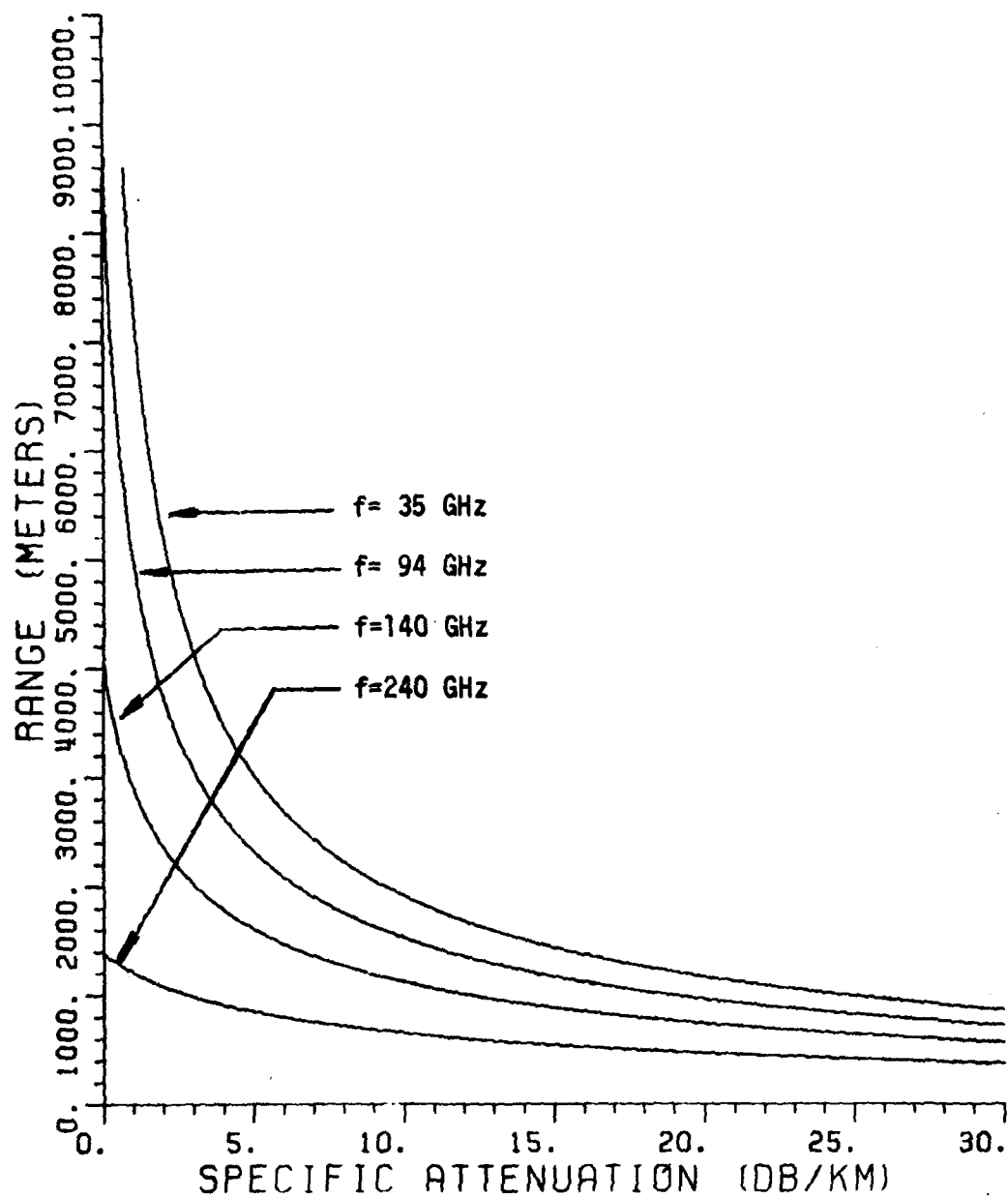


Figure 37. Range versus Specific Attenuation for the single-ended pulsed source range gated radar employing post-detection integration.  $P_d = 0.995$ ,  $P_{fa} = 10^{-6}$  (Computed processed  $E/N = 17.79$  dB.)

For unspecified system parameters, see Table I, p. 53.

Finally, Figure 37 shows the effects of specific attenuation and frequency on radar range performance. For a required probability of detection of 0.995 and probability of false alarm of  $10^{-6}$ , a processed signal-to-noise ratio of 17.79 dB is computed.

As with the transmission systems analyzed earlier in this section, both frequency and specific attenuation increases can greatly reduce radar range. All graphs presented in this section are derived from the computer program BOXCAR given in Volume II.

#### 5. Pulsed Source with a Quadrature Receiver.

As discussed in Section II.B.5, this system is a true pulsed radar which uses a range gated quadrature receiver. Typical performance of this radar system is shown in Figures 38 through 44 presented below.

Figures 38 through 41 display the signal-to-noise ratio versus range for various values of frequency and specific attenuation. From these graphs, note that even with 20 dB/km attenuation, a range of between 1000 and 2000 meters can be expected. This is slightly better than the two-way propagation system using square-law detection, however, not nearly as good as the CW source with quadrature receiver.

Figures 42 and 43 show the probability of detecting a  $10 \text{ m}^2$  target as a function of processed signal-to-noise ratio and range. As with the earlier systems, we are again assuming false alarm probabilities of  $10^{-2}$ ,  $10^{-4}$ ,  $10^{-6}$ ,  $10^{-8}$ , and  $10^{-10}$ ; the transmitted frequency in Figure 43 is 94 GHz. For this pulse radar, a processed signal-to-noise ratio of at least 18 dB is required for a near 100% probability of detecting the calibrated target. This will require the target to be no more than about 1950 meters from the transmitting and receiving



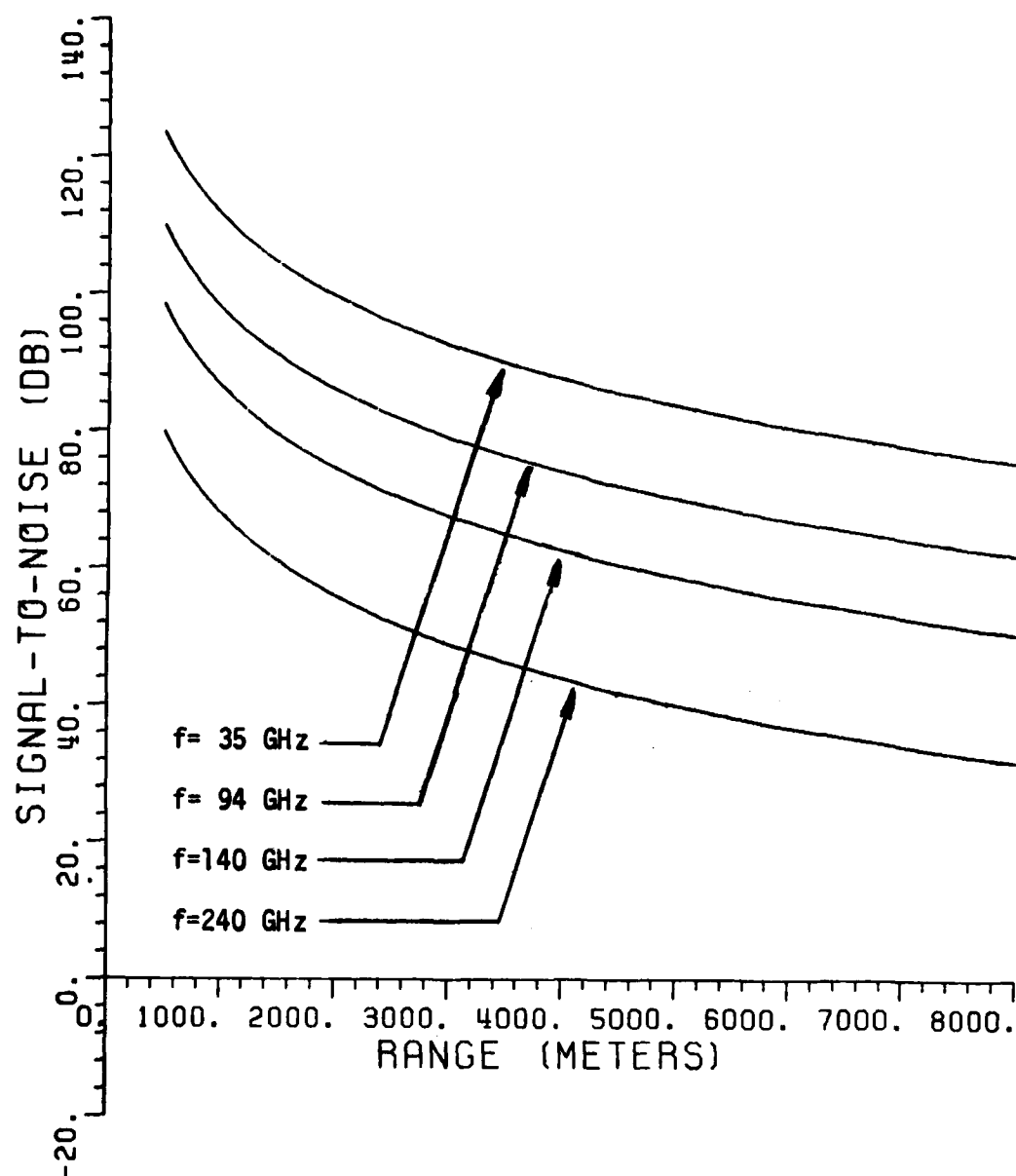


Figure 38. Signal-to-noise ratio versus Range for the single-ended pulsed radar system with quadrature receiver.  
 $\alpha = 0$  dB/km,  $\sigma = 10$  m<sup>2</sup>.

For unspecified system parameters, see Table I, p. 53.

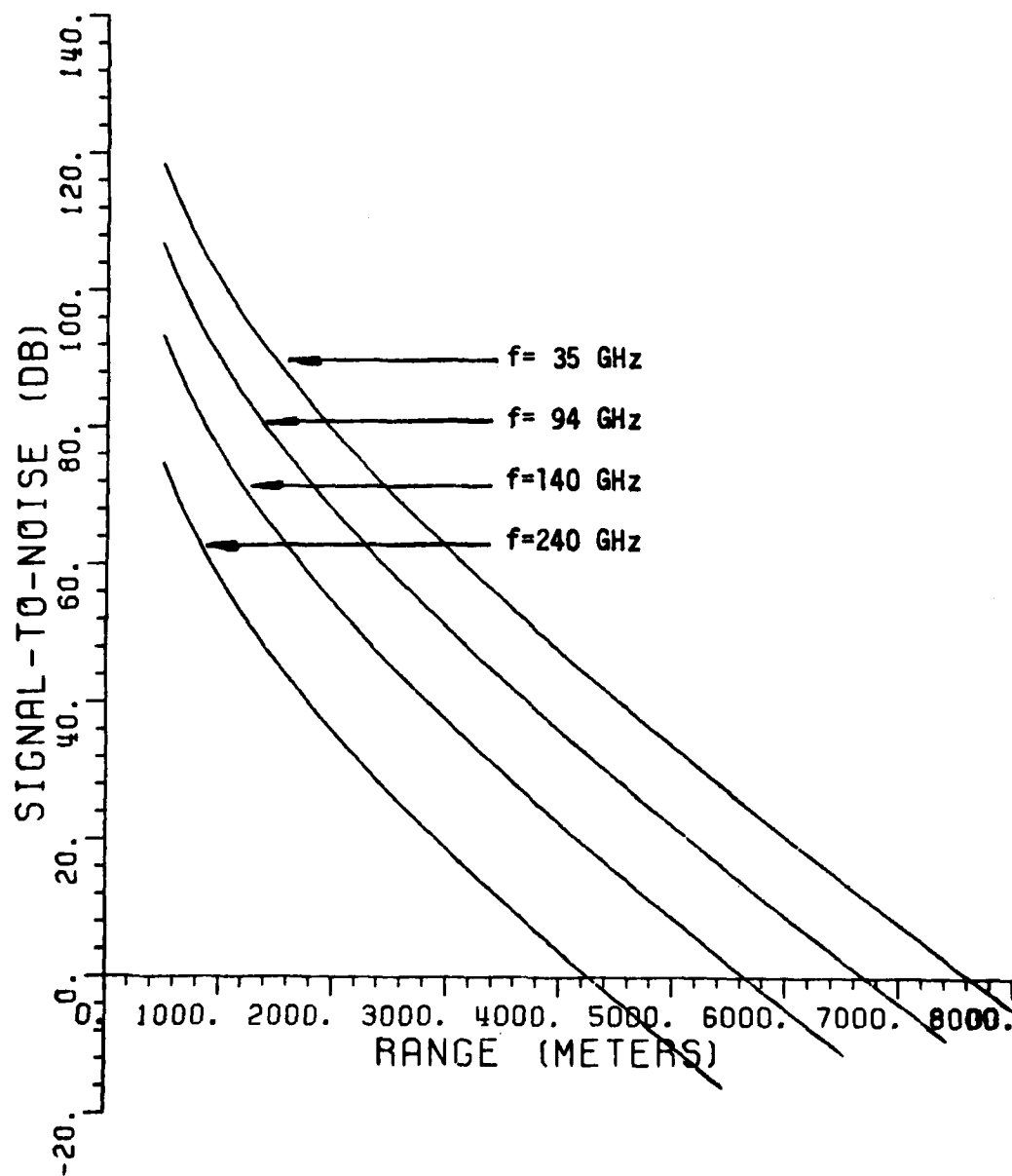


Figure 39. Signal-to-noise ratio versus Range for the single-ended pulsed radar system with quadrature receiver.  $\alpha = 5$  dB/km,  $\sigma = 10$  m<sup>2</sup>.  
For unspecified system parameters, see Table I, p. 53.

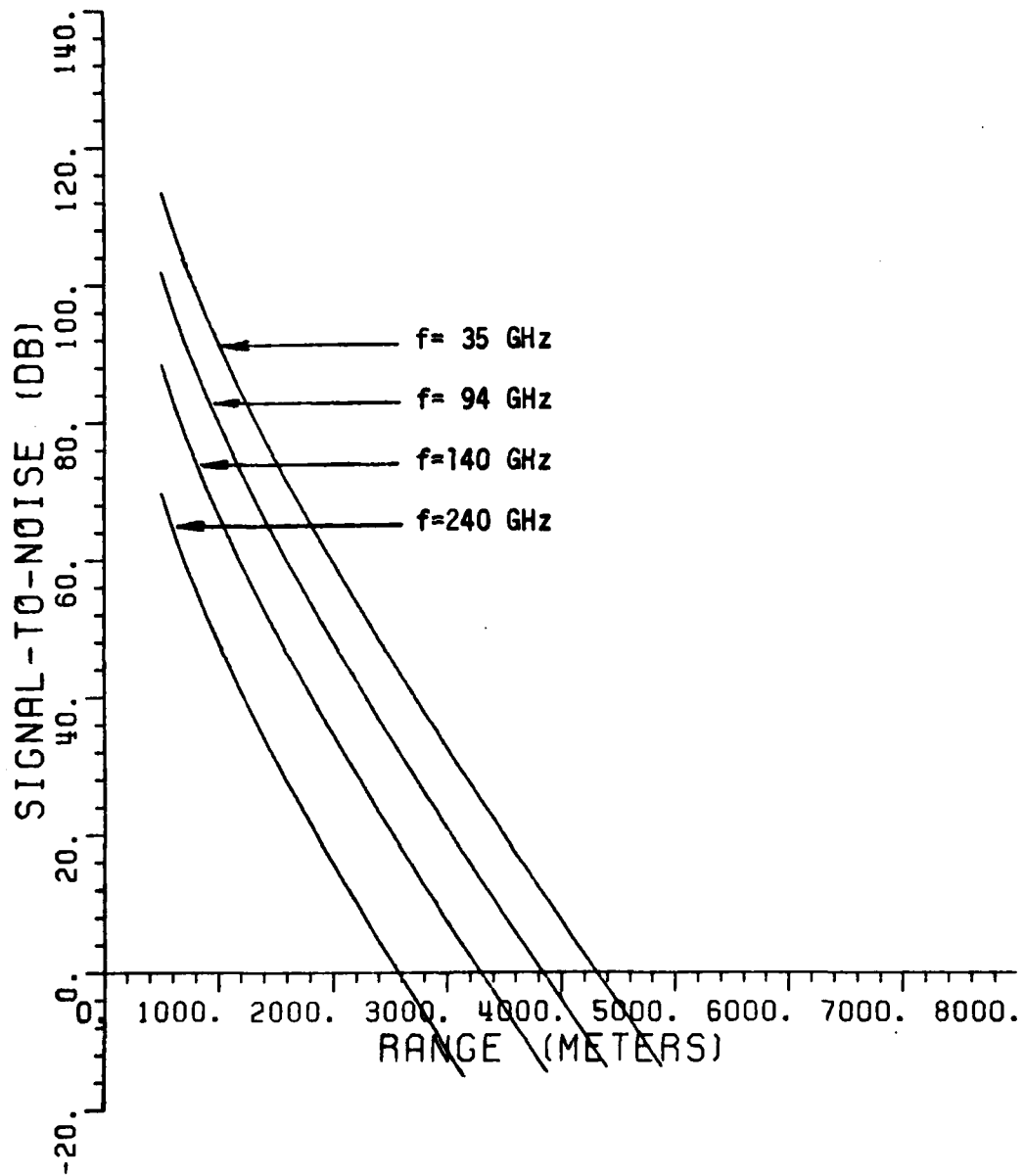


Figure 40. Signal-to-noise ratio versus Range for the single-ended pulsed radar system with quadrature receiver.  $\alpha = 10$  dB/km,  $\sigma = 10$  m<sup>2</sup>.  
For unspecified system parameters, see Table I, p. 53.

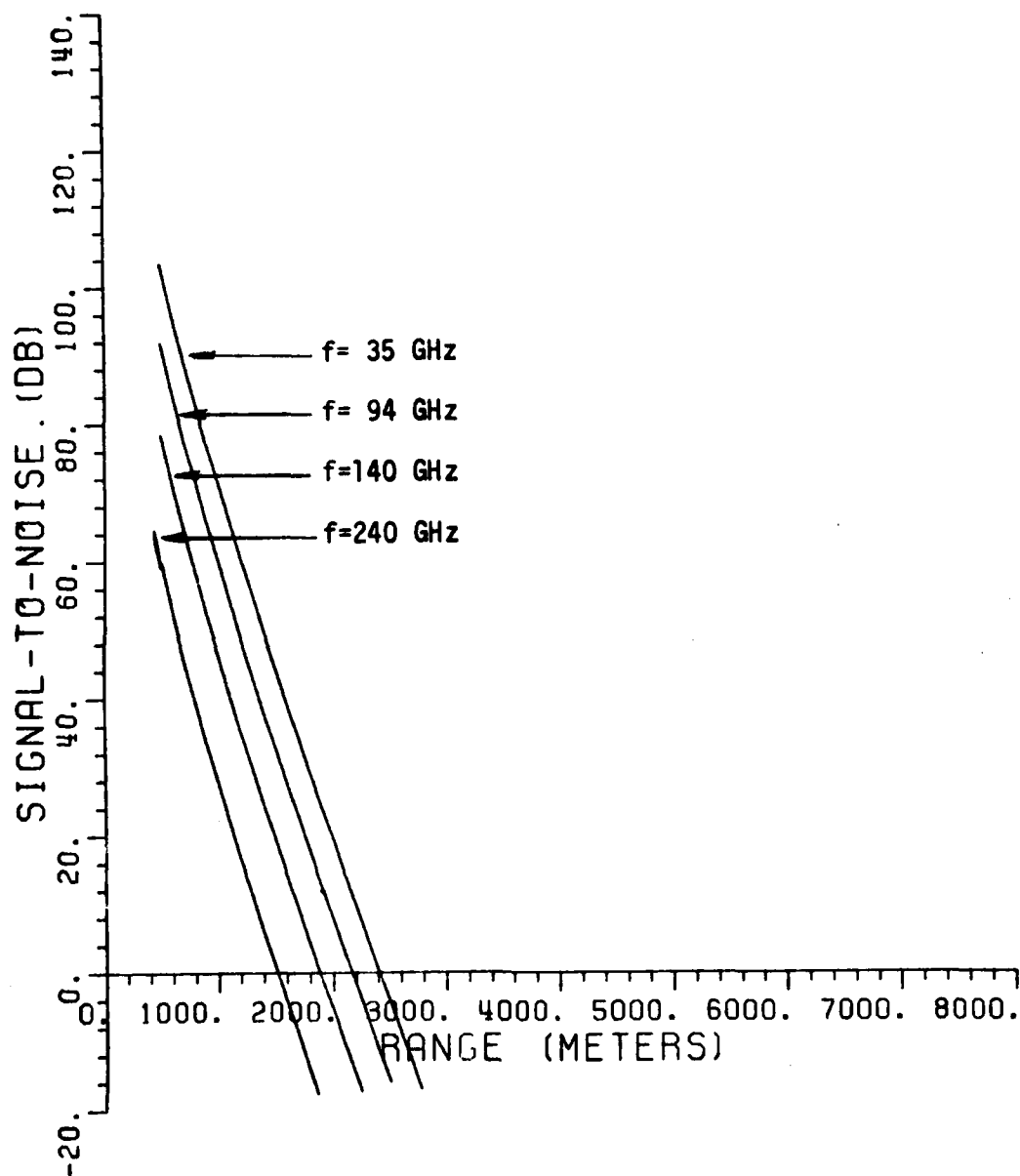


Figure 41. Signal-to-noise ratio versus Range for the single-ended pulsed radar system with quadrature receiver.  
 $\alpha = 20$  dB/km,  $\sigma = 10$  m<sup>2</sup>.

For unspecified system parameters, see Table I, p. 53.

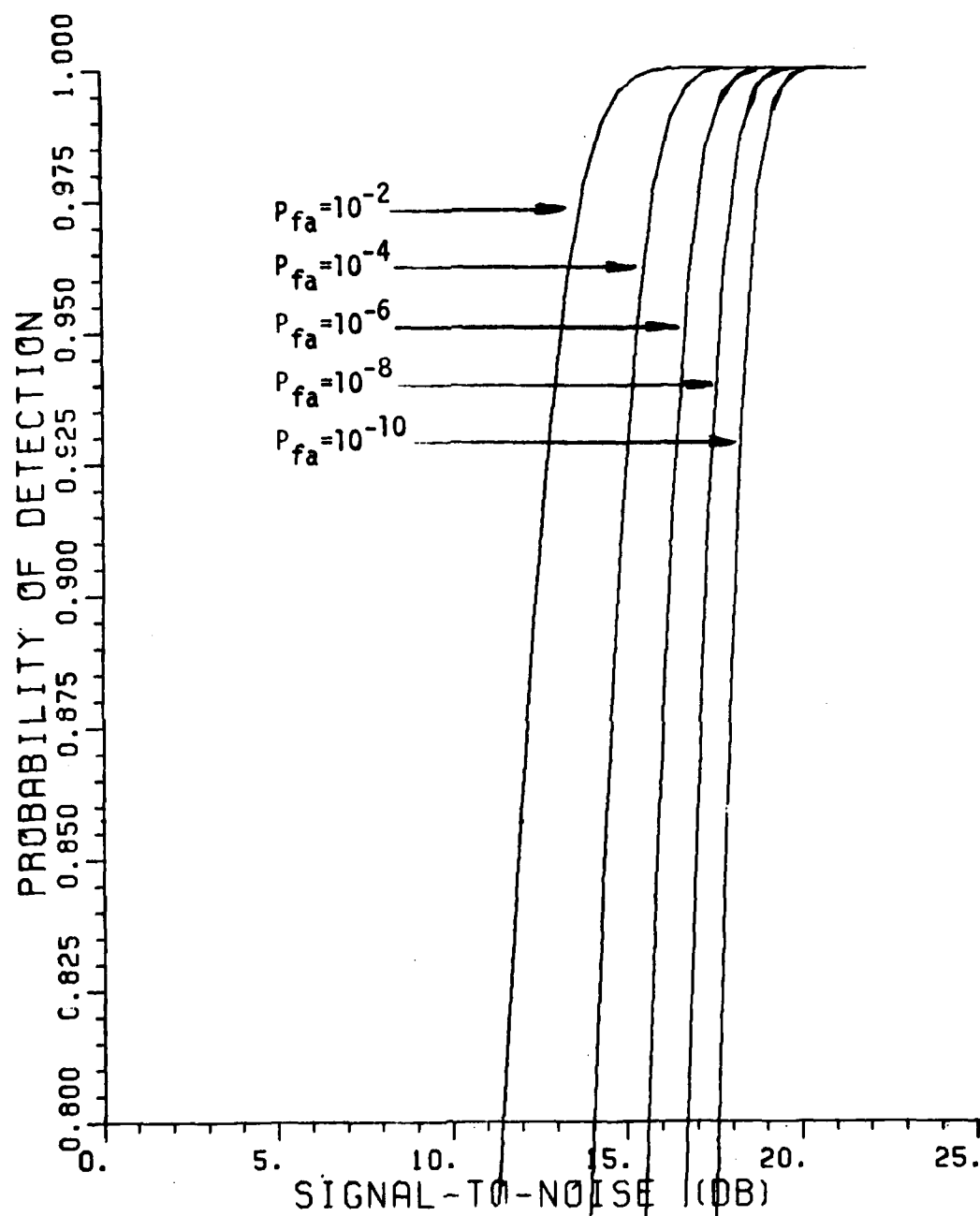


Figure 42. Probability of Detection versus Post-detection Signal-to-noise ratio for a single-ended pulsed radar system with quadrature receiver.

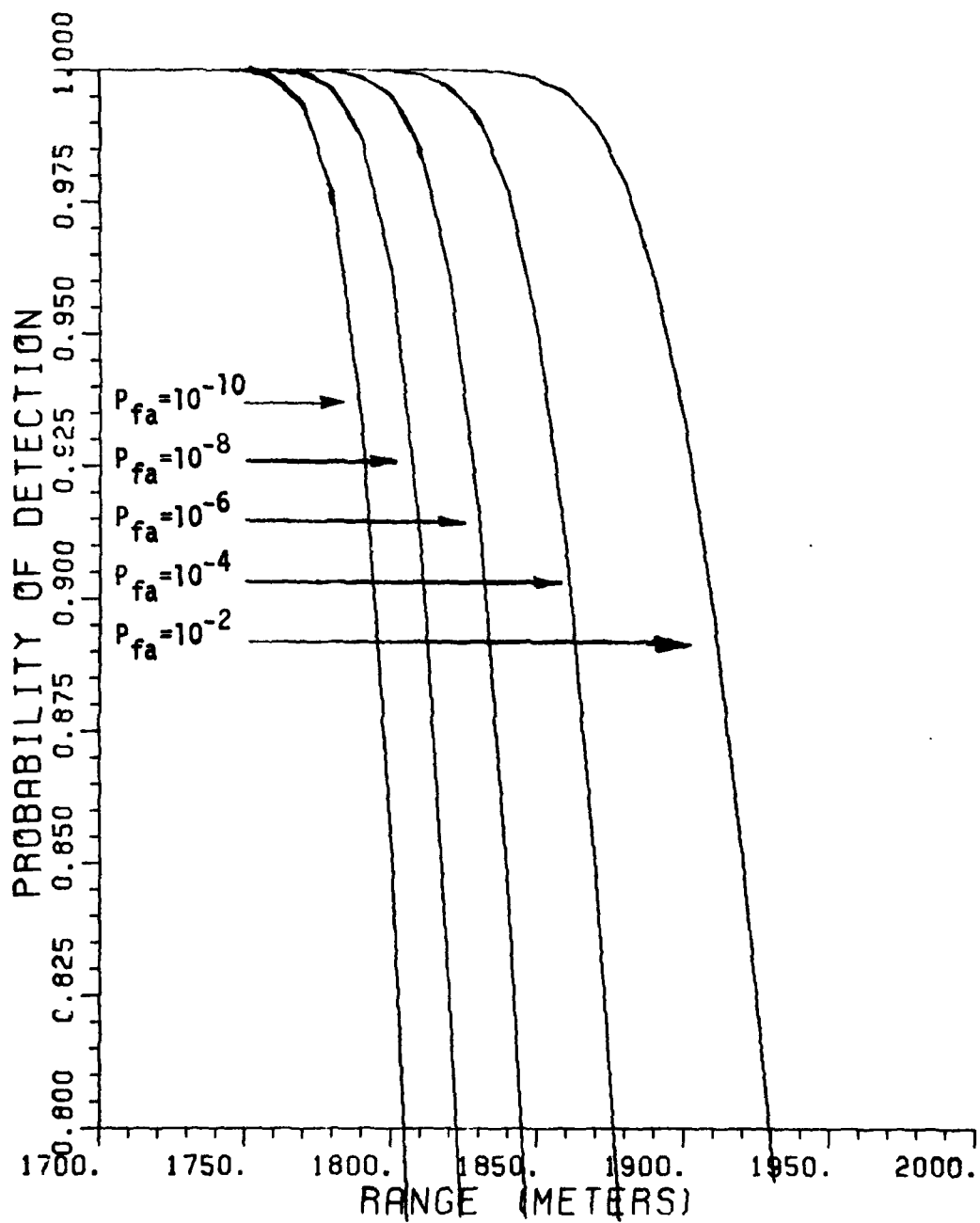


Figure 43. Probability of Detection versus Range for a single-ended pulsed radar system with quadrature receiver.  $f = 94$  GHz,  $\alpha = 20$  dB/km, and  $\sigma = 10$  m<sup>2</sup>.

For unspecified system parameters, see Table I, p. 53.

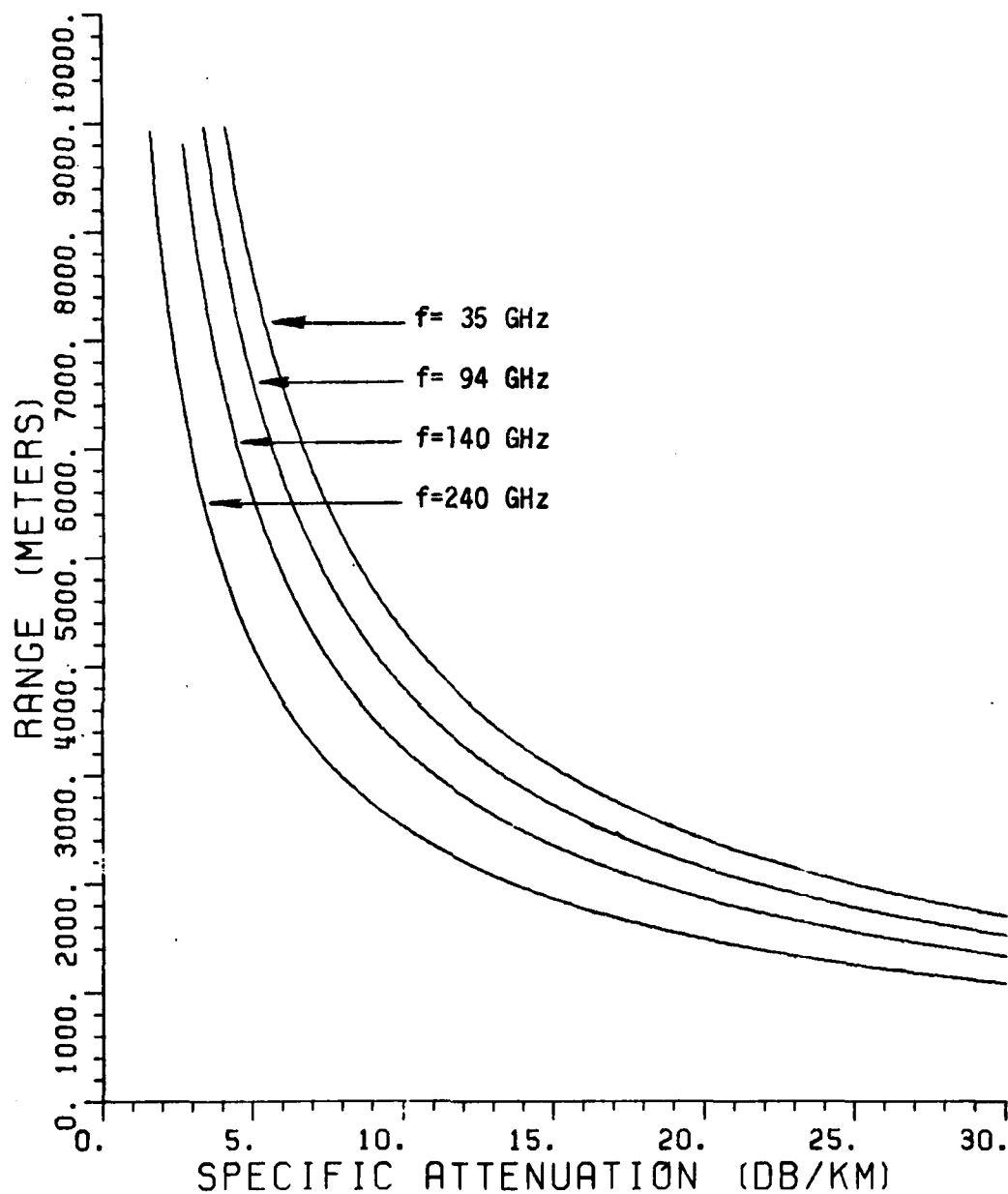


Figure 44. Range versus Specific Attenuation for the single-ended pulsed radar system with quadrature receiver.  $P_d = 0.995$ ,  $P_{fa} = 10^{-6}$  (Computed processed E/N = 17.79 dB.)

For unspecified system parameters, see Table I, p. 53.

antennas.

Finally, Figure 44 shows the range versus specific attenuation for the pulsed radar and quadrature receiver. For a 0.995 probability of detection and  $10^{-6}$  probability of false alarm, the computed processed signal-to-noise ratio at the output of the detector is 17.79 dB. All graphs presented here are derived from the computer algorithm CONET@ presented in Volume II.

#### 6. Pulsed Source with Linear FM Rectangular-Envelope Pulse Compression

As discussed in Section II.B.6, this system is a true pulse radar which uses a pulse compression filter and range gated quadrature receiver. Typical performance of this radar system is shown in Figures 45 through 51 shown below where a pulse compression ratio of 150:1 and  $10 \text{ m}^2$  target cross section area are assumed.

Figures 45 through 48 show the signal-to-noise ratio versus range for various values of frequency and specific attenuation. From the graphs of signal-to-noise ratio versus range, even with 20 dB/km attenuation, a range between 1800 and 2600 meters can be expected. This is about the same range as predicted with the single-ended CW system with quadrature receiver for a comparable radar cross section. However, this range is not as good as for the double-ended system.

Figures 49 and 50 show the probability of detecting a  $10 \text{ m}^2$  target as a function of processed signal-to-noise ratios and radar range. As with previous systems, a transmitted frequency of 94 GHz is assumed in Figure 50, as well as, false alarm probabilities of  $10^{-2}$ ,  $10^{-4}$ ,  $10^{-6}$ ,  $10^{-8}$ , and  $10^{-10}$  in both figures.



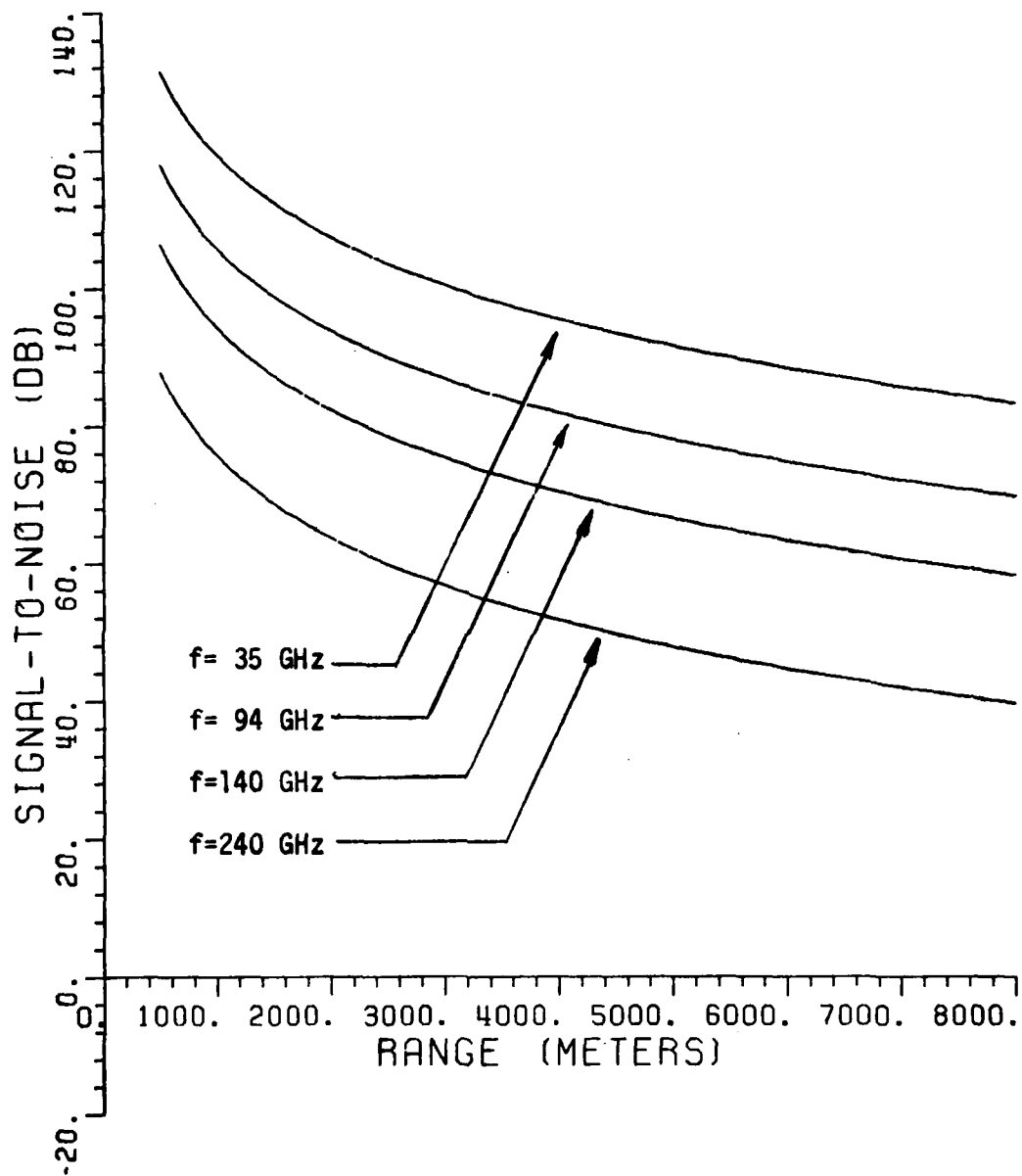


Figure 45. Signal-to-noise ratio versus Range for the single-ended pulsed radar system with pulse compression.  
 $\alpha = 0$  dB/km,  $\sigma = 10$  m<sup>2</sup>.

For unspecified system parameters, see Table I, p. 53.

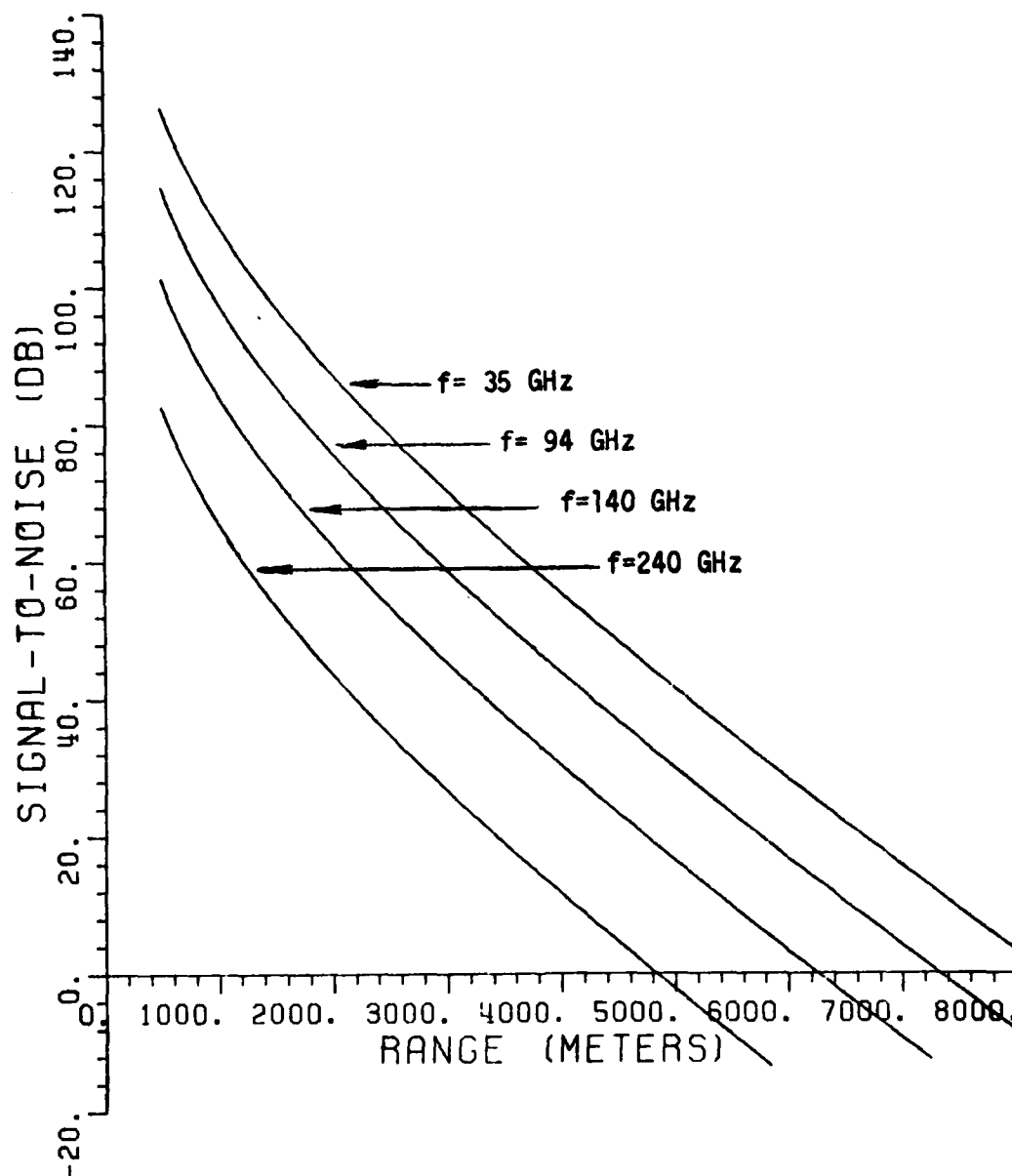


Figure 46. Signal-to-noise ratio versus Range for the single-ended pulsed radar system with pulse compression.  
 $\alpha = 5$  dB/km,  $\sigma = 10$  m<sup>2</sup>.

For unspecified system parameters, see Table I, p. 53.

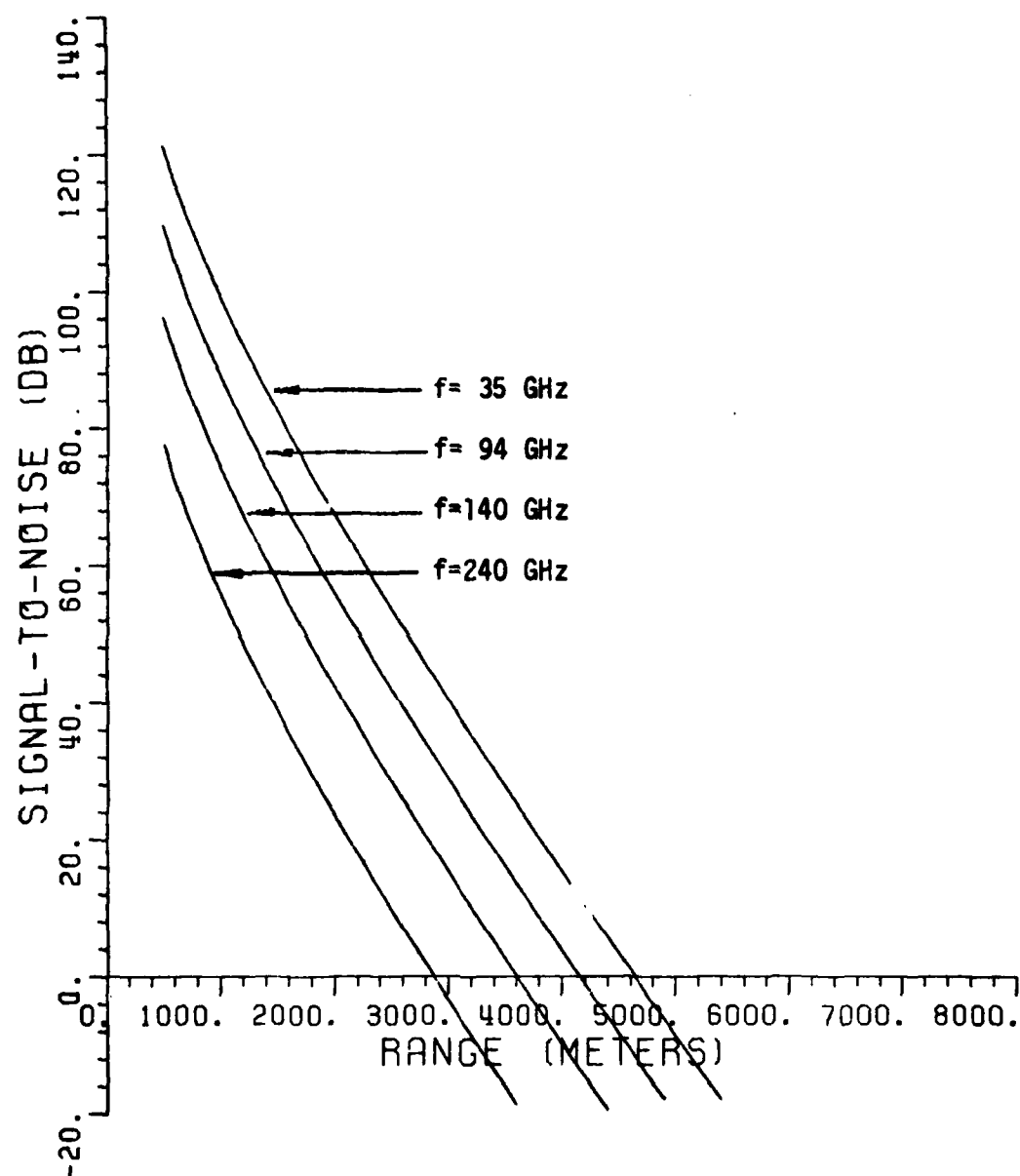


Figure 47. Signal-to-noise ratio versus Range for the single-ended pulsed radar system with pulse compression.  
 $\alpha = 10$  dB/km,  $\sigma = 10$  m<sup>2</sup>.  
 For unspecified system parameters, see Table I, p. 53.

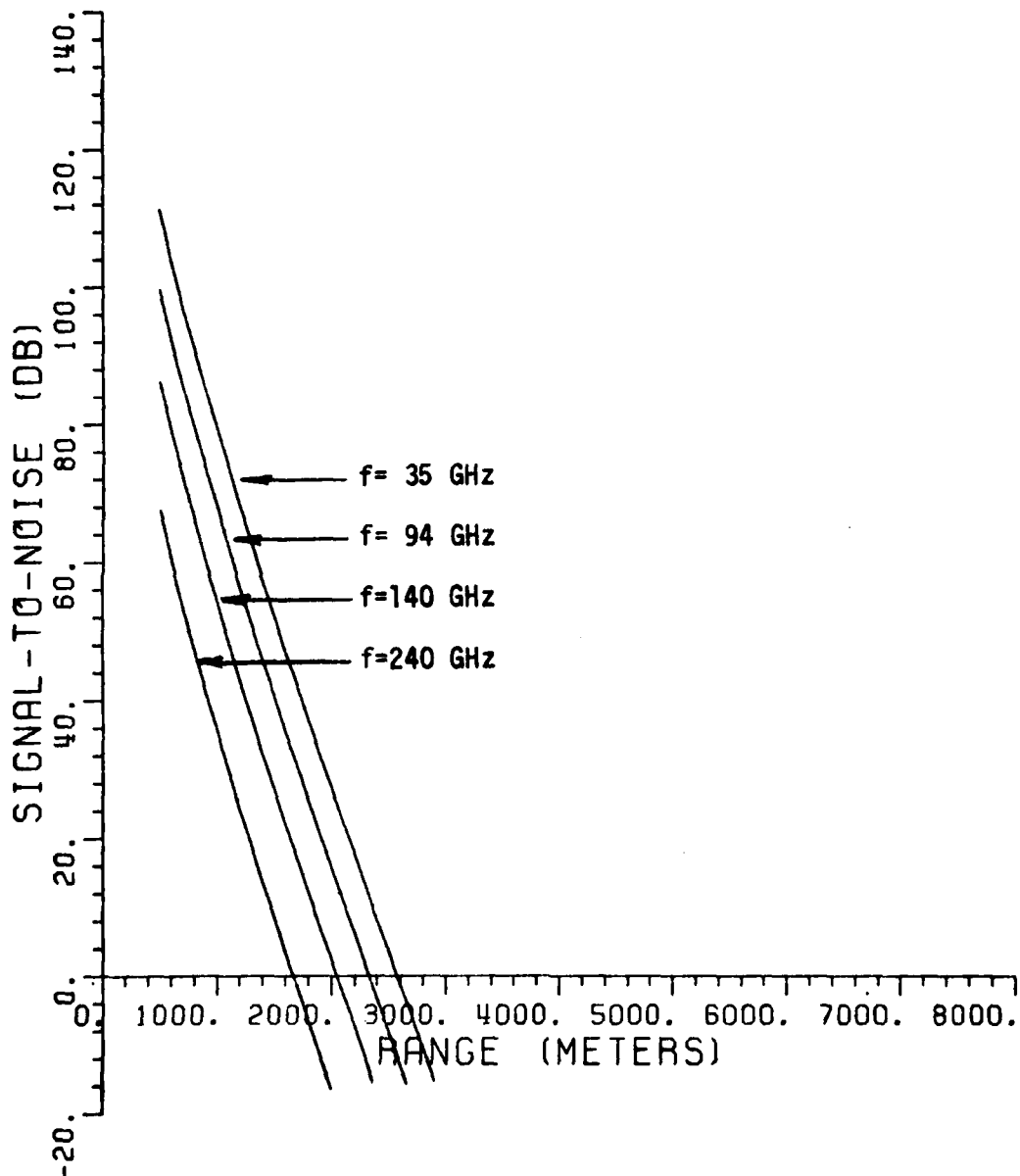


Figure 48. Signal-to-noise ratio versus Range for the single-ended pulsed radar system with pulse compression.  
 $\alpha = 20$  dB/km,  $\sigma = 10$  m<sup>2</sup>.  
 For unspecified system parameters, see Table I, p. 53.

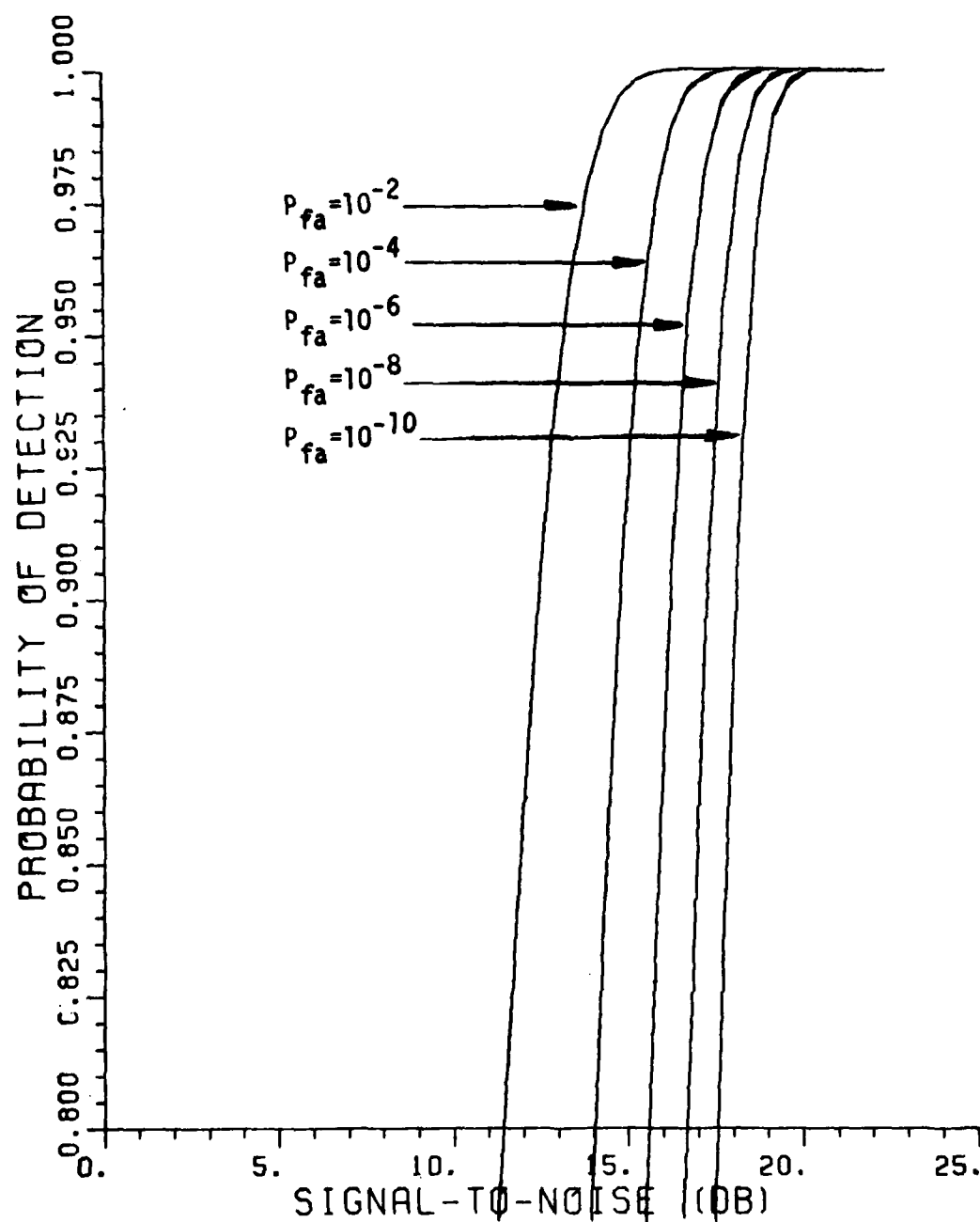


Figure 49. Probability of Detection versus Post-detection Signal-to-noise ratio for a single-ended pulsed radar system with pulse compression.

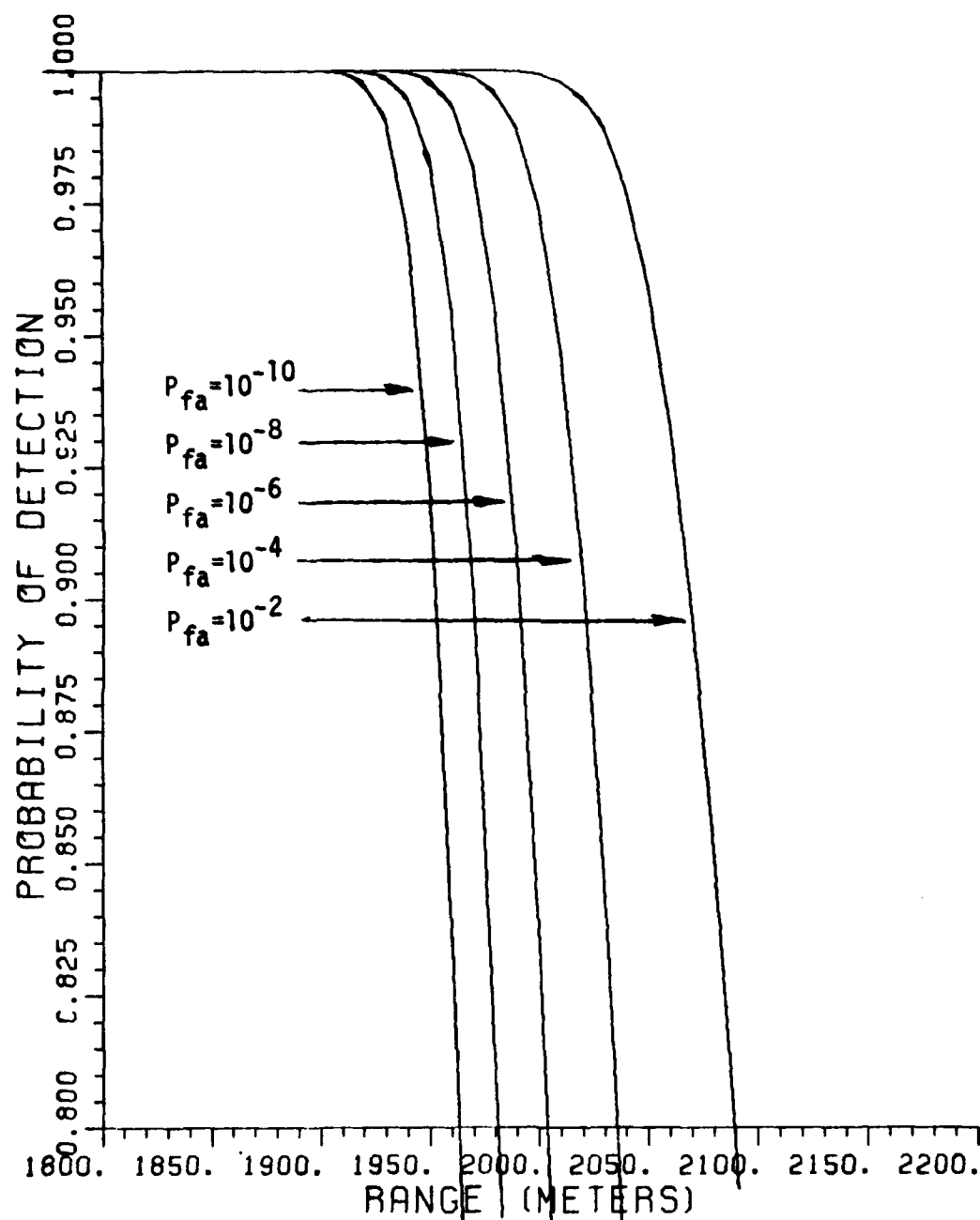


Figure 50. Probability of Detection versus Range for a single-ended pulsed radar system with pulse compression.  
 $f = 94$  GHz,  $\alpha = 20$  dB/km and  $\sigma = 10$  m<sup>2</sup>.

For unspecified system parameters, see Table I, p. 53.

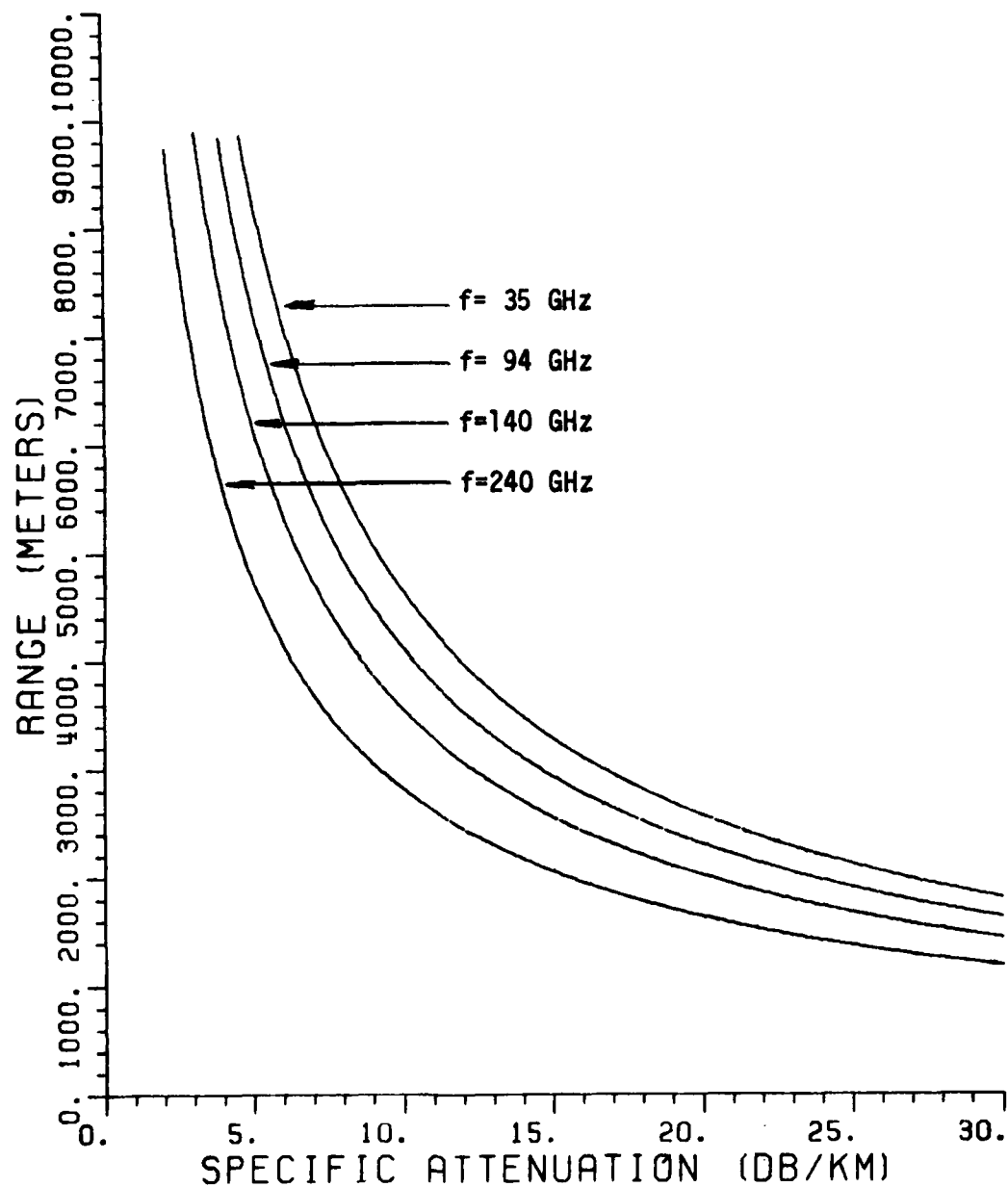


Figure 51. Range versus Specific Attenuation for the single-ended pulsed radar system with pulse compression.  $P_d = 0.995$ ,  $P_{fa} = 10^{-6}$  (Computed processed  $E/N = 17.79$  dB.)  
For unspecified system parameters, see Table I, p. 53.

Finally, Figure 51 shows the range versus specific attenuation for the pulsed radar with pulse compression. Using the same probability of detection and probability of false alarm as in previous systems requires a processed signal-to-noise ratio of 17.79 dB at the output of the detector. All graphs presented in this section are derived from the computer algorithm COMPRESS presented in Volume II.



### 8. Effects of Rain Attenuation

As discussed in Section IV, it is possible to develop a computer algorithm to compute the specific attenuation for a specified rain rate. For this study, an exponential rain drop-size distribution given by Equation (97) and a routine to determine complex index of refraction for liquid water is used (see Appendix A.) The rain water refractive index is a function of temperature and frequency. Typical values of the complex index of refraction for water at millimeter wavelengths are shown in TABLE II below.

A computer subroutine for calculating specific attenuation can be applied to plot maximum range for any of the six systems discussed in Section II as a function of rain rate. In this calculation, the attenuation is a function of temperature; however, the effects of temperature on radar range is negligible. In the discussion presented here, graphs showing range as a function of rain rate will be given for each of the systems of Section II with a temperature of 20°C assumed.

The drop-size distribution is used as a subprogram. By changing this subroutine, we can calculate extinction due to rain with other expressions or empirical data for drop-size distributions. This is useful because smaller drops become very important in the millimeter wave region so that the effect of drop-size distribution may be important. In this thesis, the Marshall-Palmer exponential distribution [2] is used exclusively. Also, it should be noted that the subroutine works well for attenuation through fog when given an appropriate drop-size distribution.

TABLE II

Calculated Complex Index of Refraction of Pure Water  
for Various Wavelengths and Temperatures

<u>Frequency (GHz)</u>	<u>Temperature (°C)</u>	<u>Complex Index of Refraction</u> <u>n</u>
35	0	4.032-j2.450
35	10	4.610-j2.673
35	20	5.200-j2.797
35	30	5.771-j2.799
94	0	2.810-j1.379
94	10	3.073-j1.653
94	20	3.359-j1.929
94	30	3.674-j2.191
140	0	2.575-j1.015
140	10	2.748-j1.254
140	20	2.929-j1.514
140	30	3.131-j1.784
240	0	2.405-j0.635
240	10	2.496-j0.810
240	20	2.571-j1.018
240	30	2.645-j1.257

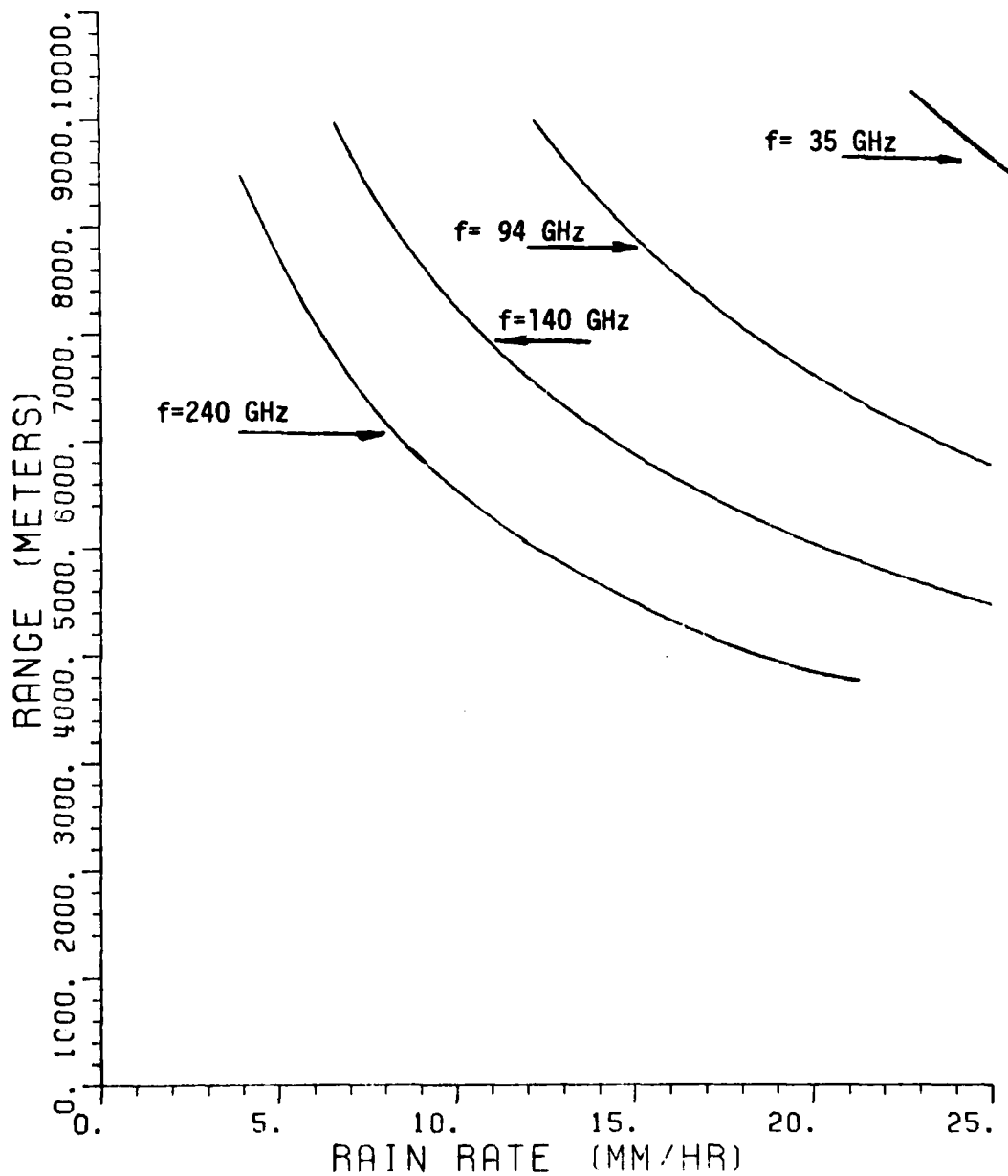


Figure 52. Range versus Rain Rate for the double-ended system with square-law detection.  $E/N = 10$  dB and  $T = 20^\circ\text{C}$ . For unspecified system parameters, see Table I, p. 53.

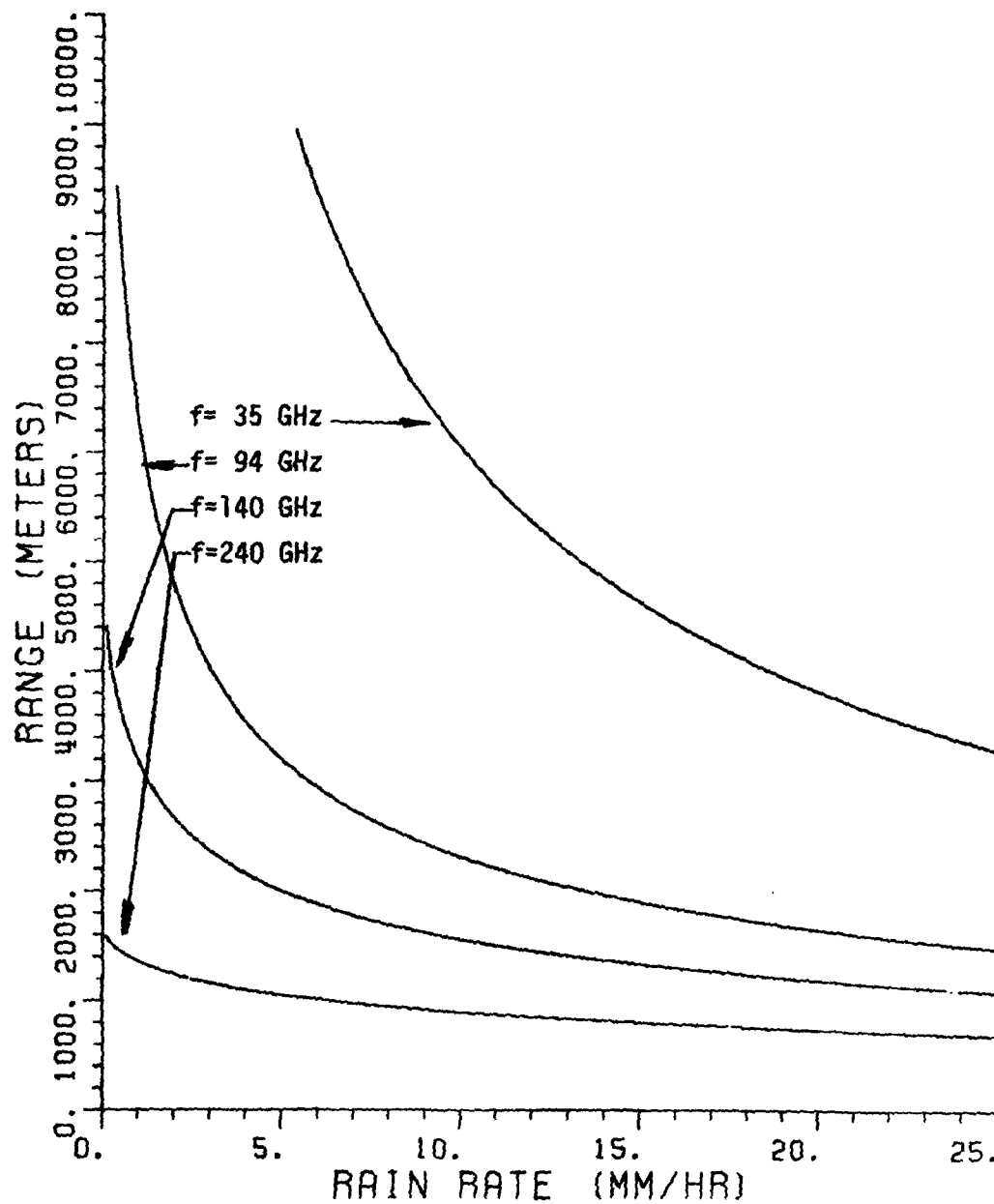


Figure 53. Range versus Rain Rate for the single-ended system with square-wave modulation and square-law detection.  $P_d = 0.995$ ,  $P_{fa} = 10^{-6}$ ,  $\sigma = 125 \text{ m}^2$ , and  $T = 20^\circ\text{C}$ . For unspecified system parameters, see Table I, p. 53.

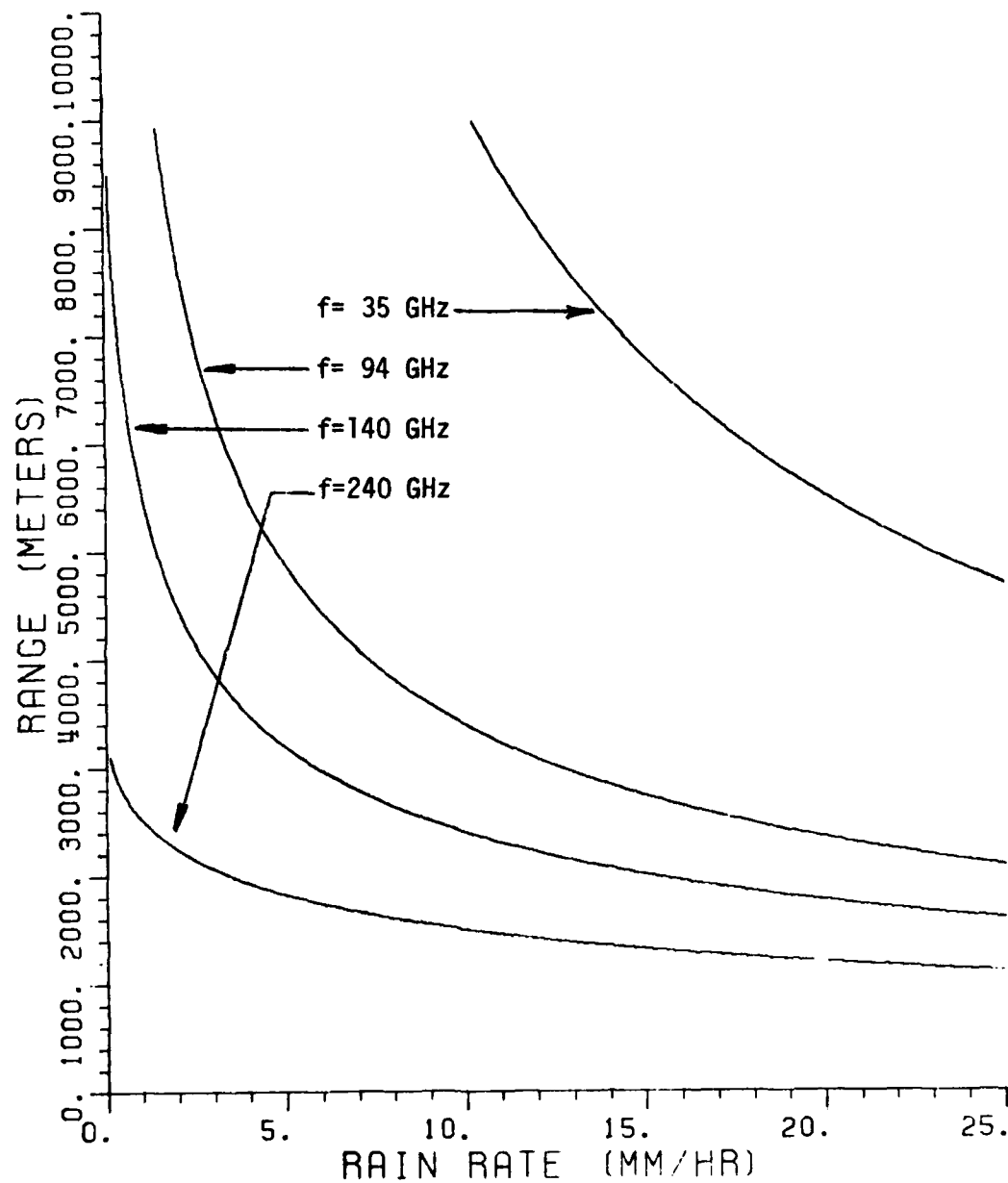


Figure 54. Range versus Rain Rate for the single-ended CW system with a quadrature receiver.  $P_d = 0.995$ ,  $P_{fa} = 10^{-6}$ ,  $\sigma = 125$  m $^2$ , and  $T = 20^\circ\text{C}$ .

For unspecified system parameters, see Table I, p. 53.

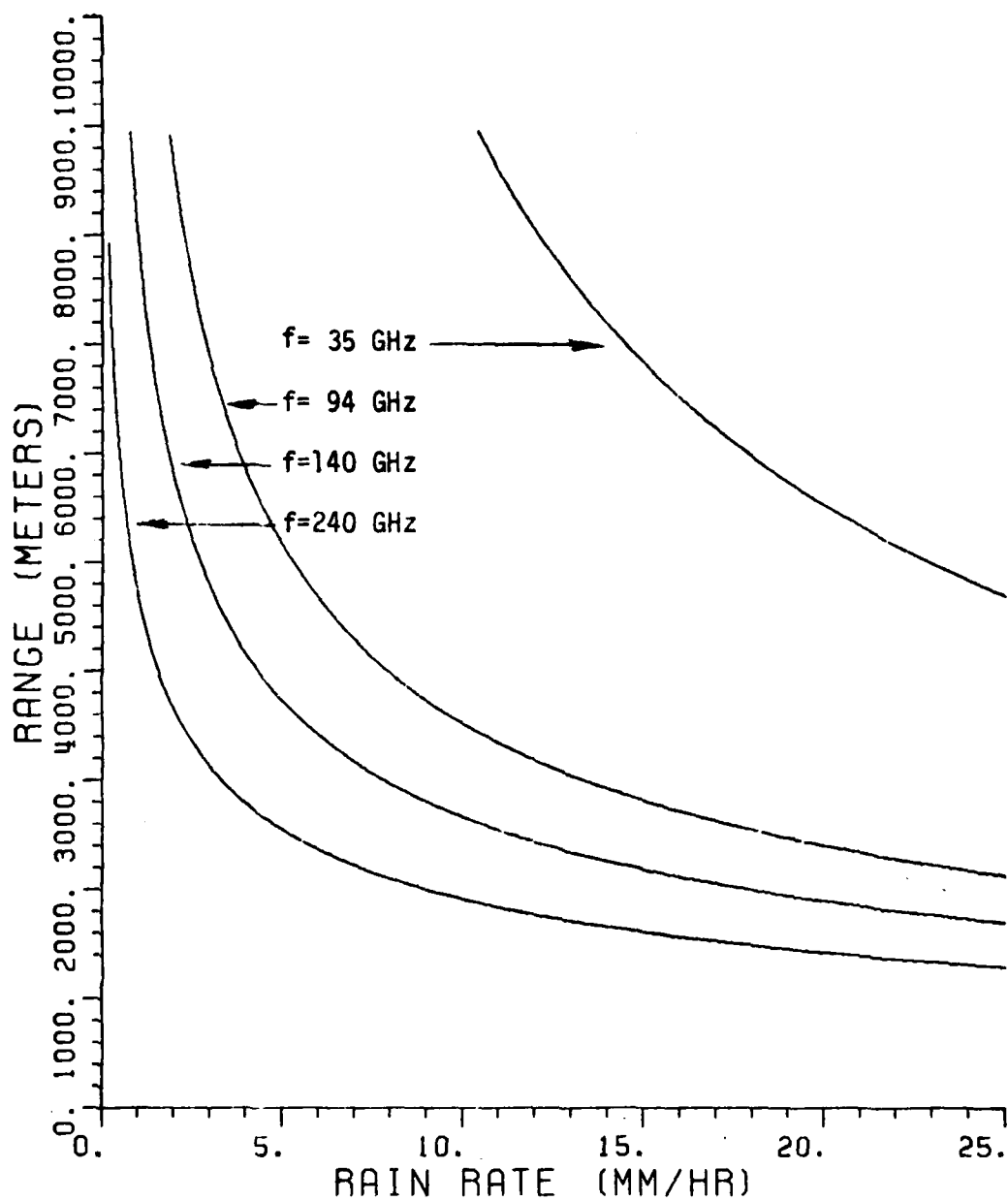


Figure 55. Range versus Rain Rate for the single-ended pulsed system with a quadrature receiver.  $P_d = 0.995$ ,  $P_{fa} = 10^{-6}$ ,  $\sigma = 10 \text{ m}^2$ , and  $T = 20^\circ \text{C}$ .

For unspecified system parameters, see Table I, p. 53.

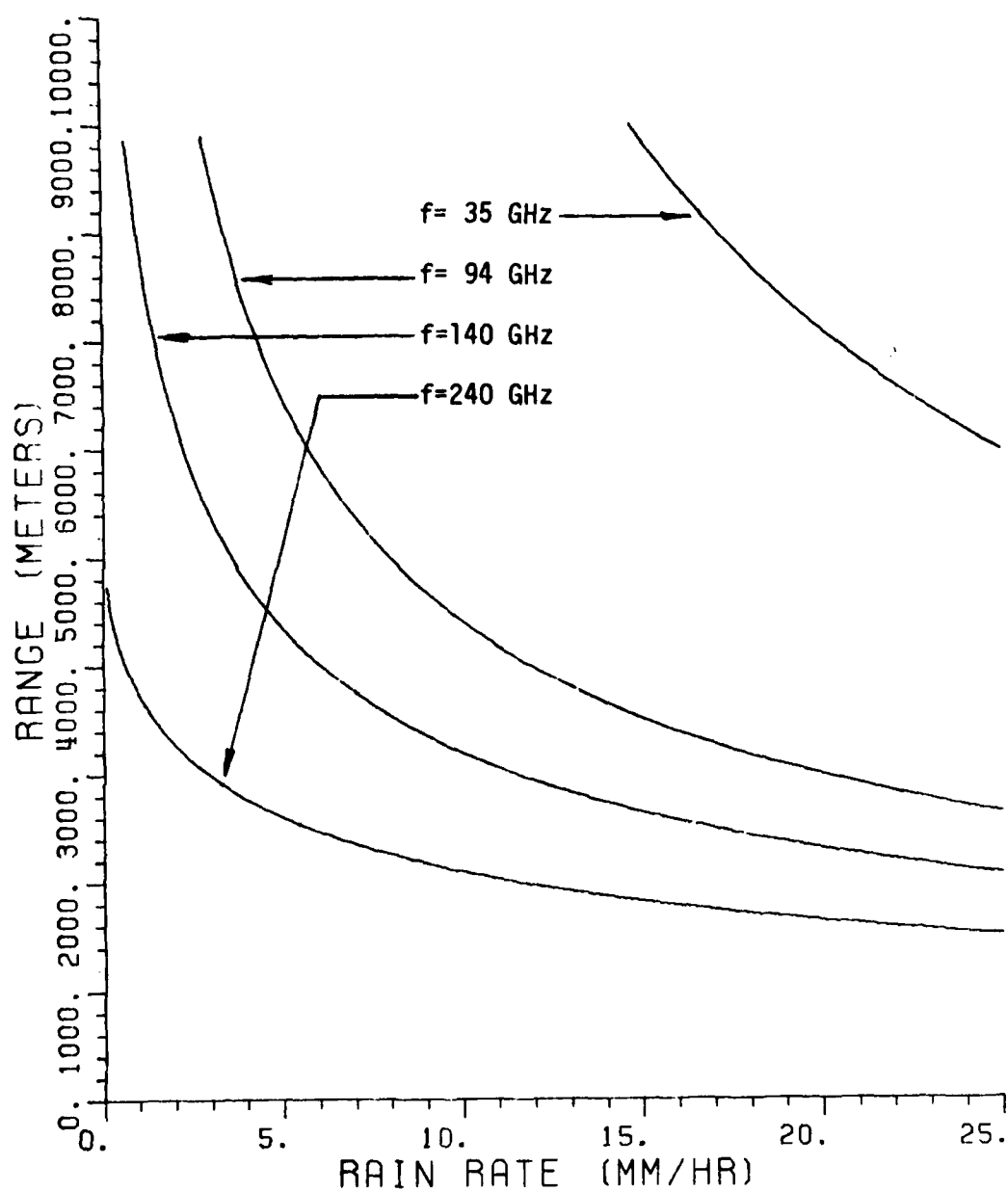


Figure 56. Range versus Rain Rate for the single-ended pulsed radar with pulse compression.  $P_d = 0.995$ ,  $P_{fa} = 10^{-6}$ ,  $\sigma = 10 \text{ m}^2$ , and  $T = 20^\circ \text{C}$ . For unspecified system parameters, see Table I, p. 53.

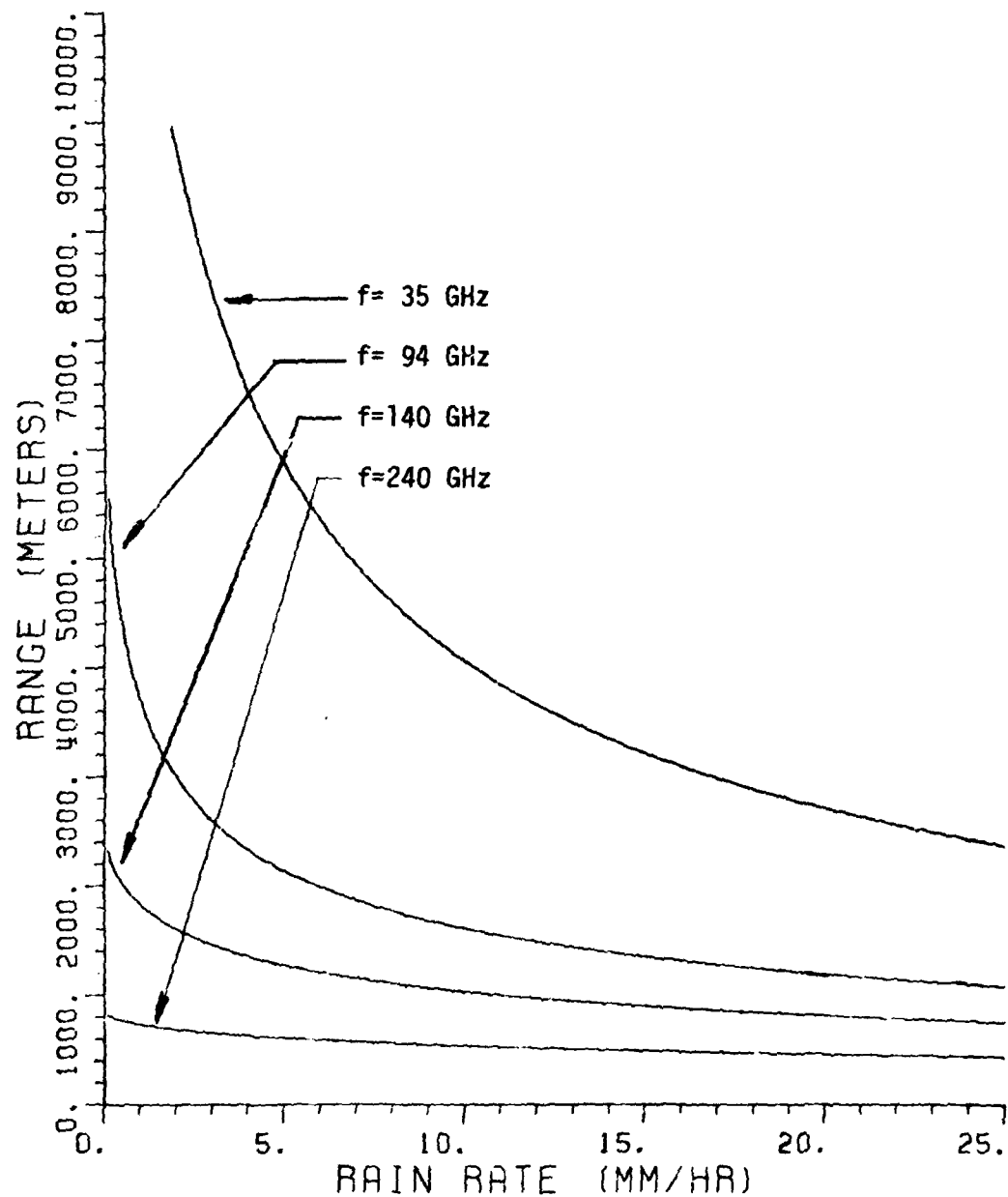


Figure 57. Range versus Rain Rate for the single-ended pulsed source range gated radar employing post-detection integration.  $P_d = 0.995$ ,  $P_{fa} = 10^{-6}$ ,  $\sigma = 125 \text{ m}^2$ , and  $T = 20^\circ \text{C}$ .

For unspecified system parameters, see Table I, p. 53.



Figure 52 shows range as a function of rain rate and frequency for the double-ended system with square-law detection of Section V.B.1. Figure 53 shows range versus rain rate for the single-ended system with square-law detection discussed in Section V.B.2. Figure 54 displays range versus rain rate for the single-ended CW system with quadrature receiver system of Section V.B.3. Figure 55 shows range as a function of rain rate for the single-ended pulsed system with quadrature receiver discussed in Section V.B.5. Figure 56 gives range as a function of rain rate for the single-ended pulsed radar with pulse compression discussed in Section V.B.6. Finally, Figure 57 shows range as a function of rain rate for the range gated radar of Section V.B.4. As expected, the double-ended systems are less sensitive to the effects of rain because the transmission path is only half as long as with the single-ended systems.

#### C. Effects of Fog Attenuation.

Not only can we construct a model to predict radar range as a function of rain rate, we can also predict radar range as a function of liquid water content in fog. As discussed in Section IV, a fog drop-size distribution given by Equation (108) and a routine to calculate complex index of refraction for liquid water is used.

Here, a computer subroutine was implemented to calculate specific attenuation of fog in terms of liquid water content. This attenuation calculation can be applied to any of the five single-ended systems discussed in before. However, here we choose to use the CW radar system of Section II.B.3 in order to compare with results presented in part B of this section.

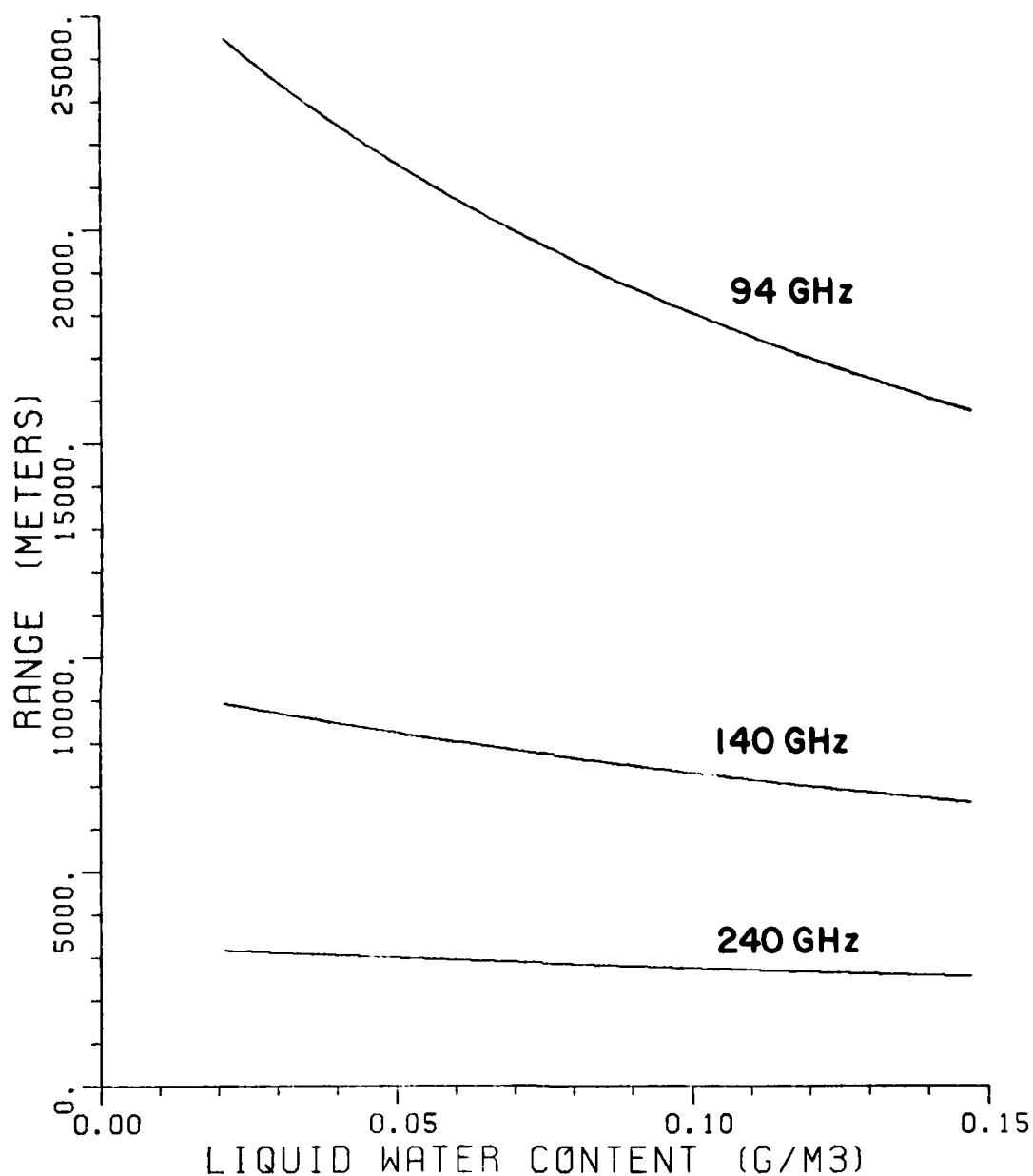


Figure 58. Range versus Liquid Water Content in fog for the single-ended CW system with a quadrature receiver.  $P_d = 0.995$ ,  $P_{fa} = 10^{-6}$ ,  $\sigma = 125 \text{ m}^2$ , and  $T = 20^\circ \text{C}$ .  
For unspecified system parameters, see Table I, p. 53.

The fog drop-size distribution is used as a subprogram. By changing this subroutine, we could calculate attenuation due to fog with other expressions or empirical data for drop-size distributions.

Figure 58 shows radar range for the CW system with quadrature receiver versus liquid water content of a fog. This graph shows frequency as the parameter because temperature of water in the propagation path does not significantly affect range. The temperature and frequency dependence of the complex index of refraction of liquid water is shown in Table II, as computed by the subroutine.

In general, notice that the radar range greatly decreases for increasing liquid water content and frequencies in fog in an analogous manner as range decreases for increasing rain rates.

#### D. Conclusions.

Six transmission systems were examined for frequencies of 35, 94, 140, and 240 GHz. The first system examined was for propagation over a one-way path. The remaining five instrumentation systems measure reflected signals from a calibrated target. Each of the single-ended systems employs a different method of signal detection.

It is found that the best range values under severe weather conditions can be acquired with the double-ended propagation system. This is true because the path over which the signal travels is only half the length of the five radar systems and under severe conditions path attenuation can be very large. As far as the single-ended systems are concerned, the system with a CW signal and quadrature detector (Section II.B.3) appears to give the best range performance under severe weather conditions at millimeter frequencies.

For an experimental transmissometer, the single-ended systems have an advantage in that the range performance can be varied easily by simply moving the calibrated target. Thus, it may be best to use a radar system with a quadrature receiver. This type of instrumentation is preferable because of the linear nature of the detector which works extremely well for low signal-to-noise ratios at the input to the detector.

Finally, an examination of the effects of rain and fog attenuation was presented in this chapter. The purpose was to show quantitatively how range decreases as a function of increasing rain rate and increasing liquid water contents of fog as a function of frequency and system configuration.

## REFERENCES

1. Rosenblum, E.S., "Atmospheric Absorption of 10 to 400 kMCPS Radiation," Microwave Journal, (March, 1961), pp. 91-96.
2. Buyukdura, O. and Levis, C., A Comparison of Several Systems for Transmission Measurements at 94 GHz, Report AFWAL-TR-81-1281, Avionics Laboratory, Air Force Wright Aeronautical Laboratories, Air Force Systems Command, Wright-Patterson Air Force Base, Ohio 45433, February 1982.
3. Schwartz, M., Information, Transmission, Modulation and Noise, McGraw-Hill, 1970.
4. Haykin, S., Communication Systems, John Wiley and Sons, 1978.
5. Schilling, D., and Taub, H., Principles of Communication Systems, McGraw-Hill, 1971, p. 307.
6. Marcum, J.I., "A Statistical Theory of Target Detection by Pulsed Radar, Mathematical Appendix," I.R.E. Transactions on Information Theory, Volume IT-6 (April, 1960), pp. 59-267.
7. Skolnik, M.I., Introduction to Radar Systems, McGraw-Hill, 1980. p. 31.
8. Skolnik, op. cit., p. 422.
9. Skolnik, op. cit., pp 23-29.
10. Mie, G. "Considerations of the Optics of Turbid Media, Especially Colloidal Metal Sols," Annalen der Physik, Vol. 25, 1908.
11. Kerker, M. Scattering of Light, Academic Press, 1969, pp. 27-96
12. Ray, P.S., "Broadband Complex Refractive Indices of Ice and Water," Applied Optics, Vol. 11, No. 8, August, 1972, pp. 1836-1844.
13. Falcone, V.J., Abreu, L.W., and Shettle, E.P., Atmospheric Attenuation of Millimeter and Submillimeter Waves: Models and Computer Code. Air Force Geophysics Laboratory, Hanscom Air Force Base, Mass., Report #AFGL-TR-79-0253, p.60.

14. Schuchardt, J.M., Newton, J.M., Morton, T.P., and Gagliano, J.A., "The Coming of mm-Wave Forward Looking Imaging Radiometers." *Micro-wave Journal*, Vol. 24, June, 1981, pp. 45-62.
15. Kunkel, B.A., "Fog Drop-Size Distributions Measured with a Laser Hologram Camera," *Journal of Applied Meteroloty*, Vol. 10, June, 1971, pp. 482-486.
16. Mallow, J.V., "Empirical Fog Droplet Size Distributions with Finite Limits." *Journal of the Atmospheric Sciences*, Vol. 32, February, 1975, pp. 440-443.
17. Tsang, L., Kong, J.A., Staelin, D.H., and Waters, J.W., "Theory for Microwave Thermal Emission from a Layer of Cloud or Rain." *I.E.E.E. Transactions on Antennas and Propagation*, Vol. AP-25, September, 1977, pp. 650-657.
18. Cook, C.E., "Pulse Compression- Key to More Efficient Radar Transmission," *Proceedings of the I.R.E.*, Vol. 48, No. 3, March, 1960, pp. 310-316.

## APPENDIX A

### MODEL FOR COMPLEX INDEX OF REFRACTION

To calculate the attenuation parameter  $\alpha$ , it is necessary to develop an accurate model for the complex index of refraction of liquid water as a function of frequency and temperature. An empirical model of the complex refractive index of ice and liquid water has been performed by Peter S. Ray [12] with corrections given by Falcone [13]. In general this model is applicable from  $-20^{\circ}\text{C}$  to  $0^{\circ}\text{C}$  for ice and from  $-20^{\circ}\text{C}$  to  $50^{\circ}\text{C}$  for liquid water. Also, the model is found to be applicable for wavelengths of  $2\mu\text{m}$  to several thousand kilometers in ice and from  $2\mu\text{m}$  to several hundred meters for liquid water. In the presentation below, a general discussion of Ray's model for both ice and water will be given. However, for our work only liquid water will be required.

For this model, consider data given in terms of the complex relative permittivity,  $\epsilon = \epsilon' - j\epsilon''$  where  $\epsilon'$  is the relative dielectric constant and  $\epsilon''$  represents the effects of loss. These are related to the complex index of refraction by

$$\epsilon' = n_r^2 - n_i^2 \quad (\text{A1})$$

$$\epsilon'' = 2n_r n_i \quad (\text{A2})$$

Solving these two simultaneous equations gives

$$n_r = \left[ \frac{\epsilon'}{2} + \frac{1}{2} [(\epsilon')^2 + (\epsilon'')^2]^{1/2} \right]^{1/2} \quad (\text{A3})$$

$$n_i = \frac{\epsilon''}{2n_r} \quad (\text{A4})$$

In these equations,  $n_r$  represents the real part and  $n_i$  represents the imaginary part of the complex index of refraction ( $n = n_r - jn_i$ ). For

water, the complex permittivity is a function of wavelength according to the Debye model

$$\epsilon' = \epsilon_i + \frac{(\epsilon_s - \epsilon_i)}{1 + [\lambda_s/\lambda]^2} \quad (A5)$$

$$\epsilon'' = \frac{(\epsilon_s - \epsilon_i)(\lambda_s/\lambda)}{1 + (\lambda_s/\lambda)^2} \quad (A6)$$

where  $\epsilon_i$  is the high frequency dielectric constant,  $\epsilon_s$  the static dielectric constant, and  $\lambda_s$  the relaxation wavelength. The temperature dependence of  $\epsilon_s$  is determined experimentally [12] as

$$\epsilon_s = 78.54 \left[ 1.0 - (4.579 \times 10^{-3})(T-25) + (1.19 \times 10^{-5})(T-25)^2 - (2.8 \times 10^{-8})(T-25)^3 \right] \quad (A7)$$

where T is given in degrees Celsius.

The equations used in the calculation for centimeter absorption are an extension of the Debye theory, modified by a frequency independent conductivity  $\sigma = 12.5664 \times 10^8$  mhos/cm. These equations are given as

$$\epsilon' = \epsilon_i + \frac{(\epsilon_s - \epsilon_i) \left[ 1 + (\lambda_s/\lambda) \frac{1 - \alpha_0}{1 + 2(\lambda_s/\lambda)^{1 - \alpha_0} \sin(\alpha_0 \pi/2) + (\lambda_s/\lambda)^2 (1 - \alpha_0)} \sin(\alpha_0 \pi/2) \right]}{1 + 2(\lambda_s/\lambda)^{1 - \alpha_0} \sin(\alpha_0 \pi/2) + (\lambda_s/\lambda)^2 (1 - \alpha_0)} \quad (A8)$$

and

$$\epsilon'' = \frac{(\epsilon_s - \epsilon_i)(\lambda_s/\lambda) \cos(\alpha_0 \pi/2)}{1 + 2(\lambda_s/\lambda)^{1 - \alpha_0} \sin(\alpha_0 \pi/2) + (\lambda_s/\lambda)^2 (1 - \alpha_0)} + \frac{\sigma \lambda}{18.8496 \times 10^{10}} \quad (A9)$$

where  $\alpha_0$  is a spread parameter in the experimental measurement. The parameters  $\epsilon_i$ ,  $\alpha_0$ , and  $\lambda_s$  are solely a function of temperature and are given by

$$\epsilon_i = 5.27137 + 0.0216474T - 0.00131198T^2 \quad (A10)$$

$$\alpha_0 = \frac{-16.8129}{T+273} + 0.0609265 \quad (A11)$$

and

$$\lambda_s = (3.3836 \times 10^{-4}) e^{\left[ \frac{2513.98}{T+273} \right]} \quad (A12)$$

where all wavelengths are in centimeters.



The complex index of refraction is given by Equations (A3) and (A4) when Equations (A10), (A11), and (A12) are substituted into (A8) and (A9). In general, the complex refractive index will then be of the form

$$n = n_r - jn_i \quad (A13)$$

For ice, Equations (A8) and (A9) are still applicable, however, the defining equations for  $\epsilon_i$ ,  $\alpha_0$ ,  $\lambda_s$  and  $\sigma$  are different. Once again, results are found experimentally as

$$\epsilon_i = 3.168 \quad (A14)$$

$$\alpha_0 = 0.288 + 0.0052T + (2.3 \times 10^{-4})T^2 \quad (A15)$$

$$\sigma = 1.26e^{\left[ \frac{-1.25 \times 10^4}{1.9869(T+273)} \right]} \quad (A16)$$

$$\lambda_s = 9.990288 \times 10^{-5} e^{\left[ \frac{1.32 \times 10^4}{1.9869(T+273)} \right]} \quad (A17)$$

and

$$\epsilon_s = 203.168 + 2.5T + 0.15T^2 \quad (A18)$$

Substitution of these last five expressions into Equations (A8) and (A9), then into (A3) and (A4) gives an expression for the complex refractive index of ice.

The FORTRAN computer program REFRAC shown in Volume II permits a calculation of the complex index of refraction as a function of a given temperature and variable wavelength. Figures A1 through A4 show typical results of the complex refractive index of liquid and ice water for various temperatures. The scales for the refractive index were chosen to make it easy to compare plots for water and ice directly with plots given by Ray's article [12].

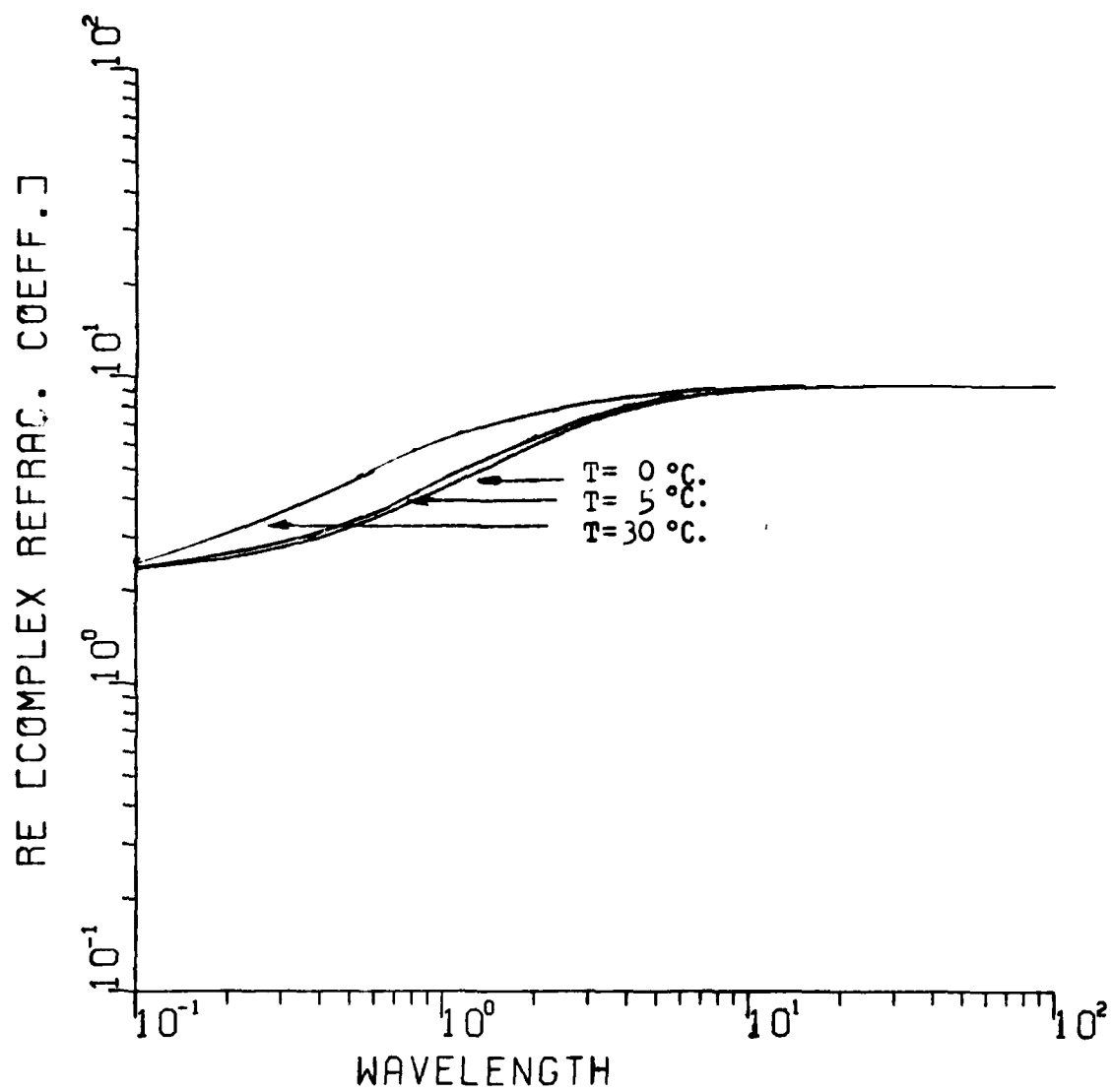


Figure A1. Real part of Refractive Index of liquid water (wavelength in centimeters.)

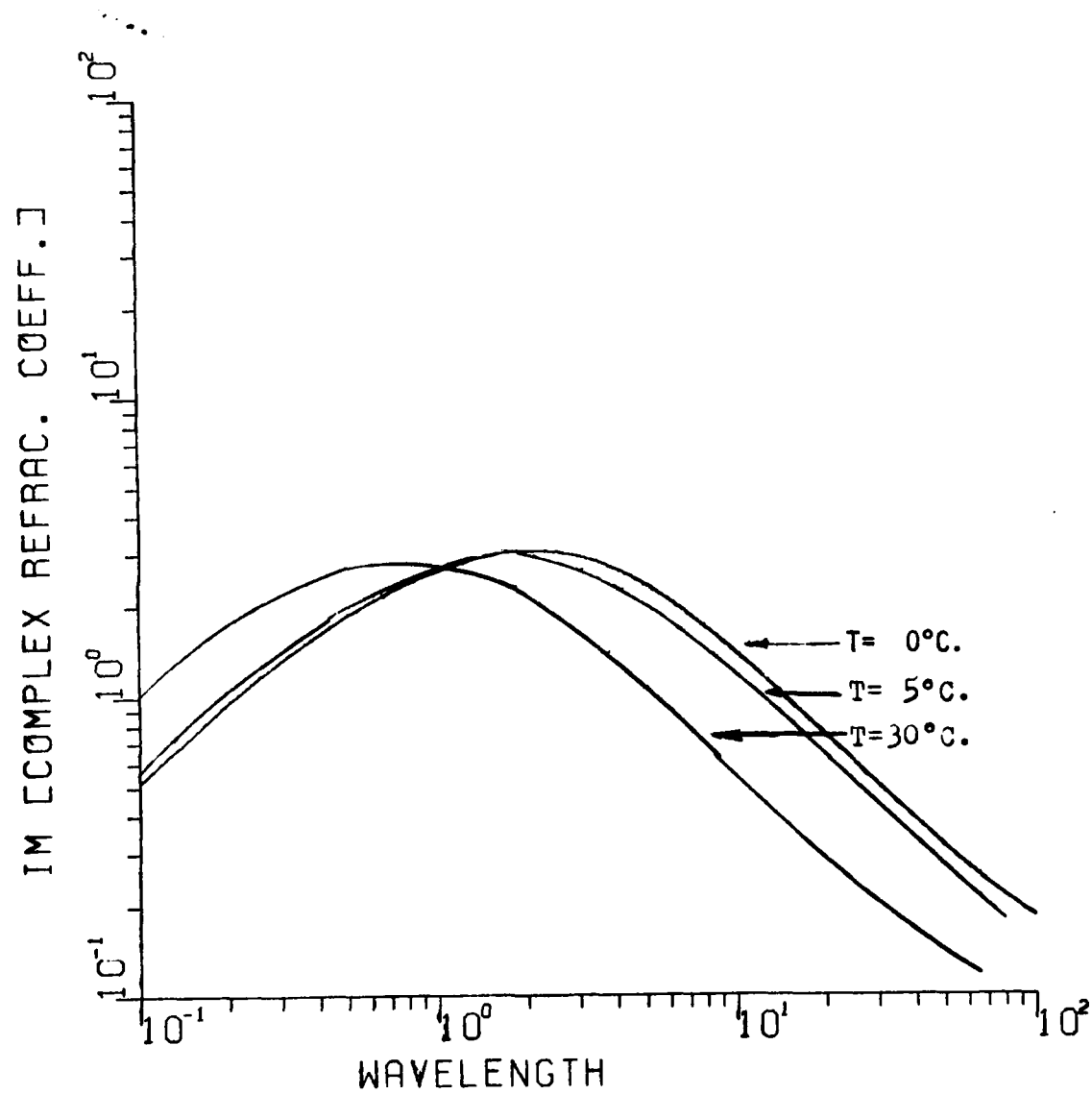


Figure A2. Imaginary part of Refractive Index of liquid water (wavelength in centimeters.)

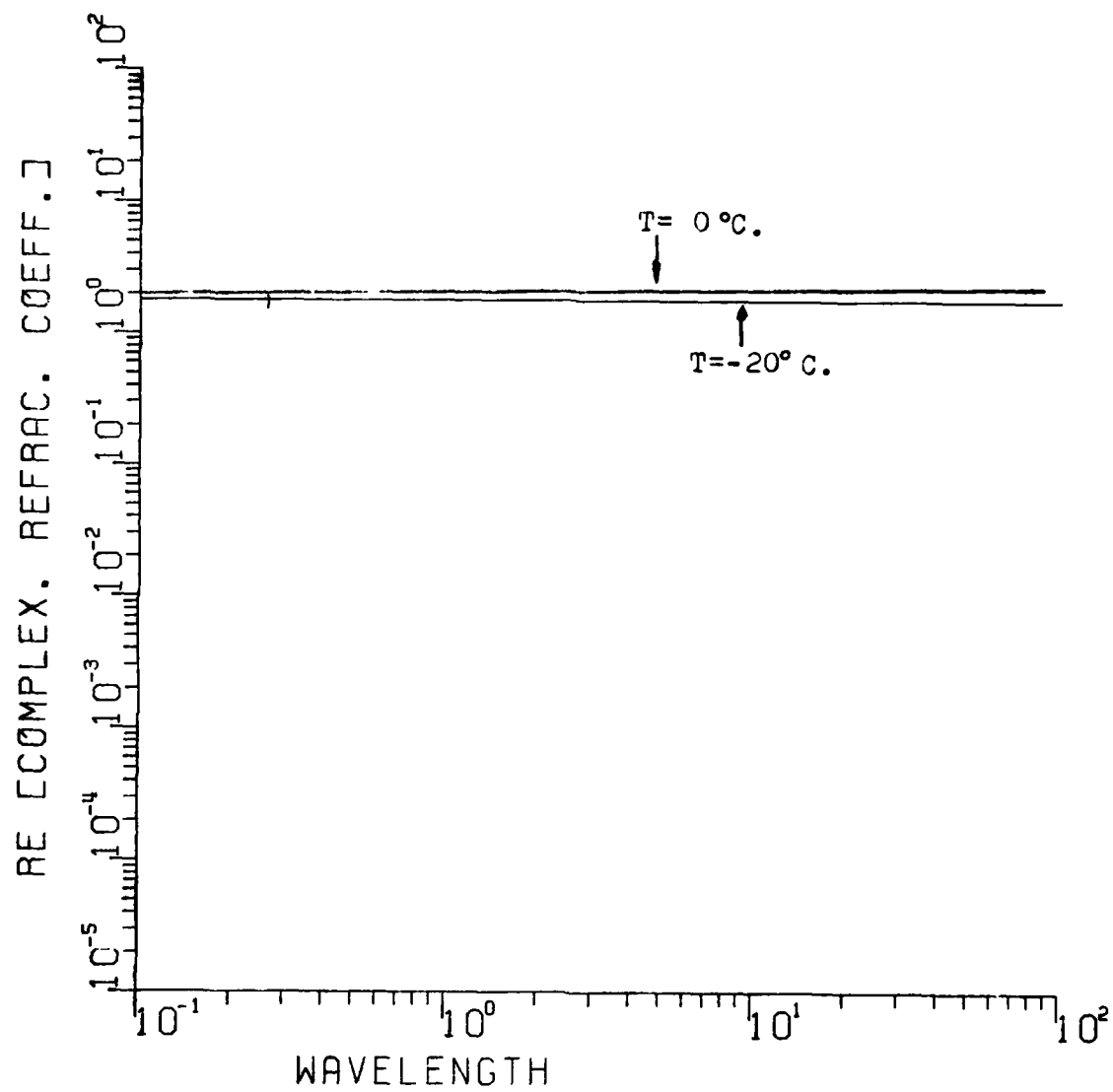


Figure A3. Real part of Refractive Index of frozen water (wavelength in centimeters.)

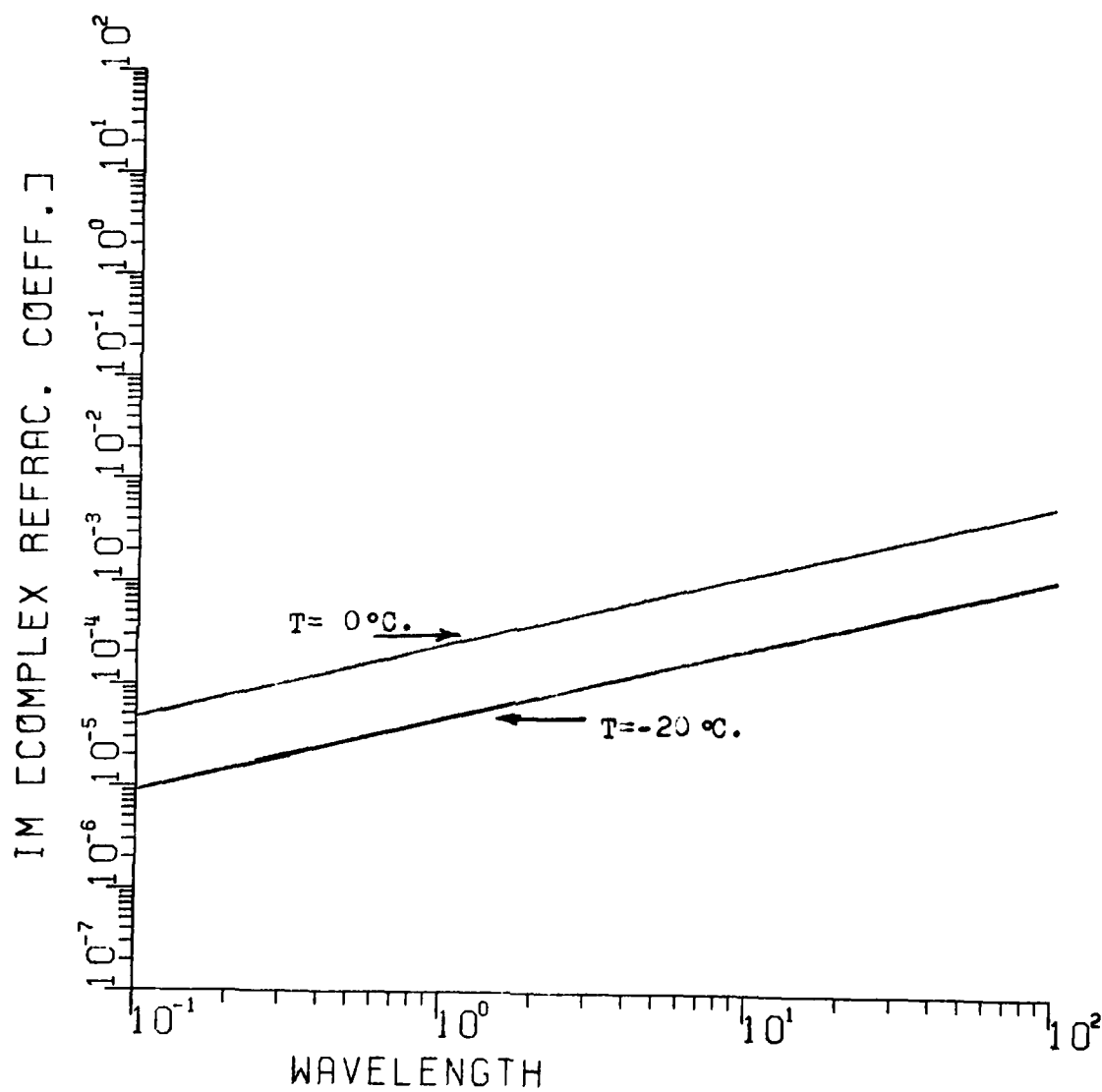


Figure A4. Imaginary part of Refractive Index of frozen water (wavelength in centimeters.)

# APPENDIX B PULSE COMPRESSION RADAR

For the transmission system under study, the transmitted signal is of the form

$$f(t) = A \cos[\phi(t)] \quad -\frac{T}{2} < t < \frac{T}{2} \quad (B1)$$

where  $\phi(t)$  is the phase angle of the transmitted frequency defined by Cook [18] as

$$\phi(t) = \omega_c t + \frac{\mu t^2}{2} \quad (B2)$$

and  $\mu$  is a constant given by  $\mu = \Delta\omega/T = 2\pi\Delta f/T$ . Therefore, the instantaneous frequency is a linear function

$$\omega = \frac{d\phi(t)}{dt} = \omega_c + \mu t \quad (B3)$$

We wish to determine a relation between input power and output power of the pulse compression filter so that the signal-to-noise ratio before detection can be defined. Using the method outlined by Cook, let's consider a unity magnitude linear FM rectangular-envelope pulse compression (i.e.,  $A=1$ ) and assume the generalized compression filter transfer function is

$$H(\omega, \mu) = e^{-\frac{j(\omega_c - \omega)^2}{2\mu}} \quad (B4)$$

Therefore, the pulse spectrum is given by the Fourier transform of  $f(t)$ . That is,

$$F(\omega) = \int_{-\infty}^{\infty} f(t) e^{-j\omega t} dt \quad (B5)$$

so

$$F(\omega) = \int_{-T/2}^{T/2} \cos\left[\omega_c t + \frac{\mu t^2}{2}\right] e^{-j\omega t} dt$$

or

$$F(\omega) = \frac{1}{2} \left[ \int_{-T/2}^{T/2} e^{j\left[(\omega_c - \omega)t + \frac{\mu t^2}{2}\right]} dt + \int_{-T/2}^{T/2} e^{-j\left[(\omega_c + \omega)t + \frac{\mu t^2}{2}\right]} dt \right] \quad (B5)$$

Then, if we define

$$F_+(\omega, \omega_c, \mu) = \int_{-T/2}^{T/2} e^{j\left[\omega_c t + \frac{\mu t^2}{2}\right]} e^{-j\omega t} dt \quad (B6)$$

and

$$F_-(\omega, \omega_c, \mu) = \int_{-T/2}^{T/2} e^{-j\left[\omega_c t + \frac{\mu t^2}{2}\right]} e^{-j\omega t} dt \quad (B7)$$

it follows that

$$F(\omega) = \frac{1}{2} [F_+(\omega, \omega_c, \mu) + F_-(\omega, \omega_c, \mu)] \quad (B8)$$

However, notice that

$$F_-(\omega, \omega_c, \mu) = F_+(\omega, -\omega_c, -\mu) \quad (B9)$$

so

$$F(\omega) = \frac{1}{2} [F_+(\omega, \omega_c, \mu) + F_+(\omega, -\omega_c, -\mu)] \quad (B10)$$

and

$$G(\omega) = F(\omega)H(\omega, \mu) = \frac{1}{2} [H(\omega, \mu)F_+(\omega, \omega_c, \mu) + H(\omega, \mu)F_+(\omega, -\omega_c, -\mu)]. \quad (B11)$$

Therefore, the real time-varying output function becomes

$$g_1(t) = \frac{1}{2} \mathfrak{F}^{-1}[H(\omega, \mu)F_+(\omega, \omega_c, \mu)] + \frac{1}{2} \mathfrak{F}^{-1}[H(\omega, \mu)F_+(\omega, -\omega_c, -\mu)]$$

or

$$g(t) = \frac{1}{2}g_1(t) + \frac{1}{2}g_2(t) . \quad (B12)$$

We can examine both  $g_1(t)$  and  $g_2(t)$  separately in order to derive the output function. By definition of the inverse Fourier integral

$$\begin{aligned} g_1(t) &= \mathcal{F}^{-1}[H(\omega, \mu)F_+(\omega, \omega_c, \mu)] \\ &= \frac{1}{2\pi} \int_{-\infty}^{\infty} H(\omega, \mu)F_+(\omega, \omega_c, \mu)e^{j\omega t} d\omega \end{aligned}$$

or

$$g_1(t) = \frac{1}{2\pi} \int_{-\infty}^{\infty} \left[ e^{\frac{j(\omega_c - \omega)^2}{2\mu}} \int_{-T/2}^{T/2} e^{j[(\omega_c - \omega)t_1 + \frac{\mu t_1^2}{2}]} dt_1 \right] e^{j\omega t} d\omega$$

which can be rearranged as

$$\begin{aligned} g_1(t) = \frac{1}{2\pi} \int_{-T/2}^{T/2} \left[ e^{j\left[\frac{\mu t_1^2}{2} + \omega_c t_1 + \frac{\omega_c^2}{2\mu} - \frac{(\omega_c + \mu t_1 - \mu t)^2}{2\mu}\right]} \right. \\ \left. \times \int_{-\infty}^{\infty} e^{\frac{j\mu}{2}[\omega - (\omega_c + \mu t_1 - \mu t)]^2} d\omega \right] dt_1 \end{aligned} \quad (B13)$$

Now, using the substitution

$$u = \frac{\omega - (\omega_c + \mu t_1 - \mu t)}{\sqrt{2\mu}} \quad (B14)$$

we see

$$g_1(t) = \frac{\sqrt{2\mu}}{2\pi} \int_{-T/2}^{T/2} \left[ e^{j\left[\frac{\mu t_1^2}{2} + \omega_c t_1 + \frac{\omega_c^2}{2\mu} - \frac{(\omega_c + \mu t_1 - \mu t)^2}{2\mu}\right]} \int_{-\infty}^{\infty} e^{ju^2} du \right] dt_1. \quad (B15)$$

But, we can show

$$\int_{-\infty}^{\infty} e^{ju^2} du = \int_{-\infty}^{\infty} [\cos u^2 + j\sin u^2] du = \sqrt{\pi} e^{j\frac{\pi}{4}}$$



so that

$$g_1(t) = \frac{\sqrt{2\mu}}{2\pi} \int_{-T/2}^{T/2} e^{j\left[\frac{\mu t_1^2}{2} + \omega_c t_1 + \frac{\omega_c^2}{2\mu} - \frac{(\omega_c + \mu t_1 - \mu t)^2}{2\mu}\right]} \sqrt{\pi} e^{j\frac{\pi}{4}} dt_1$$

or

$$g_1(t) = \frac{\sqrt{\mu}}{\sqrt{2\pi}} e^{j\left[\frac{\omega_c t}{2} - \frac{\mu t^2}{2} + \frac{\pi}{4}\right]} \int_{-T/2}^{T/2} e^{j\mu t t_1} dt_1$$

which reduces to

$$g_1(t) = \sqrt{\frac{2\mu[T/2]^2}{\pi}} \frac{\sin \mu t (T/2)}{\mu t (T/2)} e^{j\left[\frac{\omega_c t}{2} - \frac{\mu t^2}{2} + \frac{\pi}{4}\right]}. \quad (B16)$$

Now, let's perform a similar integration to find  $g_2(t)$ . Knowing

$$\begin{aligned} g_2(t) &= \mathcal{F}^{-1}[H(\omega, \mu) F_+(\omega, -\omega_c, -\mu)] \\ &= \frac{1}{2\pi} \int_{-\infty}^{\infty} H(\omega, \mu) F_+(\omega, -\omega_c, -\mu) e^{j\omega t} d\omega \end{aligned}$$

so

$$g_2(t) = \frac{1}{2\pi} \int_{-\infty}^{\infty} \left[ e^{j\frac{(\omega_c - \omega)^2}{2\mu}} \int_{-T/2}^{T/2} e^{-j\left[\frac{(\omega_c + \omega)t_1 + \mu t_1^2}{2}\right]} dt_1 \right] e^{j\omega t} d\omega$$

which can be rearranged to

$$\begin{aligned} g_2(t) &= \frac{1}{2\pi} \int_{-T/2}^{T/2} \left[ e^{-j\left[\frac{\mu t_1^2}{2} + \omega_c t_1 + \frac{\omega_c^2}{2\mu} - \frac{(\omega_c + \mu t_1 - \mu t)^2}{2\mu}\right]} \right. \\ &\quad \left. \times \int_{-\infty}^{\infty} e^{-j\frac{\mu}{2}[\omega - (\omega_c + \mu t_1 - \mu t)]^2} d\omega \right] dt_1 \end{aligned} \quad (B17)$$

Now, using the substitution given in Equation (B14), we see

$$g_2(t) = \frac{\sqrt{2\mu}}{2\pi} \int_{-T/2}^{T/2} \left[ e^{-j\left[\frac{\mu t_1^2}{2} + \omega_c t_1 + \frac{\omega_c^2}{2\mu} - \frac{(\omega_c + \mu t_1 - \mu t)^2}{2\mu}\right]} \int_{-\infty}^{\infty} e^{-ju^2} du \right] dt_1. \quad (B18)$$

But we can show

$$\int_{-\infty}^{\infty} e^{-ju^2} du = \int_{-\infty}^{\infty} [\cos u^2 - j \sin u^2] du = \sqrt{\pi} e^{-j\frac{\pi}{4}} \quad (B19)$$

so that

$$g_2(t) = \sqrt{\frac{2\mu}{2\pi}} \int_{-T/2}^{T/2} e^{-j\left[\frac{\mu t_1^2}{2} + \omega_c t_1 + \frac{\omega_c^2}{2\mu} - \frac{(\omega_c + \mu t_1 - \mu t)^2}{2\mu}\right]} \sqrt{\pi} e^{-j\frac{\pi}{4}} dt_1$$

or

$$g_2(t) = \sqrt{\frac{\mu}{2\pi}} e^{-j\left[\omega_c t - \frac{\mu t^2}{2} + \frac{\pi}{4}\right]} \int_{-T/2}^{T/2} e^{j\mu t t_1} dt_1$$

which reduces to

$$g_2(t) = \sqrt{\frac{2\mu[T/2]^2}{\pi}} \frac{\sin \mu t (T/2)}{\mu t (T/2)} e^{-j\left[\omega_c t - \frac{\mu t^2}{2} + \frac{\pi}{4}\right]} \quad (B20)$$

Upon substitution of Equations (B16) and (B20) into (B12) gives

$$g(t) = \sqrt{\frac{2\mu[T/2]^2}{\pi}} \frac{\sin \mu t (T/2)}{\mu t (T/2)} \cos\left[\omega_c t - \frac{\mu t^2}{2} + \frac{\pi}{4}\right] \quad (B21)$$

for the time-varying output function where  $\mu = 2\pi\Delta f/T$  is the swept-frequency deviation. Figure 8 of this thesis shows the relationship between the input and output waveforms of the pulse compression filter.

Since we previously assumed the input amplitude was unity, the output-input peak power ratio is found by squaring the amplitude of the output pulse. This implies

$$\frac{P_o}{P_i} = \frac{2\mu[T/2]^2}{\pi} = \frac{2(2\pi\Delta f/T)[T/2]^2}{\pi} = T\Delta f. \quad (B22)$$

The time function of the compressed pulse given by Equation (B21) is recognized as having the familiar sincx envelope. The pulse width is  $\tau = 1/\Delta f$  when measured 4 dB down from the peak amplitude. The spacing between the first zeros of this envelope is  $2/\Delta f$ . The instantaneous received frequency is a swept linearly (as was the transmitted frequency), and the relative peak amplitude is  $\sqrt{T\Delta f}$  as shown in Figure 8. Use of these results gives an expression for the output-input peak power ratio in terms of the pulse compression ratio K,

$$\frac{P_0}{P_i} = K = \frac{T}{\tau} . \quad (B23)$$

Notice that the shape of the compressed pulse is of the form sincx and not rectangular. Because of the high sidelobe levels, this may not be the most desirable pulse waveform for some radar applications, however, it should be sufficient for our application of estimating the effects of rain and fog.

The radar equation including losses before any signal processing at the receiver is given by Equation (13) for a single-ended transmission system. Therefore, using Equation (B23) gives an expression for signal power as

$$P_0 = \frac{P_t K G_t G_r L_t L_r \sigma \lambda^2}{(4\pi)^3 R^4} 10^{\frac{-2\alpha R}{10}} . \quad (B24)$$

The pre-detection signal-to-noise ratio for the radar transmitter is

$$\frac{S}{N} = \frac{P_t K G_t G_r L_t L_r \sigma \lambda^2}{(4\pi)^3 R^4 k T_0 B F} 10^{\frac{-2\alpha R}{10}} . \quad (B25)$$

If we consider a pulse compression radar with a quadrature receiver system as in Section II. B.5, then the output signal-to-noise ratio can be found from Equation (58) to be

$$\frac{E}{N} = \frac{P_t K G_t G_r L_t L_r \sigma \lambda^2 T_d B_{if}}{(4\pi)^3 R^4 k T_0 B F} 10^{\frac{-2\alpha R}{10}} . \quad (B26)$$

This result is presented in Section II. B.6 for the pulsed source with linear FM rectangular-envelope pulse compression.

Distribution List  
AFWAL TR-82-1147

<u>Organization</u>	<u>No. of Copies</u>
AFWAL/AART-3 Attn: R. Rang Wright-Patterson AFB, OH 45433	5
DTIC Cameron Station Alexandria, VA 22314	2
HQ USAF/SAMID Washington, DC 20330	1
HQ AFSC/IN Andrews AFB, MD 20334	1
AUL/LSI Maxwell AFB, AL 36112	1
AFWAL/TST-2 Wright-Patterson AFB, OH 45433	1
AFEWC/ESRI San Antonio, TX 78243	1
USA Night Vision and Electro-Optical Laboratories Attn: DELNV-AC (R. Wright) Ft Belvoir, VA 22060	1
Commander USA - Atmospheric Science Lab Attn: DELAS-EO-EN (D. Snyder)	1
US Army Missile Command Attn: DRMSI-REL (Mr T. Barley) Redstone Arsenal, AL 35898	1
Naval Weapons Center Attn: Mr D. Dobberpuhl (Code 31506) China Lake, CA 93555	1
AFGL/LYR Attn: Maj Mike Snapp Hanscom AFB, MA 01731	1
AFGL/OPI Hanscom AFB, MA 01731	1
AFWAL/WE Wright-Patterson AFB, OH 45433	1

OrganizationNo. of Copies

AFWAL/WEA Wright-Patterson AFB, OH 45433	1
EOARD Attn: Lt Col Peter Soliz Box 14 FPO New York, NY 09510	1
AFGL/LYS Attn: Vince Falcone Hanscom AFB, MA 01731	1
AFGL/OPI Attn: Lt Col Kit Cottrell Hanscom AFB, MA 01731	1
AFGL/LYS Attn: Dr Mike Kraus Hanscom AFB, MA 01731	1
USAF ETAC/ONE Attn: Capt Michael Abel Scott AFB, IL 62225	1
HQ AWS/DOOE Attn: Lt Col Bob Wright Scott AFB, IL 62225	1
AFWAL/AAAS-2 Attn: Dianne Sommers Wright-Patterson AFB, OH 45433	1
AFWAL/AARI-3 Attn: Leo Vroombout Wright-Patterson AFB, OH 45433	1
AFWAL/AARI-3 Attn: Roger Cranos Wright-Patterson AFB, OH 45433	1
AFWAL/AARM-4 Attn: Walt Barnes Wright-Patterson AFB, OH 45433	1
AFWAL/AARM-4 Attn: Ralph Becker Wright-Patterson AFB, OH 45433	1
AFWAL/AART-2 Wright-Patterson AFB, OH 45433	1

OrganizationNo. of Copies

AFWAL/AART-3 Attn: Lt Mark Schulte Wright-Patterson AFB, OH 45433	1
AFWAL/AADM-2 Wright-Patterson AFB, OH 45433	1
AFWAL/AARF-4 Attn: L. Crouch Wright-Patterson AFB, OH 45433	1
ASD/ENAMD Wright-Patterson AFB, OH 45433	1
ASD/RWNM Attn: Mr Benitez Wright-Patterson AFB, OH 45433	1
AFWAL Liaison Office AD/XRG (AFWAL) Eglin AFB, FL 32542	2
Quest Research Corporation 4999 Northcut Place Suite 2 Dayton, OH 45414	1
Science Applications, Inc. Attn: Mr Wasky 1010 Woodman Drive Suite 200 Dayton, OH 45432	1
Harry Diamond Laboratories Attn: Dr J. Nemerich 2800 Powder Mill Road Adelphi, MD 20783	1
Ohio State University Electro-Science Laboratory Attn: Dr C. Levis 1320 Kinnear Road Columbus, OH 43212	5
Alpha Industries, Inc. Attn: R. Gerrich 20 Sylvan Road Woburn, MA 01801	1

<u>Organization</u>	<u>No. of Copies</u>
U.S. Naval Weapons Center, Code 3313 Attn: Gaylon E. Ryno China Lake, CA 93555	1
The Aerospace Corporation Attn: Howard E. King Bldg. 120, Room 2011 2350 East El Segundo Blvd. El Segundo, CA 90245	1
Dept. of the Army Harry Diamond Laboratories 2800 Powder Mill Rd. Adelphi, MD 20738 Attn: A. Sindoris	1
USA CORADCOM CENCOMS DRDCO-COM-RH-1 Ft. Monmouth, N.J. 07703 Attn: Dr. Felix Schwerling	1
Office of Naval Research, Code 427 800 North Quincy St. Arlington, VA 22217 Attn: Dr. R. Collins	1
U.S. Army Research Office P.O. Box 12211 Research Triangle Park North Carolina 27709 Attn: Dr. W.A. Flood	1
U.S. Navy Naval Ocean Systems Center Attn: Dr. John Hoffman, Code 8255 San Diego, CA 92152	1
Jet Propulsion Laboratory Attn: Dr. E.K. Smith, MS 161-228 4800 Oak Grove Drive Pasadena, CA 91109	1
Lincoln Laboratory, MIT Attn: Dr. Alan Simmons Lexington, MA 02173	1

Organization

No. of Copies

Georgia Institute of Technology  
Engineering Experiment Station  
Attn: David Schmieder  
Atlanta, GA 30332

1

Georgia Institute of Technology  
Engineering Experiment Station  
Attn: Dr Jim Echard  
Atlanta, GA 30332

1

Georgia Institute of Technology  
Engineering Experiment Station  
Attn: Dr Robert McMillan  
Atlanta, GA 30332

1

NASA Goddard Space Flight Center  
Attn: Dr David Atlas, Code 910  
Greenbelt, MD 20771

1

RADC/EEP  
Attn: Dr Paul Lossey  
Hanscom AFB, MA 01731

1

NASA Headquarters, EC-4  
Attn: Dr Louis J. Ippolito  
Washington, D.C. 20546

1



**END**

**FILMED**

**11-83**

**DTIC**